UNIVERSITÀ DEGLI STUDI DI GENOVA
SCUOLA DI SCIENZE MATEMATICHE FISICHE E NATURALI
CORSO DI DOTTORATO IN FISICA

LINEAR AND NON-LINEAR PHOTOACTIVATION
A TOOL FOR NEUROSCIENCE AND CANCER RESEARCH.

Supervisors:
Prof. Alberto Diaspro
Prof. Mauro Robello
Dr. Paolo Bianchini

Candidate:
MARCO COZZOLINO

XXXII Cycle Ph.D.

Look up the stars and not down at your feet. Try to make sense of what you see and wonder about what makes the universe exist. Be curious.

(Stephen Hawking)

Contents

List of acronyms

1PE one-photon excitation

2PE Two-photon excitation

ApoMb Apomyoglobin

BSA Bovine serum albumin

CNS central nervous system

DMSO dimethyl sulfoxide

EPR Enhanced Penetration and Retention

FITC Fluorescein-5-Isothiocyanate

FWHM full width at half maximum

GABA γ-aminobutyric acid

HeLa Henrietta Lacks (uterine cell variety)

HOMO the Highest Occupied Molecular Orbitals

Hyp Hypericin

ISC inter-system crossing

LCAO linear combination of atomic orbitals

LUMO and the Lowest Unoccupied Molecular Orbitals

MPE Multiphoton excitation

NA numerical aperture

PALM photoactivation localization microscopy

PDT Photodynamic therapy

PS photosensitizer

PSF point spread function

ROS reactive oxygen species

SIM structured illumination microscopy

STORM stochastic optical reconstruction microscopy

STED stimulated emission depletion microscopy

VIP Vasoactive Intestinal Peptide

ZnMb Zinc-Substituted Myoglobin

ZnPc Zinc-phthalocyanine

List of figure

Fig. 4.2: Examples of chloride current peaks evoked by 10 µM uncaged RuBi – GABA at different laser powers during 1PE (458 nm, 100 ms) (A) and 2PE (750 nm, 100 ms) (B) on the same cell;
Fig. 4.3: Normalized values of current evoked by 10 µM (black squares) and 20 µM (red dots) uncaged RuBi – GABA at different laser powers during 1PE (458 nm, 100 ms) (A) and 2PE (750 nm, 100 ms) (B).

Fig. 4.4: Examples of chloride current peaks evoked by 10 µM uncaged RuBi – GABA at different exposure times during 1PE (458 nm, 9.36 µW) (A) and 2PE (750 nm, 125 mW) (B) on the same cell.

Fig. 4.5: normalized values of current evoked by 10 µM uncaged RuBi – GABA at different exposure times during 1PE (458 nm, 9.36 µW) (A) and 2PE (750 nm, 125 mW) (B).

Fig. 4.6: time of decay in function of the exposure time (τ) *during 1PE (458 nm, 9.36 µW) (A) and 2PE (750 nm, 125 mW) (B);*

Fig. 4.7: the difference between FWHM and FWHM at 1 ms in the function of the exposure time during 1PE (458 nm, 9.36 µW) (A) and 2PE (750 nm, 125 mW) (B).

Fig. 4.8: Example of uncaging point variations on X–Y axis

Fig. 4.9: Currents related to the example of fig. 4.8 during 2PE (750 nm, 100 ms, 77.3 mW) (A) and 1PE (458 nm, 100 ms, 9.36 µW) (B).

Fig. 4.10: Peak value for 1PE (458 nm, 100 ms, 9.36 µW) and 2PE (750 nm, 100 ms, 77.3 mW)to vary of XY distance;

Fig. 4.11: Normalized data (at least three cells) current value at different Z-Distance:

*Fig. 4.12***:** *Current – potentials curve obtained after the administration of 10 µM GABA.*

*Fig. 4.13***:** *Current – potentials curve obtained after uncaging of 10 µM RuBi – GABA with 1PE (458 nm, 9 µW) and 100 ms of exposure time.*

Fig. 4.14 Photoinduced damage to HeLa and PC3 cells incubated with Hyp-apoMb.

Fig. 4.15. Uptake dynamics of Hyp and Hyp-apoMb.

Introduction

Photoactivation is a physical process that allows using light-matter interaction as a precursor to induce a specific Physico-chemical reaction.

This reaction is induced after the absorption of a photon, having a suitable wavelength, by specific photoactivable molecules. Such molecules act as a molecular machine that performs functions useful both for therapeutic purposes but also for the study of biophysical processes. The ability to have high temporal and spatial control is one of the main advantages of photoactivation. Therefore combining the photoactivation with appropriate optical methods, manipulation of living specimens at molecular precision is possible.

Moreover, a set of photoactivable molecules is the key player in realizing super-resolution microscopy, allowing the quantitative study of biological challenges at the subcellular scale. [1]

This work of thesis focuses the attention on two classes of photoactivable molecules, i.e., caged compounds and photosensitizers, with the attention at applications in the neuroscience and photodynamic therapy fields, respectively.

Caged compounds are realized via covalent appendage of a light-sensitive protecting group “the cage” to a signaling molecule. In particular, it was used as a GABA caged molecule (RuBi-GABA). One photon (UV-VIS light) and two-photon (700-900nm) absorption were used to break the “cage” binding[2]. The uncaged molecule (GABA) becomes active and can bind the $GABA_A$ receptor site generating a Cl^- current across the neuronal membrane that can be recorded using the Patch Clamp Technique. This approach allows controlling the neurotransmitter release in time, space, and relative concentration. In particular, the uncaging method and fluorescence microscopy coupled to the patch-clamp technique provides a useful approach to detect a selected biological target in a temporally and spatially confined way. In this thesis was analyzed how the change of physical parameters such as uncaging distance, exposure time, laser power, linear and non-linear photoactivation influence the measurements, and here I determined how these parameters change concentration and volume of GABA release and consequently the $GABA_A$ response. Specifically, localization precision can be improved using advanced fluorescent optical methods such as super-resolved and non-linear fluorescence microscopy[3]. This allows exploring the release of caged GABA topically applied *in situ* at defined concentration and in a specific region of neuronal cells for mapping the localization and the functional distribution of $GABA_A$ receptors in cerebellar granule cells *in vitro*. Finally, it was possible to explore the responses generated by specifics drugs in different regions of neurons.

Photosensitizers are photoactivable molecules that, after absorption of light, can produce reactive species of oxygen, which induce cell damage and death. When those molecules are targeted to cancer cells the process could lead to the death of tumor cells [4][5]. Such molecules are typically exploited in photodynamic therapy (PDT).

This treatment modality is not invasive and explicates its function by the simultaneous presence of a PS, visible light, and tissue oxygen. Indeed, these specific molecules can target and localize in the neoplastic tissue and, upon photoactivation with visible light, they generate reactive oxygen species (ROS), causing confined damage [6].

The reactive chemical species, and in particular singlet oxygen ($^1O_2$), are characterized by an active region of the order of 0.02 μm [7], where a series of reactions can produce oxidative damages and consequently cellular death for apoptosis or necrosis. The cellular death mechanism, such as apoptosis or necrosis, depends on (i) the cell line, (ii) the quantity of light, and (iii) the cell area in which the PSs accumulate [8]. Besides, these cellular damages could produce an immune response, improving therapy efficiency [9].

A particular class of PSs, such as hypericin, phthalocyanine, porphyrin, and curcumin, are an object of study for PDT.

However, a general characteristic and drawback of PSs is the low solubility in water and the aggregate formation, which impair their photophysical properties, such as the quenching of productive, excited states. To overcome this limit, PSs carriers were exploited. Among them, proteins offer several potential advantages. It has been demonstrated that PS molecules spontaneously bind internal hydrophobic cavities of particular proteins, preserving their monomeric, photoactive (both photosensitizing and fluorescent) state [12].

Proteins such as ApoMb and BSA were used as a carrier (ApoMb and BSA) for hypericin, phthalocyanine, porphyrin, and curcumin. These complexes were studied through advanced microscopical methods (spinning disk confocal, confocal, and STED microscopy) analyzing the difference in the use of PS or PS-protein complex, demonstrating how a protein can increase the PS efficacy. Therefore, were performed accumulation measurements, biocompatibility and bioavailability tests, colocalization measurements, and were studied the interactions of PSs with tumoral spheroids.

In summary, the main goals of this work are: (i) the study of cellular tumor damages induced by photosensitizing molecules and its localization in cells and the increase of its efficacy using protein carriers exploit advanced microscopy technique (ii) the study of $GABA_A$ receptor with the use of GABA caged molecule developing a set-up that combines confocal and two-photon excitation fluorescence microscope with patch-clamp technique.

Chapter 1: Photoactivation

1.1 Photoactivation theory

1.1.1 Molecular structure

To understand the spectroscopic characteristic of photoactivatable molecules, it is essential to have a quantistic approach to the molecular structure. The probability distribution of electrons in a molecular system is characterized by the wave function, Ψ, and its evolution is described by Schrödinger equation (for a non-relativistic particle):

$$i\hbar\frac{\partial}{\partial t}\Psi(\mathbf{r},\mathrm{t}) = \left(-\frac{\hbar^2}{2m_e}\nabla^2 + V(\boldsymbol{r},t)\right)\Psi(\mathbf{r},\mathrm{t}) \quad (1.1)$$

m_e and V represent particle mass of and its potential energy, respectively.

Solving the Schrödinger equation permits to find the presence of stationary states, also known as molecular orbitals. these states are described through time-independent equations.[13]

$$\hat{H}|\Psi\rangle = E|\Psi\rangle \quad (1.2)$$

It is possible to solve this equation analytically only for the case of H^+_2 molecule, but using Born-Oppenheimer approximation, it is possible to solve for a more complex molecule.

If we consider that nuclei move much slower than electrons in a molecule, then we can assume that electrons move in a fixed potential due to nuclei, while nuclei feel an average potential due to electrons.

The Born–Oppenheimer approximation is very reliable for ground electronic states, but it is less reliable for excited states.

The most straightforward approach is to consider H^+_2 ion in which all motion is confined to the z-axis. The hamiltonian is:

$$H = -\frac{\hbar^2}{2m_e}\frac{\partial^2}{\partial z^2} - \sum_{j=1,2}\frac{\hbar^2}{2m_j}\frac{\partial^2}{\partial Z_j^2} + V(z, Z_1, Z_2) \quad (1.3)$$

where z is the electron position and $Z_{1,2}$, of the two nuclei. It possible rewrite:

$$H = T_e + T_n + V \quad (1.4)$$

Schrödinger equation is:

$$H\psi(z, Z_1, Z_2) = E\,\psi(z, Z_1, Z_2) \quad (1.5)$$

splitting wavefunction ψ in electronic (φ) and nuclear (χ) wavefunction

$$\psi(z, Z_1, Z_2,) = \varphi(z, Z_1, Z_2)\chi(Z_1, Z_2) \quad (1.6)$$

After some mathematical handling it is possible to obtain:

$$\left(-\frac{\hbar^2}{2m_e}\nabla^2 + V\right)\varphi = E\varphi \quad (1.7)$$

where E is the total electronic and nucleus-nucleus repulsion energy for a stable nuclear conformation V is the potential energy of the electron in the field of the stable nuclei plus the nuclear interaction contribution described from the following Fig 1.1.

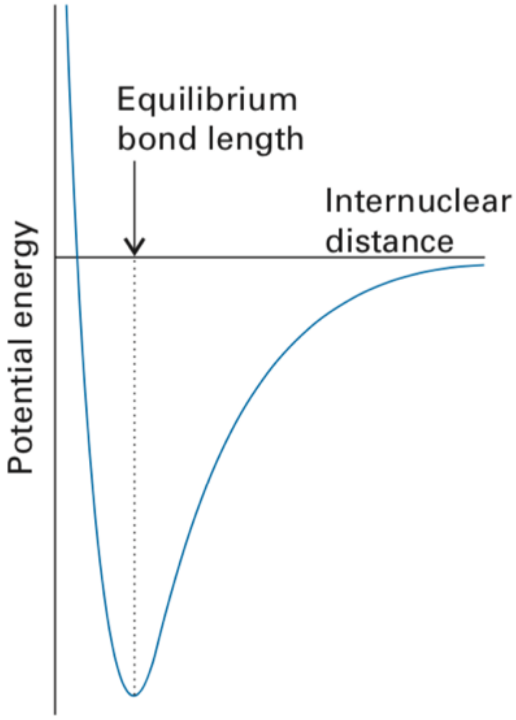

Fig. 1.1 Morse potential

Despite Born Oppenheimer approximation, the solution of the Schrödinger equation for H_2^+ is complicated. So, for solving more complicated molecules with more electrons, we need another approximation.

It is possible to write H_2^+ wavefunction such as linear combinations of hydrogen atomic orbitals:

$$\varphi^{+} \approx \Phi_a + \Phi_b \qquad \varphi^{-} \approx \Phi_a - \Phi_b \qquad (1.8)$$

Where Φ_a and Φ_b are hydrogen 1s-orbital of nucleus A and B. The two cases represent the electron density given from constructive and destructive interference of nuclear wave function. This method is called LCAO (linear combination of atomic orbitals)

For each of this wave function correspond two different energy orbital E^+ and E^-. The lower-energy orbital, given from φ^+ wavefunction, is called a bonding orbital. The higher-energy orbital, given from φ^- wave function, is called an antibonding orbital. When the electron occupies orbital bonding, the molecule is in its lower energy, so this configuration it helps the bonding of two nuclei; when it is in its antibonding orbital, the molecule energy raises and the two nuclei tend to be forced apart. Under inversion, the wavefunction ψ^+ remains indistinguishable from itself. In contrast, ψ^- change its sign, so the first one is classified as having gerade symmetry and the second one ungerade [14].

1.1.2 Absorption of light

An electronic transition is defined as an electron passage from a ground state of molecular orbital to an unoccupied orbital by absorption of a photon. In this case, the molecule is in an excited state. In absorption and fluorescence spectroscopy, two crucial types of orbitals are considered: the Highest Occupied Molecular Orbitals (HOMO) and the Lowest Unoccupied Molecular Orbitals (LUMO). [15]
The light absorption is due to the dipole interaction of the electromagnetic wave with the dipole moment of the molecule. If E_m and E_n are the energies of the initial and final molecular states respectively, it is possible to have absorption of light if and only if:

$$E_n - E_m = h\nu \quad (1.9)$$

Were $h\nu$ is the photon energy.
The transition probability from m to n state depends on the wavefunction of the ground and excited-state φ_m and φ_n, and of electric dipole moment operator μ:

$$\mu_{mn} = \int \psi_n \mu \psi_m d\tau \quad (1.10)$$

Were $d\tau$ is the volume element.

The dipole moment depends on three terms:

- an electronic transition moment, due on the nature of the electron distribution in the initial and final electronic spatial wavefunctions $\langle T_n|\mu|T_m\rangle$
- two overlap integrals related to the electronic spin $\langle S_n||S_m\rangle$ and the nuclear wavefunctions $\langle \chi_n||\chi_m\rangle$

$$\mu_{mn} = \langle \psi_n|\mu|\psi_m\rangle = \langle T_n|\mu|T_m\rangle\langle S_n||S_m\rangle\langle \chi_n||\chi_m\rangle \quad (1.11)$$

The electronic transition fulfills the Franck-Condon principle, that states that electron excitation by electromagnetic radiation occurs rapidly compared to nuclear motions. Thus, the nuclei remain permanently frozen during the transition. In this condition, the nuclear configuration remains the same during the transition. For this reason, the electronic transition is considered as a “vertical transition.”

*F*ranck-Condon factor ($\langle \chi_n \| \chi_m \rangle$) represents the overlap between the final and initial nuclear wave functions.

Since the electronically excited state thus generated can have different structural properties compared to the ground state. Therefore some changes in the nuclear configuration can take place after the transition.

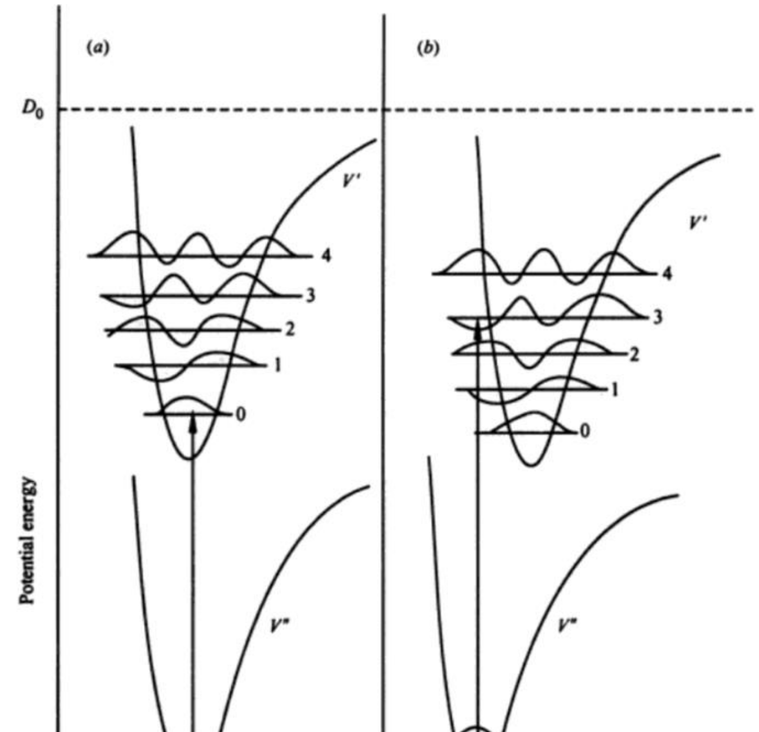

Fig. 1.2 Similar equilibrium geometry (a) different equilibrium geometry (b)

When there is the same nuclear equilibrium configuration, in the ground and the excited state, the most probable transition is the 0-0 (Fig. 1.2a), In contrast, if the nuclear configuration is different, the 0-0 is no longer the most probable, and the transition at a higher vibrational state became more probable (Fig. 1.2b).

This mechanism and the spacing of vibrational subbands together to electronic state distribution are fundamental for the shape of absorption spectra.[16]

The transition dipole moment also contains the spin overlap integral. When one of the two electrons of opposite spins is promoted to a molecular orbital of higher energy, its usually spin unchanged so that the total spin quantum number $S = \sum s_i$ remains equal to zero. Because the multiplicities $M = 2S + 1$ of both the ground and excited states are equal to 1, both are called singlet state, denoted S_0 for the ground state, and S_1; S_2 [etc.] for the excited states. This transition is called a singlet–singlet transition. Unchanging spin the spin overlap integral will be $\langle S_n||S_m\rangle = 1$. In some cases, the electron in singlet excited state can have a conversion that produces a spin inversion; having two electrons with parallel spins, the multiplicity will be 3. It is called the triplet state and is composed of three states of equal energy. In this case, spin overlap integral will be $\langle S_n||S_m\rangle = 0$

The electric dipole transition cannot induce changes in the spin state in the absence of spin-orbit coupling.[15]

1.1.3 Relaxing from an excited state

There are a variety of photophysical relaxing mechanisms for an excited molecule:

- Radiative processes where deexcitation to lower energy states occur through the emission of electromagnetic radiation (fluorescence, phosphorescence)
- Nonradiative processes where electronically excited states are transferred without emission of electromagnetic radiation

- Quenching processes (non radiative) where bimolecular interactions occur. In particular energy transfer of the excited state to other molecules take place.

A photophysical process is distinct from a photochemical process in that the former involves only changes in quantum states of a molecule and not its chemical nature. The schematic diagram, called the Jablosky diagram, shown in Fig. 1.3, is useful to represent absorption, emission phenomena, and some molecular processes

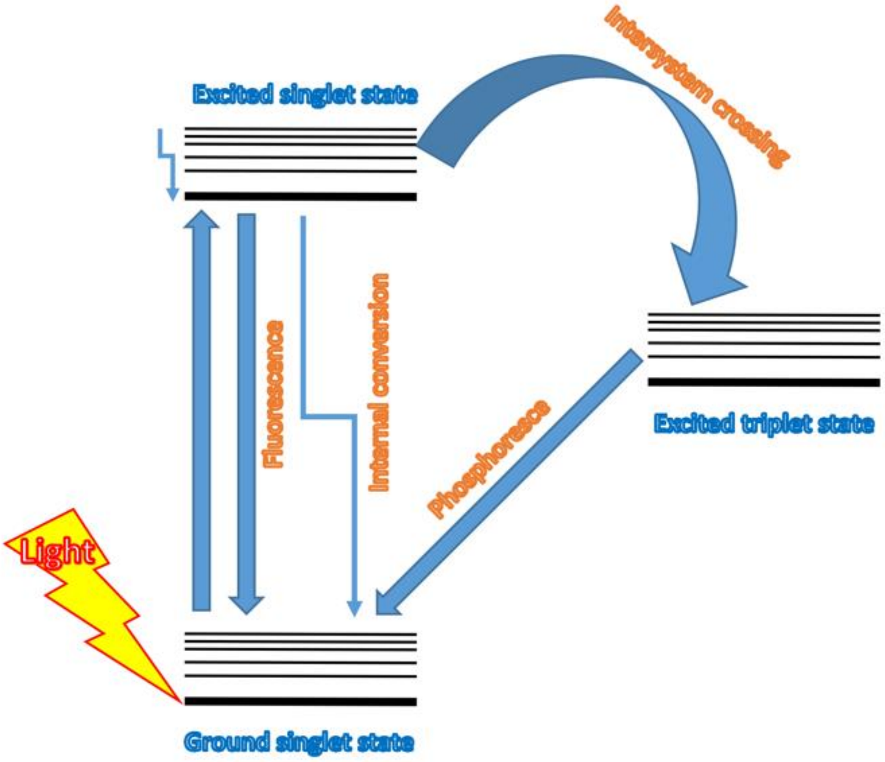

Fig. 1.3 Jablonsky diagram

In this diagram are represented the singlet ground states, the first excited state, and the first excited triplet state. Each electronic energy level of fluorophores is split into vibrational energy levels. Arrows depict the possible transitions between states. Absorption and emission occur mostly from molecules with the lowest vibrational energy.

The gap between the S_0 and S_1 electronic states is too large to have thermal excitation. At room temperature, thermal energy is not adequate to significantly populate the excited vibrational states. For this reason, we use visible light and not heat to induce fluorescence.

After light absorption occurs, a fluorophore is excited to a vibrational level of the first two electronic levels. It rapidly relaxes to the lowest vibrational level of S_1. This process is called internal conversion and generally occurs within 10^{-12} s or less. Since fluorescence lifetimes are typically near 10^{-8} s, the internal conversion is generally completed before emission. Hence, fluorescence emission generally results from a thermally equilibrated excited state, that is, the lowest energy vibrational state of S_1.

The return to the ground state typically occurs to a higher vibrational level of the ground state, which then quickly (10^{-12} s) reaches thermal equilibrium. An interesting consequence of emission to higher vibrational ground states is that the emission spectrum is typically a mirror image of the absorption spectrum of $S_0 \rightarrow S_1$ transition, as shown in Fig. 1.4

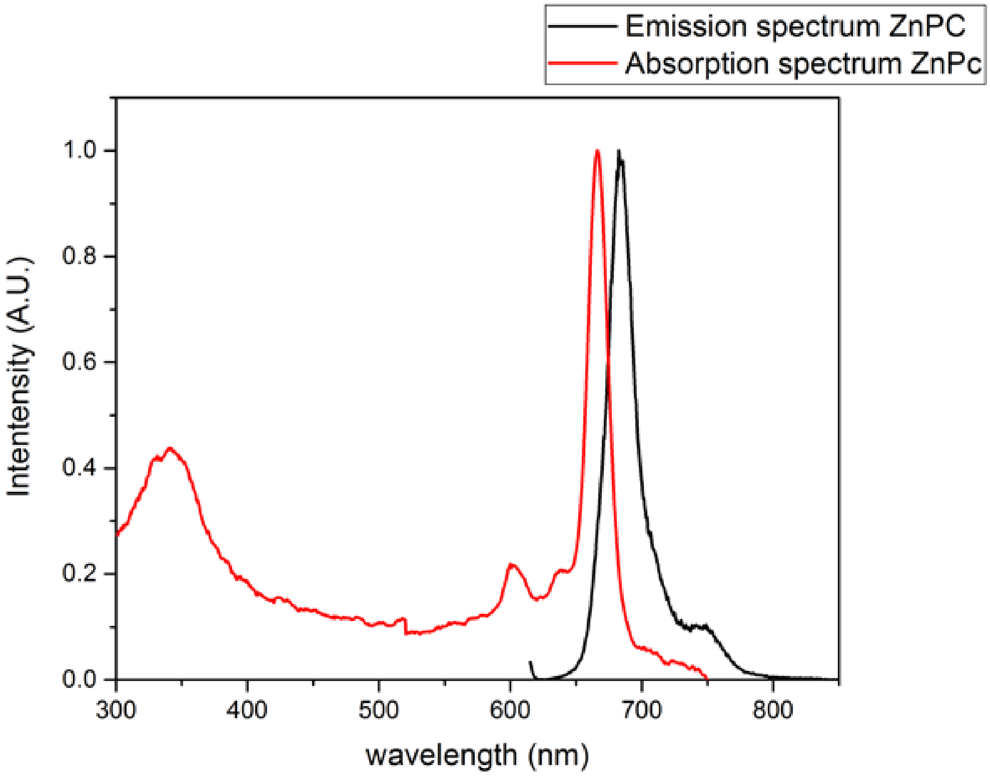

Fig. 1.4 Zinc Phthalocyanine absorption and emission spectrum.

Molecules in the S_1 state can also undergo a spin conversion to the first triplet state T_1. Emission from T_1 is called phosphorescence and is shifted to longer wavelengths relative to the fluorescence because the triplex excited state has lower energy in comparison with S_1 . Typically this phenomenon could be beaten by the back conversion to the excited S1 state leading to "retarded fluorescence”. The conversion of S_1 to T_1 is called intersystem crossing.

The transition from T_1 to the singlet ground state is forbidden, and as a result, the rate constants for triplet emission are several orders of magnitude smaller than those for fluorescence, and its lifetime is usually longer of 10^{-6} s. [17] As shown in Fig 1.4, there is a difference in the wavelength of the excitation and emission peak. This difference is due to the change in the equilibrium coordinates of the nuclear wave function that could be due to the interaction with solvent. Solvent molecules whose dipole moment interacts with the dipole moment of the fluorophore to yield an ordered distribution of solvent molecules around the fluorophore.

Energy level differences between the ground and excited states in the fluorophore produce a change in the molecular dipole moment, which ultimately induces a rearrangement of surrounding solvent molecules. Solvent molecules assist in stabilizing and further lowering the energy level of the excited state by re-orienting (termed solvent relaxation) around the excited fluorophore in a slower process that requires between 10 and 100 picoseconds. This has the effect of reducing the energy separation between the ground and excited states, which results in a redshift (to longer wavelengths) of the fluorescence emission Fig 1.5.

Increasing the solvent polarity produces a corresponding significant reduction in the energy level of the excited state while decreasing the solvent polarity reduces the solvent effect on the excited state energy level. The polarity of the fluorophore also determines the sensitivity of the excited state to solvent effects.

Polar and charged fluorophores exhibit a far stronger effect than non-polar fluorophores.

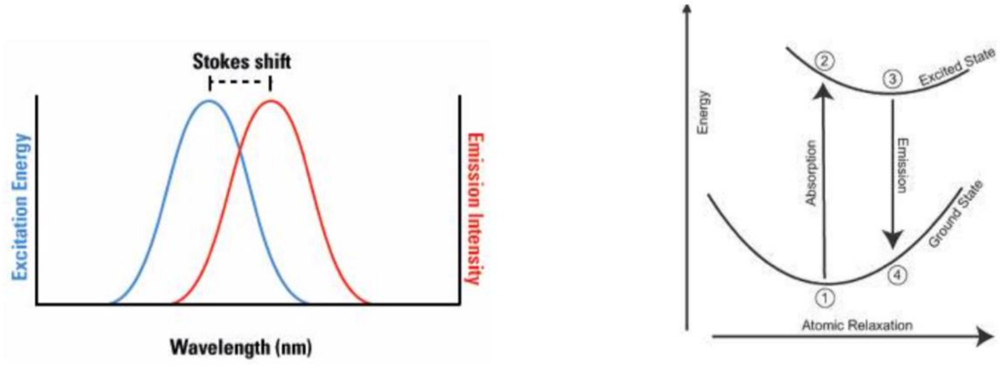

Fig. 1.5 Stock shift representation [17].

Fluorescence emission can be affected by the same mechanism that decreases its flurescence intensity, such as quenching. Quenching is due to different mechanisms. For example, collisional quenching occurs when the excited-state fluorophore is deactivated upon contact with some other molecule in solution, called the quencher.

These phenomena is described by the Stern Volmer equation:

$$\frac{F_0}{F} = 1 + k_q \tau_0 [Q]$$

K is the Stern-Volmer quenching constant that indicates the fluorophore sensitivity of quencher, k_q is the bimolecular quenching constant, τ_0 is the unquenched lifetime, and $[Q]$ is the quencher concentration. [17]

1.2 Photoactivation of the caged compound

1.2.1 GABA neurotransmitter

Neurotransmitters are molecules packaged in vesicles in presynaptic neurons, released in the synapse by fusion of the vesicles with the plasma membrane, and then taken back into the presynaptic neurons or postsynaptic cells. Transporters involved in the neuronal reuptake of the neurotransmitters and the regulation of their levels in the synaptic cleft belong to two significant superfamilies, High-affinity glutamate and neutral amino acid transporter and Na^+ and Cl^- dependent neurotransmitter transporter. Transporters in both families play roles in reuptake of neurotransmitters like γ-aminobutyric acid (GABA), glutamate, and the monoamine neurotransmitters norepinephrine, serotonin, and dopamine. These transporters may serve as pharmacological targets for neuropsychiatric drugs. [18]

Gamma-aminobutyric acid (GABA) is the primary inhibitory neurotransmitter in the mammalian central nervous system (CNS). It is known that GABA mediates most inhibitory transmission events in the vertebrate brain [19], and GABAergic signaling plays an essential role in the development of CNS [20].

Some drugs can enhance inhibitory neurotransmission include benzodiazepines, barbiturates, and general anesthetics and are used as a sedative and for the treatment of some neurological diseases [21].

1.2.2 GABA Receptor

GABA can interact on the different receptors as $GABA_A$ and $GABA_B$ types. [20]

These receptors differ in molecular structure, signal transduction mechanism, distribution, function, and pharmacological profile.

The object of the study of this work is the $GABA_A$ receptor.

$GABA_A$ receptors are ligand-dependent protein channels and represent the primary mechanism by which GABA can transfer a rapid inhibitory signal (in the order of few milliseconds).

Cl^- is the ion for this receptor and fixes the value of the membrane potential (- 70 mV).

Activation of this receptor reduces, through hyperpolarization, the probability of having an action potential that decreases the excitability of the cell. [22]

The $GABA_A$ receptor is a pentameric complex composed of several subunits.

There are 16 subunits, α1-6, β1-3, γ1-3, δ, ε, θ, and π [23] the combination of different subunit classes leads to the formation of $GABA_A$ receptors with different pharmacological properties. *In vivo*, generally, it is composed of the isoform 2α, 2β, and γ subunits [20]. GABA binding site is located between the subunits α and β.

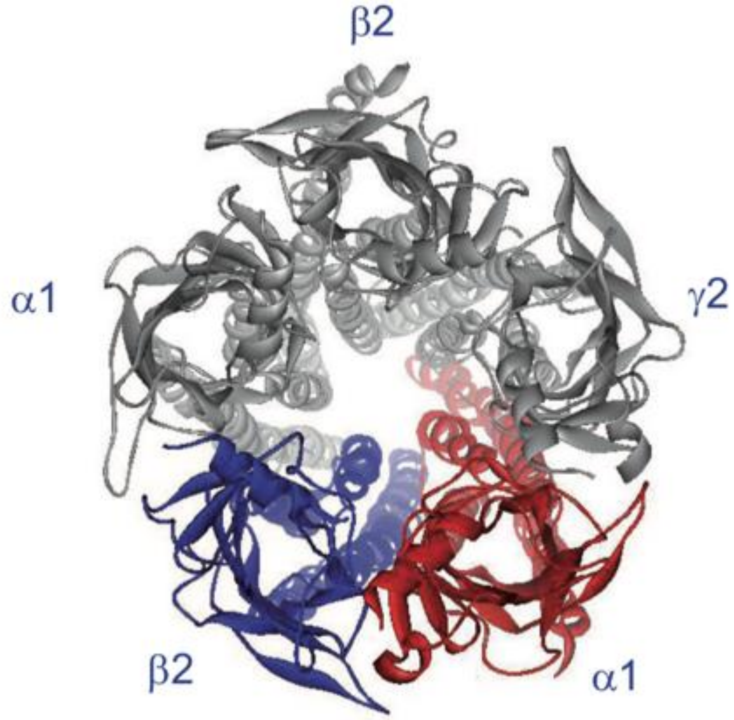

Fig. 1.6 GABA$_A$ receptor structure

GABA$_A$ Receptor presents several binding sites for different drugs such as benzodiazepines, barbiturates, neuroactive steroids, anesthetics, and convulsants that change the interaction with GABA neurotransmitter.

Interaction of these drugs with GABA$_A$ receptor allows modulating anxiety, the excitability of the brain, muscle tonus, […] [24].

For these reasons, the GABA$_A$ receptor is an essential object of study for pharmacology.

1.2.3 Uncaging (RuBi-GABA)

Caged compounds are composed of biological effector molecules whose active functionality has been chemically masked with a photoremovable protecting group. These compounds produce a high impact of interest in neuroscience, because of the capability of the localized release of neuroactive molecules in a well-defined area of a neuron; this represents a new approach for the study of receptor localization and channel kinetics. [25]

Caged molecules must have the same characteristics as those used for neuroscience applications. It must not produce a response before illumination and must be hydrolytically and enzymatically stable during the experiment.

It must not be agonist or antagonist for cellular receptors and must not be toxic.

Uncaging has many useful features and advantages compared to other technologies for changing solute concentration around or inside living cells. These include:

1. *Intracellular release.* Being cell transparent, the inner part of the cell is accessible to uncaging technique

2. *Speed of release.* Uncaging time is of the order of sub-micro seconds to milliseconds, so it is swift and allows quantifying the channel kinetics.

3. *Timing of release.* The caged compound is inert until photoactivated. It can activate molecules at a specific time during the experimental time course.

4. *Location of release.* The position and the volume of photoactivation are defined and confined.

5. *Quantification of release.* It is possible to calibrate in a specific experimental parameter uncaging efficiency. It allows quantifying the number of uncaged molecules. [26]

There is a large variability of a different caged and neuroactive molecule, for example, GABA [2], glutamate [27], nicotine [28] […] in this work of thesis the object of the study is caged RuBi-GABA, a compound where GABA is bound to ruthenium-bipyridine- triphenylphosphine.

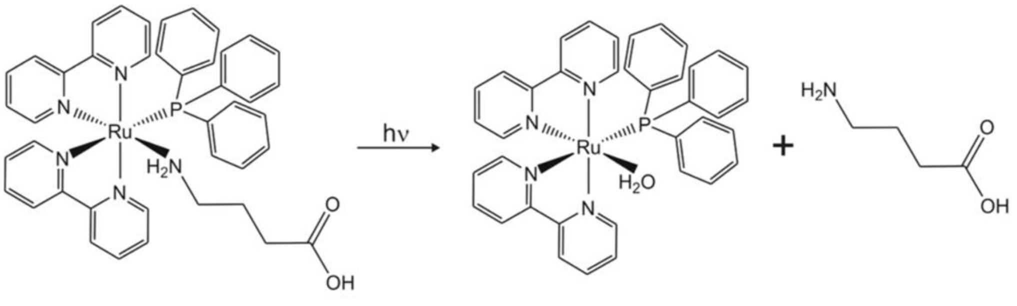

Fig. 1.7 RuBi-GABA structure in the cage and uncaged form [2]

This molecule presents different advantages: in fact, it has a high quantum yield of uncaging. It can be uncaged using visible light instead of UV light, so it is possible to prevent DNA damage, and it is possible to increase light penetration [2]. At last, but not least, this molecule is photoactivable using two-photon excitation.

1.3 Photoactivation of Photosensitizer

1.3.1 Photodynamic therapy

Light is used for the treatment of various diseases over 3000 years. Some civilizations, such as Egyptians, Indians, and the Chinese, used light for the therapy of psoriasis, rickets, and vitiligo. In Denmark, at the end of the XIX century, Niels Finsen discovered that red light allows treating smallpox pustule to prevent its formation, while the use of ultraviolet light coming only from the consent to treat cutaneous tuberculosis. This was received by modern "phototherapy" so that in 1903 Finsen was awarded the Nobel Prize for his discoveries.

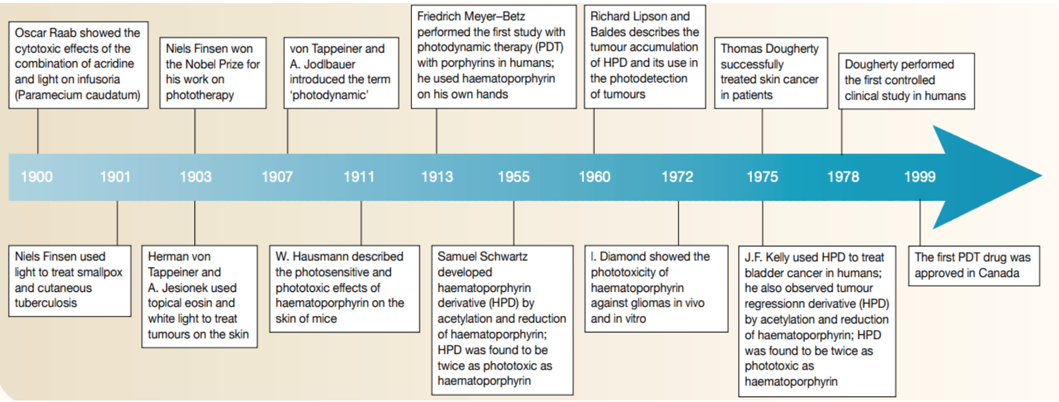

Fig. 1.8 History of photodynamic therapy [6]

Furthermore, more than 100 years ago, researchers observed that cell death could be induced by the combination of light and certain chemicals. In particular, in 1900, the German medical student Oscar Raab observed that the simultaneous presence of acridine and light of specific wavelengths has a lethal effect on some biological matter, including a kind of Paramecium. In conclusion, this therapy exploits three individually non-toxic components which, combining appropriately, can induce damage to cells and tissues [6]:

- A photoreactive agent called photosensitizer;
- Light of appropriate wavelength;

- Tissue oxygen.

Photodynamic therapy offers several advantages over traditional methods of anticancer treatment, such as surgery, radiotherapy, or chemotherapy. Since it is possible to direct light activating photosensitizers towards the neoplastic tissue, using modern optical fibers and various types of endoscopes [29], the method is less invasive. However, the primary advantage of this technique is given by the photosensitizing agent. With a suitable carrier, It can accumulate with a and can be preferably retained in the neoplastic tissue rather than in the surrounding healthy tissues.

1.3.2 How to act photodynamic therapy

Clinical treatment of PDT can be divided into four phases:

- Administration of the drug;
- Accumulation in the tumor;
- Activation of the photosensitizer;
- Generation of cytotoxic species and cell death;

When a photosensitizer is illuminated with visible light of appropriate wavelength, it can absorb a photon undergoing excitation at the singlet electronic state, S_1.

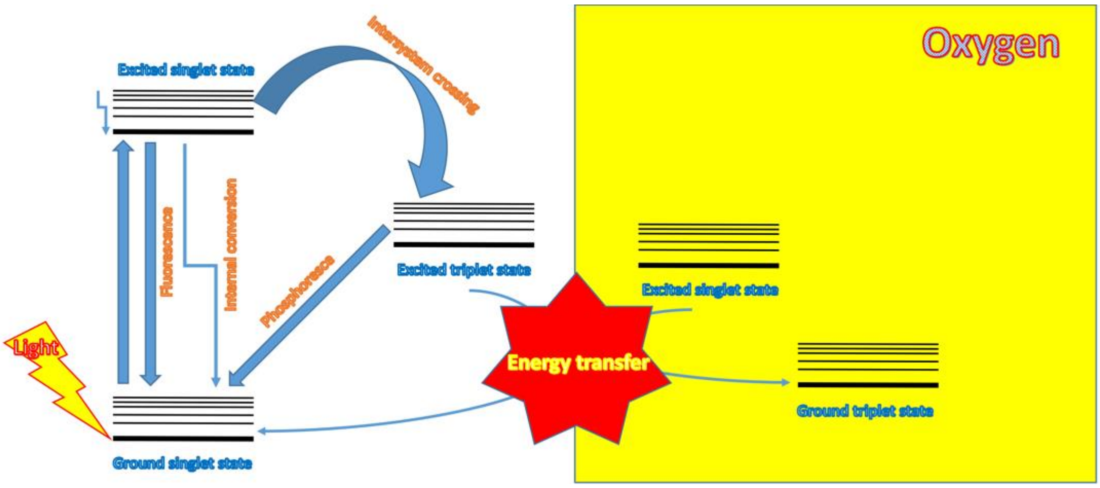

Fig. 1.9 Jablonsky diagram of PS-oxygen interaction

As shown in chapter 1.1.3, some molecules can undergo inter-system crossing (ISC) from singlet to triplet state, S1 -> T1. This process, prohibited by the selection rules, is favored by spin-orbit coupling effects. The further de-excitation in the ground state S0 requires a second prohibited transition. Therefore, the lifetime of the T1 species is much longer, of the order of micro / milliseconds, and is enough to allow energy transfer with surroundings molecules, hence generating cytotoxic species. In particular, two different reactions can be involved:

Type I reactions.

A charge transfer occurs from the photosensitizer in the T1 excited triplet state to biological substrates (unsaturated lipids, steroids, aromatic amino acids), with consequent formation of radical species, which in turn react with oxygen molecules to produce reactive oxygen species. These intermediates are highly reactive and strongly oxidizing, such as superoxide anion, hydrogen peroxide, and hydroxyl radical.

Type II reactions.

There is a direct energy transfer from the photosensitizer in the triplet state to the molecular oxygen ($^3O_2$) to form singlet oxygen ($^1O_2$) which, has a crucial role in the in anticancer treatment by PDT.

The two reaction types do not occur in a mutually exclusive manner, but they can contribute together to the final therapeutic effect.

The magnitude of oxidative damage caused by ROS strictly reflects the intracellular localization of the photosensitizer, due to the short lifetime of ROS that prevents them from traveling longer than a few tens of nanometers. In particular, oxygen in the singlet state has a half-life few than 4 μs, and this time interval allows it to spread to a distance not longer than 0.02 μm. So, the oxidative damage can be precisely confined to the diseased cells targeted by the therapy, preserving the surrounding healthy tissues [7].

1.3.3 Photosensitizer

A photosensitizer is defined as an atom or a molecule that absorbs radiant energy, usually visible light, consequently move to an excited electronic state, and subsequently transfers the excitation energy to another atom or molecule.

There are several features that a photosensitizer must have to be suitable for photodynamic therapy, including [7][30]:

1) It must be available in pure form, and of known chemical composition;

2) It must be synthesizable from precursors available and easy to reproduce;

3) A high quantum yield of singlet oxygen production ($\Phi\Delta$);

4) A high absorption in the red region of the visible spectrum (680-800 nm) with a high molar extinction coefficient (ε) of the order of 50,000 - 100,000 M^{-1} cm^{-1}.

This range is determined by the fact that in the organism, below the 680 nm scattering phenomena and strong absorption by endogenous chromophores are observed, which limits the penetration of light. On the other hand, at wavelengths exceeding 900 nm, light has not enough energy to generate singlet oxygen.

5) Photostability and no toxicity in the absence of light (dark toxicity) in order to prevent side effects at high doses;

6) Sufficient energy of the excited triplet electronic state, which must be higher than 94 kJ mol to allow the transition between the fundamental state of oxygen and the first excited state of singlet;

7) A preferential biodistribution in tumor tissues;

8) A quick molecule elimination to avoid skin photosensitization effect;

9) Excellent solubility in pharmaceutical formulations and in body fluids

The first generation of photosensitizers used for PDT was a derivative of hematoporphyrin. It consists of a complex mixture of porphyrins in the form of monomers and oligomers. Thus Photofrin® was formulated in 1995 was approved by the FDA as a photodynamic agent for PDT and had high popularity for the treatment of various tumors [30]. Nevertheless, Photofrin® does not respond to many characteristics proper to an ideal photosensitizer:

- It is difficult to reproduce the composition mixture
- There is a modest biological activity, with a low molar extinction coefficient in the red band at 630 nm ($\varepsilon \sim 1170$ M^{-1} cm^{-1}).

- High doses are necessary.
- Low selectivity for the target tissues.

This leads to numerous side effects, such as skin photosensitization [7].

Limitations of first-generation photosensitizers, bring production of new molecules with better properties, leading to developing second-generation photosensitizers which have a higher absorption and molar extinction coefficient at longer wavelengths and high chemical purity.

The major limitation of this second generation of drugs is the inefficient selective accumulation of photoactive agents in the diseased tissue and its aggregation propensity, which leads to significant side effects.

To overcome this problem, the use of several biomolecules such as: monoclonal antibodies, lecithins, peptides, hormones, folates, and ligands, that are selective for receptors overexpressed in tumor cells combined with the photosensitizer gives a major selectivity. the photosensitizer development leads to giving higher drug selectivity combining them with biomolecules, such as monoclonal antibodies, lecithins, peptides, hormones, folates, and ligands for receptors overexpressed by tumor cells. Thus was born the third photosensitizer generation. This is based on the combining second-generation photosensitizers with carriers, allowing:

- Make soluble molecules in water-based fluids (increase bioavailability);
- Giving selectivity (targeting);
- Increase the fluorescence emission;
- Increase biocompatibility.

1.3.4 Protein carrier system

Protein carrier systems result to be an interesting solution for the delivery of photosensitizers. Since we choose proteins that are endogenous in the organism, the biocompatibility is fully preserved, minimizing undesired effects. Nevertheless, the use of proteins could allow a simple binding (see chapter 3.10).

In this thesis, I focused my attention on two specific proteins, myoglobin and albumin.

Myoglobin

Myoglobin is a globular protein that can bind oxygen. It is present with a high concentration in human muscles and its function of oxygen reserve.

Myoglobin was the first protein whose three-dimensional structure was determined through X-ray crystallography. α-helices mostly form myoglobin joined together by folds to form a globular structure. In particular, it consists of a single polypeptide chain of 153 amino acid residues and has a size of 45x35x25 Å and a molecular weight of 17,000 Da. To this polypeptide chain to which heme (Fe-protoporphyrin IX) is covalently attached and the iron atom of the heme is directly bonded to the proximal histidine (His93) [31]

About 70% of the structure of myoglobin is organized in the form of eight α-helices, wrapped around the heme and histidine-93 called proximal (below) and histidine-64 called distally (above); while the rest of the polypeptide chain forms folds and loops. Four cavities are present in the protein, determined by Xenon diffraction X-linked studies, stylized in the figure as black spheres [32].

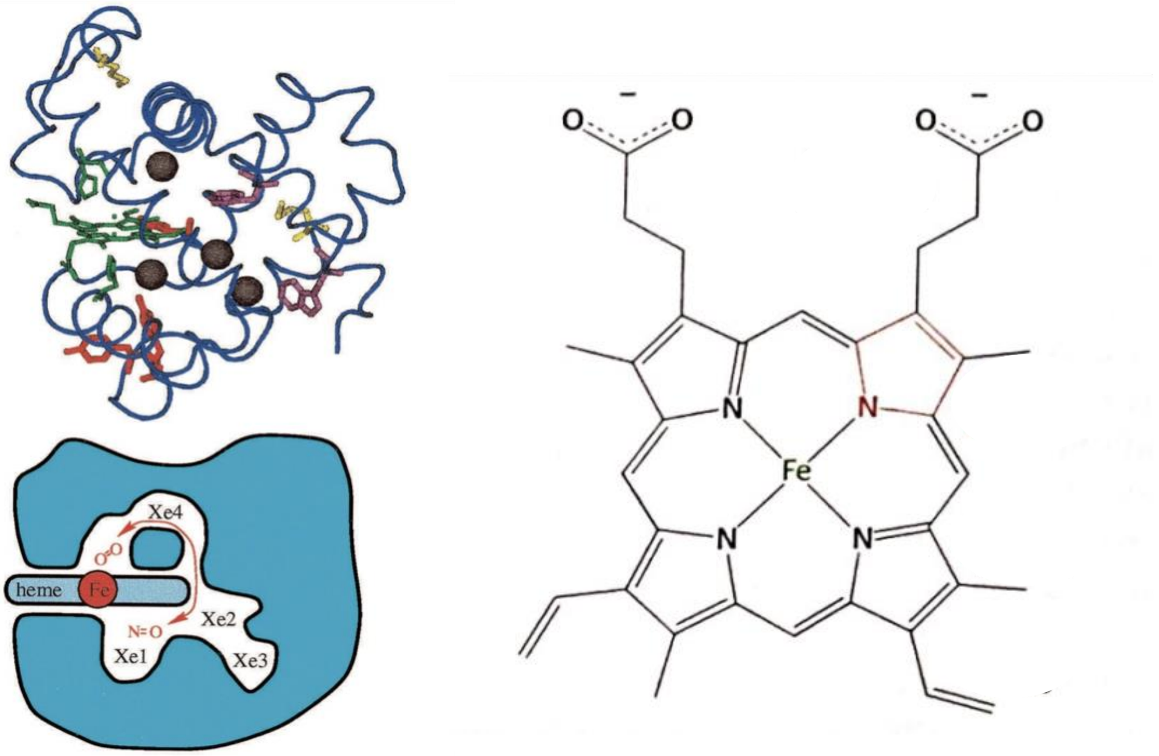

Fig. 1.10 Apomyoglobin (left) and HEME (right) structures.

The ability of myoglobin to bind oxygen depends on the presence of a prosthetic group, called heme. The red color of the muscle and blood is due to the presence of the heme, consisting of a non-protein organic component and a central ferrous ion. The organic component is called protoporphyrin and consists of four pyrrole rings linked by methyl bridges. Four methyl groups, two vinyl groups, and two propionate side chains are bound to the tetrapyrrolic ring thus formed. The iron atom is located in the center of protoporphyrin and is linked to the four nitrogen atoms of the pyrrole rings. When myoglobin is deprived of its heme cofactor, the remaining protein matrix is called apomyoglobin.

Apomioglobin can be derived from myoglobin with a chemical protocol that exploits a partial acidic denaturation of the protein [33]. It is generally used for studies and developments of complexes with molecules different from heme bound within the protein cavity.

Albumin

Serum albumin is an abundant multifunctional protein and is the main protein component of blood plasma, but it can also be found in body tissues and secretions. The primary role of albumin is to transport fatty acids. Thanks to its versatile ability to bind various molecules and its high concentration in the body, it has a series of additional functions, which include the maintenance of osmotic blood pressure and the detoxification of the organism from carcinogenic metabolites, such as bilirubin [34].

Albumins are a monomeric protein composed of 585 amino acids with a total molecular weight of 66400 Da. The protein is 67% α-helicoidal and utterly free of β-sheet. They are organized into three homologous domains (named I-II-III), and each of these is composed of two subdomains (A and B) that share common structural elements. A total of 17 disulfide bridges, which are exclusively inside the subdomains, give the albumins a high thermostability.

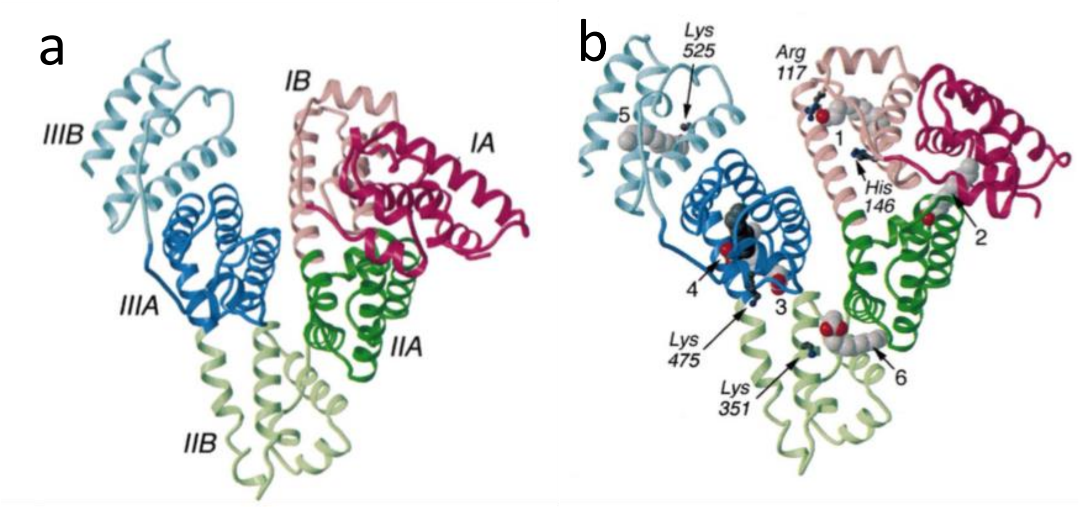

Fig. 1.11 (a)Albumins structures and (b) binding sites.

The albumin's crystalline structure revealed six possible binding sites for fatty acids and showed that a conformational change in the protein accompanies bonds with one of these. In five of the six sites (numbered 1-5), where there is a high electron density, fatty acids are bound. The sixth site at the interface between IIA IIB, in which there is a fragmented electron density, does not allow to host an entire molecule [34].

Two of these five sites are particularly crucial for reversibly binding many drugs. The first is found in the IIA subdomain, called the Drug 1 site, in which abundant heterocyclic compounds are bound, mostly without a carboxyl group. The second site, called drug site II, is located in the IIIA subdomain and is preferred by compounds with an aromatic ring or carboxylate groups which have a very large conformation [35].

1.3.5 Targeting

Targeting is based on the use of carrier systems. It transports drugs selectively to the active site. Targeting strategies can be multiple:

- Passive targeting. It is observed that photosensitizer accumulation in tumors site increase with its hydrophobicity. However, hydrophobic PSs show aggregation problems, so intravenous treatment is dangerous. Therefore, most of the PSs currently in use are encapsulated within hydrophilic molecules or structures such as liposomes, protein, polymer, and particles. Furthermore, these formulations showed an increase in photosensitizer concentration in tumors [36].

Passive targeting of vector and encapsulated drug is possible thanks to the physicochemical properties of the construct, e.g., size, hydrophilicity, and surface charge. Such parameters determine its biodistribution. Another essential characteristic is the alterations of physiological conditions caused by neoplastic tissue. It can produce severe damage to the lymphatic tract, which allows further accumulation of the molecules transported in the tumor interstices. This particular concept, called the "EPR effect" (Enhanced Penetration and Retention), explains how carriers passively reach the tumor releasing the encapsulated molecules in the desired site [37].

- Active targeting. This takes advantage of the altered density of some receptors in tumor cells allowing the use of specific carriers to target photosensitizers [38].

For example, monoclonal antibodies can be exploited to give photosensitizer selectivity. The idea develops around the recognition of these antibodies for some overexpressed markers on the tumor cell surface that can be used as a "linker" between the photosensitizer and the cells cancer [39].

Chapter 2: Microscopy and electrophysiological Methods

2.1 Advanced fluorescence microscopy and nanoscopy

Microscopy allows studying objects that are too small for the naked eye. A microscope is an optical system that transforms an 'object' into an 'image'. The idea is to make the image much larger than the object, that is magnifying it, and exist different microscopy techniques in which this can be done [40], such as:

- Atomic force microscopy uses a cantilever to probe the surface of the sample.

At the end of the cantilever, a sharp tip is mounted to sense the force between the sample and tip.[41]

This technique offers a fully three-dimensional view of the sample's surface, without requiring a coating that alters the sample. So, AFM result suitable for biological samples analysis.[42]

- Electron microscopy is based on the use of an accelerated electron beam for investigating the sample. Thanks to shorter wavelengths of radiation this technique allows a high-resolution level. There are two main classes of microscopy: scanning electron microscopy (SEM) and transmission electron microscopy (TEM). Both of them are exploited for 2D and 3D materials characterization[43]. At the simplest level, a SEM can be thought of as providing images of external morphology, while TEM probes also the internal structure of solids.[40]

- Optical microscopy exploits visible light (400-700nm) and its interaction with the matter to acquire an image of the sample.

The use of visible light results particularly interesting for biological specimens. It is not invasive and allows three-dimensional subcellular studies in physiological conditions.

Numerous transmitted light microscopy approaches such as phase-contrast, differential interference contrast (DIC), and polarized microscopy allow enhancing the inherent contrast of living specimens in order to make some details visible. Nonetheless, the exploitation of fluorescence results particularly interesting. This technique exploits some engineered fluorescent indicators that have the capability to bind some specific target, e.g., proteins, lipids, or ions. Their use was the biggest step forward in order to study cell physiology. The use of a fluorescence microscope has the aim of being specific, increasing image contrast and spatial resolution. Consequently, most of the recent advances with fluorescence microscopy have sought to improve image quality by addressing the fundamental problem of image resolution, which is determined by noise, contrast and diffraction of light within an optical system. [44]

2.1.1 Point spread function

Position accuracy refers to the precision with which an object can be localized in space. Spatial resolution is defined as the capability to discriminate two separate objects from a single one. [45]

The point spread function (PSF) can be considered a measure of the resolving power of an optical system. The smaller the point spread function, the better the resolution will be. As the name implies, the point spread function defines the spread of a point source. If we have an infinitely small source of light, it will appear with a finite size.

The image $I(x)$ of a specimen produced by an optical microscope can be described as a convolution between the object (specimen) $O(x)$ and the point spread function $P(x)$:

$$I(x) = \int P(x - x')O(x - x')\, dx'$$

The PSF depends on the optical system but can be locally distorted because of aberrations introduced by the specimen or imperfections of the optical setup.

Neglecting the aberration components, it is possible to estimate the diffraction limit. This implies that optical resolution is ultimately limited by the wavelength of light and focusing power.

The image of an infinitely small luminous point object is not infinitely small but is a circular Airy diffraction pattern with a bright central disk and progressively weaker concentric dark and bright rings. The radius r_{Airy} of the first dark ring around the central disk of the Airy diffraction pattern depends on the wavelength of light, λ, and the numerical aperture, NA, of the objective: [46]

$$r_{Airy} = 0.61\,\frac{\lambda_0}{NA}$$

Following Rayleigh criterion, that relies on the assumption that the two-point sources radiate incoherently, two points of light separated by a distance d will be resolved if *d* is larger or equal to the radius of the Airy disk.

2.1.2 Introduction: from wide-field to confocal

The most simple fluorescence microscope is the Wide-field microscope. It works illuminating all the samples with the light of suitable wavelength and the response of the sample, in fluorescence, is collected by a camera. The fluorescence is opportunely filtered by a dichroic filter. [47]

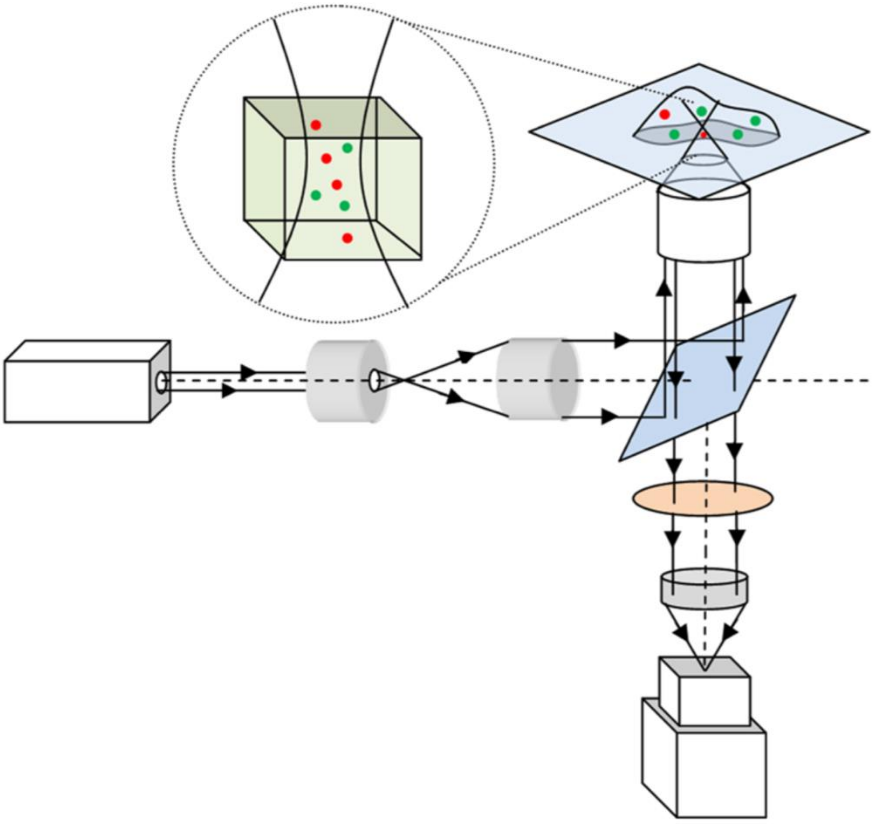

Fig. 2.1 Wide-field microscope scheme. [47]

Wide-field microscopy presents several advantages. Being all the image area illuminated at the same time it allows faster imaging limited only by camera acquisition capabilities. Wide-field imaging generally allows lower excitation power that brings less photobleaching and phototoxicity.

However, being optics governed by diffraction and collecting fluorescence of different out of focus planes in a single image, the final image has both a limited spatial resolution and a low contrast respectively. The lateral resolution is defined by Abbe’s law and two nearby objects can be resolved following, for instance, the Rayleigh criterion, [44] three-dimension sectioning is also possible and can be achieved by exploiting computational methods based on deconvolution. [48] The more advanced deconvolution methods attempt to reassign this out-of-focus light to its point of origin (i.e., converting airy rings back into single point sources of light); the resulting image should be sharper with better contrast and under certain circumstances with increased Z resolution [49]

2.1.3 Confocal Microscopy

Confocal microscopy is the first step towards higher resolution. Differently from Wide-field microscopy, it allows rejection of the out of focus signal thanks to the use of the pinhole, and it improves contrast, resolution and enables 3D mapping of the specimen. [47]

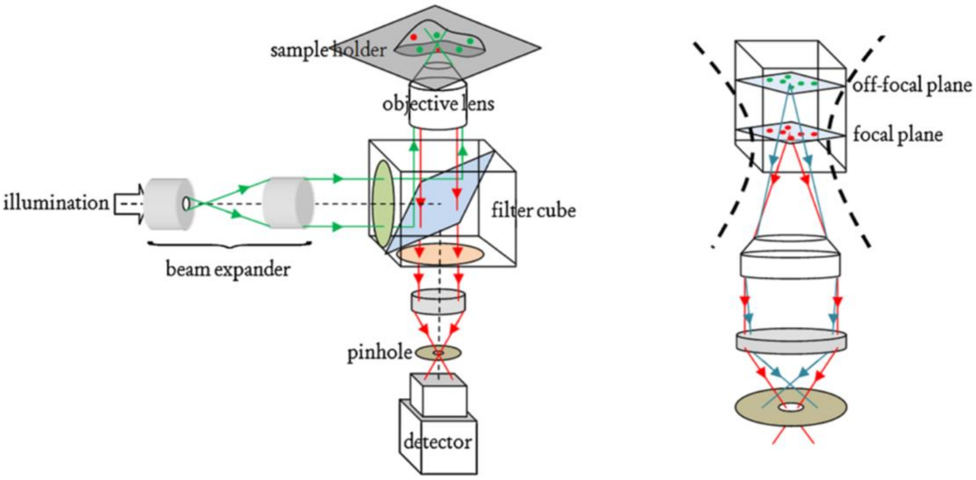

Fig. 2.2 confocal microscope scheme. [47]

The small pinhole is placed in a conjugate focal plane. This allows, to the only photons, emitted in the focal point, to pass through the pinhole for being recorded. Both any light outside of the focal plane and the scattered light is blocked by the screen. [50] This microscope brings in the concept of point-by-point scanning of the specimen. There are two primary scanning technique, laser-scanning, and disk-scanning.

Laser-Scanning

This technique allows imaging the specimen one “point” at a time. To create an image of the specimen, the focal spot is rapidly and serially scanned in the *X–Y* plane, usually using a galvanometric mirror [51] or a stage motion (Marvin Minsky patent 1957).

Point by pointing it fluorescence signal pass from pinhole and a dichroic mirror and is collected by a sensitive detector such as a photomultiplier. The fluorescence intensity was acquired by a computer that will reconstruct the image.

Disk scanning

Disk scanning uses an alternative design. It is composed of a spiral-perforated disk, i.e., a Nipkow disk. Such a disk contains thousands of pinholes arranged in a spiral track. When the disk is spinning, the moving pinholes could cover the whole field of view, and signals were acquired by CCD camera. By spinning thousands of points simultaneously, the Nipkow disk can achieve a real-time confocal image.[52][50] In comparison to laser-scanning, this approach results faster with less bleaching and photo-toxicity.

2.2 Super-resolution Fluorescence Microscopy

A confocal microscope could reach and, to some extent, overcome the resolution limit of a lens. Considering a confocal microscope equipped with perfect lenses, optimal alignment, and large numerical apertures, the optical resolution is approximately half of the wavelength of the light used. This limit means that cellular structures and objects that have dimensions of at least 200 to 350 nm could be resolved by light microscopy. How it is understandable, the majority of the fundamental biology of cells happens at the dimension of macromolecular complexes ranging from tens to a few hundred nm.[53] This challenge produced an extensive study on the possible methods for overtaking the diffraction limit that culminated in 2014 with the Nobel prize awarded to Stefan Hell, Eric Betzig, and William Moerner for the development of super-resolved fluorescence microscopy.[54–56]

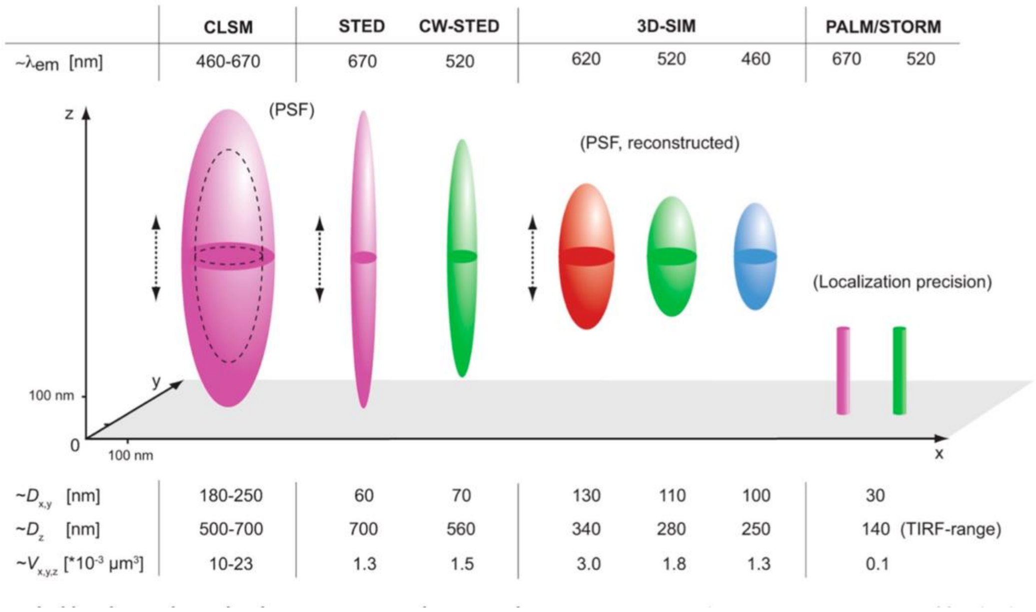

	CLSM	STED	CW-STED	3D-SIM			PALM/STORM	
~λem [nm]	460-670	670	520	620	520	460	670	520
$\sim D_{x,y}$ [nm]	180-250	60	70	130	110	100	30	
$\sim D_z$ [nm]	500-700	700	560	340	280	250	140 (TIRF-range)	
$\sim V_{x,y,z}$ [$*10^{-3}$ µm^3]	10-23	1.3	1.5	3.0	1.8	1.3	0.1	

Fig. 2.3 PSF of different microscopy technique. [53]

Recent innovations have led to the development of three leading alternatives for super-resolution microscopy that effectively break this diffraction limit: stimulated emission depletion microscopy (STED), stochastic optical reconstruction microscopy (STORM) / photoactivation localization microscopy (PALM), and structured illumination microscopy (SIM), .[57][58]

- STED exploits stimulated emission promoted by a second laser beam to turn off fluorescence emission of fluorophores located in the surrounds of the excitation center, allowing to sharpen the excitation PSF (see the following section for more details). [59–61]
- PALM/STORM uses photo-switchable fluorescent dyes that allow the separation in time of activation and detection of single molecules. Since the activation process is achieved randomly in space, it is possible to localize each fluorescent molecule and, therefore, each protein or structure, which is attached. The localization of each fluorescent molecule will have an uncertainty determined by the PSF and the number of photons emitted N, leading to a localization precision approximated by:

$$\Delta_{\mathrm{loc}} \approx \frac{\Delta}{\sqrt{N}}$$

where Δ_{loc} is the localization precision, and Δ is the size of the PSF. Since the localization precision depends on N the final resolution limit is only defined by the label itself. [62]

- SIM uses a series of sinusoidal striped excitation patterns with a high spatial frequency to illuminate the sample. Such a structured illumination allows retrieving higher spactial frequencies than a conventional microscope. The illumination pattern is typically generated by laser light passing through a movable optical grating and projected via the objective onto the sample. The method requires the acquisition of an image for each position and rotation of the pattern. The recorded images are linearly processed to extract the high spatial frequencies that are the smallest details and to generate a reconstructed image with twice the standard resolution. [63]

2.2.1 STED Microscopy

A typical STED nanoscope is based on a confocal microscope. It needs at least two coaligned laser beams: one for the excitation and a second for the fluorescence depletion. STED microscopy is based on the saturation of the stimulated emission process, which allows the instantaneous de-excitation of the excited fluorophore. The technique is realized illuminating the sample with a gaussian excitation beam aligned with a depletion beam, called the STED beam. This latter beam has a donut shape with a zero intensity at the center. This particular shape is obtained using a vortex phase plate. The two-beams combination allows shrinking the effective PSF depending on the reached saturation level of stimulated emission process, thus on the depletion beam power. Current experimental setups routinely achieve a resolution in the range of 30–80 nm. [53]

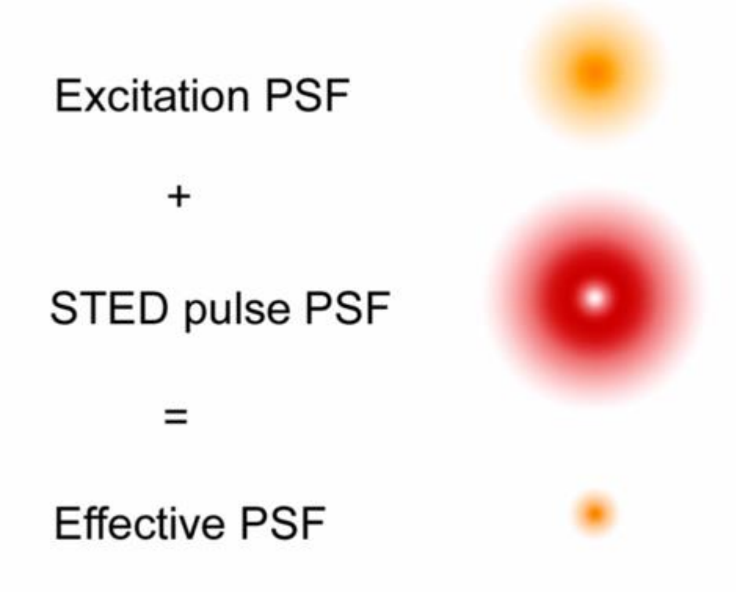

Fig. 2.4 STED excitation, depletion beam, and PSF. [53]

Lasers have a primary role in STED microscopy. Quenching is optimized when depletion occurs shortly after fluorophore excitation, so STED microscopy is typically implemented with pulsed lasers. [60]

In a pulsed STED microscope, while the donut should always show a proper zero at the center, the depletion pulse must be synchronized with the excitation one and have a correct duration. A pulse width of τ STED ≈20–30ps would exploit the available STED power maximally and would yield the steepest decrease of the probability of spontaneous decay with increasing saturation factor . [64]

Therefore, to obtain an excellent Spatio-temporal STED alignment, we take particular care on polarization, pulses delays, optical stability, and beam alignment.[61]

Another critical parameter in STED microscopy is the wavelength of the depletion beam. The STED beam stimulates the emission of fluorophores, instantaneously bringing them to the ground state emitting a photon of the same wavelength of the depletion beam, so photons in this spectral region will be filtered out. For this reason, the wavelength of the depletion beam should be red-shifted to the tail of the fluorophore emission. However, we should consider that higher is the fluorescence emission probability in a determinate spectral region and higher is the probability to have stimulated emission.

To overcome the diffraction limit, the stimulated emission process should saturate. Saturation allows widening the donut area, so that the spontaneous fluorescence emission can occur only in the very center of the excited volume. Thus, PSF becomes smaller with the increase of the depletion beam power. The final resolution, d, of the microscope is well described by the following relationship:

$$d = \frac{\lambda}{2NA\sqrt{1 + I/I_s}}$$

where I is the intensity of the STED beam, and the saturation intensity I_S is the intensity required by the STED beam to quench the spontaneous fluorescence emission by half. [59]

2.3 Multiphoton Fluorescence Microscopy

Multiphoton microscopy is a technique that, like confocal microscopy, allows us to have optical sectioning capability avoiding out of focus light.

For the one-photon excitation (1PE) process, a dye could absorb a single photon of a suitable wavelength reaching the excited state. Multiphoton excitation (MPE) use longer excitation wavelengths. MPE requires the simultaneous absorption of multiple photons so that the sum of their energies reaches the same values of the 1PE case. To realize the condition of simultaneous absorption, it is necessary a high photon density so that two or more photons can interact with the fluorophore in a time lower than 10^{-17} s. [17]

Considering two-photon excitation, the probability p_a that a fluorophore in the focus center absorbs a photon pair during a single pulse is: [65]

$$n_a = \frac{\delta \langle P \rangle^2}{\tau_p f_p} \left(\frac{NA^2}{2\hbar c \lambda} \right)^2$$

Where n_a is the number of absorbed photons per molecule, δ the two-photon cross-section, τ_p the laser pulse width, f_p the pulse repetition rate, N.A. the numerical aperture, ‹ P › the average incident power, $\hbar$ the Plank constant, *c* the speed of light in vacuum and λ the wavelength.

Thanks to the dependence of 2PE from the second-order of the excitation power, in a sharply focused excitation beam, the excitation probability outside the focal region falls off. Considering the homogeneous distribution of chromophores and a Gaussian beam, about 80% of the two-photon absorption at λ= 700 nm occurs in a volume of ellipsoidal shape with 0.3 µm of diameter and 1 µm of length that correspond to 0.1 femtoliters in volume (considering an objective lens with an *NA* = 1.4). This means that 2PE is confined to the focal volume providing excellent depth discrimination, resulting in a 3D resolution similar to a 1P confocal microscope. [46]

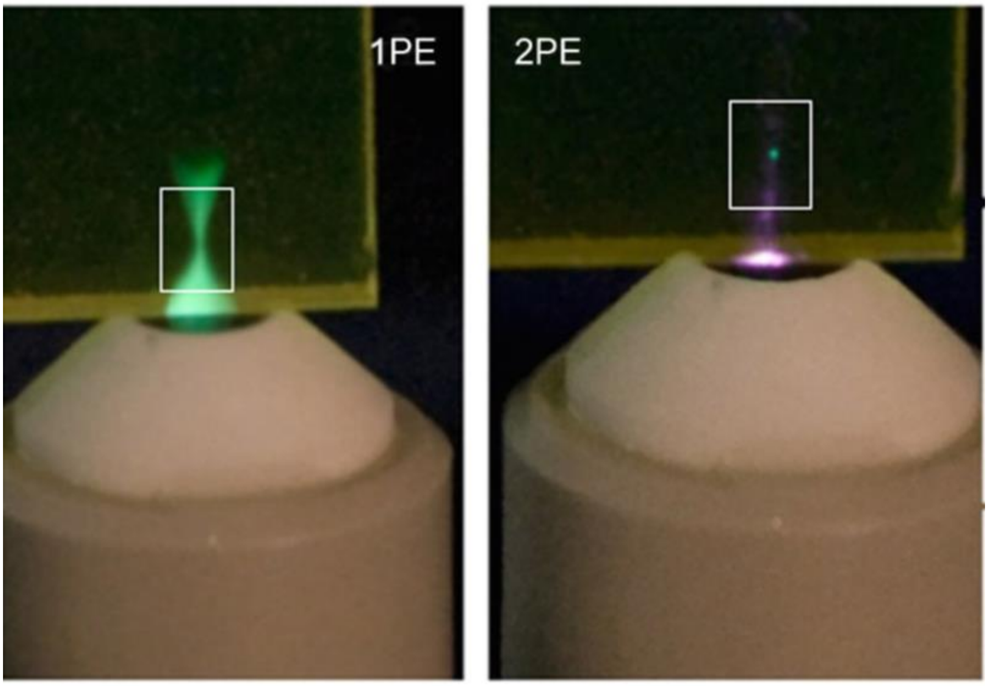

Fig. 2.5 1PE (left) and 2PE (right) [47]

Most fluorophores under continuous illumination photobleach rapidly, so localized excitation is an advantage. In 1PE, light is absorbed in all sample depths, so photobleaching occurs in all planes across the double cone. With 2PE we avoid out-of-focus excitation and then photobleaching and photodamage do not occur with the only exception of the imaging plane.[17]

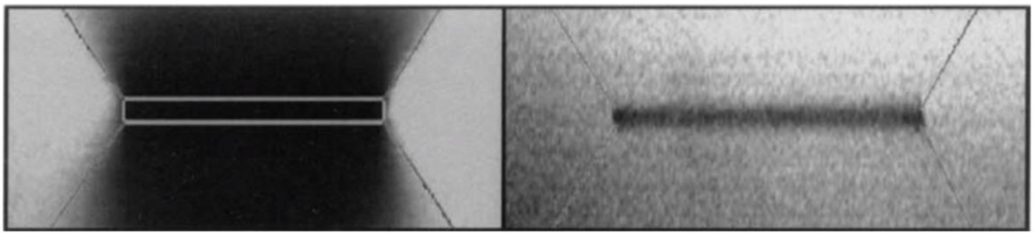

Fig. 2.6 Photobleaching of rhodamine with one- (left) and two-photon excitation (right). [17]

Since in two-photon microscopy we double the conventional excitation wavelength, the spectral region used will be approximately in the spectral window between 700- and 1000 nm. [66]

Longer wavelegths allow an improved penetration depth [67] and a reduced photodamage in living specimens. Moreover, the quadratic behaviour gives a resolution increase of approximately $\sqrt{2}$ compared to the diffraction-limited spot of excitation light. However, 2PE cannot be considered a genuine super-resolution because the longer wavelength causes an increase of diffraction spot size of a factor of 2 in comparison of single-photon excitation. [68]

2.4 Electrophysiology

2.4.1 Bioelectromagnetism

Bioelectromagnetism is a discipline that examines the electric, electromagnetic, and magnetic phenomena that arise in biological tissues. It is based on Maxwell's equations and the principle of reciprocity. Maxwell's equations connect time-varying electric and magnetic fields. While, the principle of reciprocity affirms that the source and the measurement sites may be swapped without a change in the detected signal. Bioelectric phenomena of the cell membrane are fundamental in living organisms. The cells use the membrane potential in several ways. The cellular potential is regulated through membrane ion channels, and, for example, allows communication among cells in the nervous system. Erwin Neher and Bert Sakmann won the Nobel prize in 1991 “for their discoveries concerning the function of single ion channels in cells” and for the invention of the patch-clamp technique. This technique allows measuring the electric current from ion channels, studying bioelectromagnetism and molecular biology, bringing crucial information for the development of new pharmaceuticals.[69]

2.4.2 Patch-clamp technique

The patch-clamp technique allows the electrophysiological measurements of currents through ion channels in the cell membrane. This technique allows us to record the activity of native channels in their natural environment and to investigate both the ion channel conductance and dynamic behavior. Thanks to this technique, new classes of ion channels were discovered, and their physiological role in cells was determined. With patch-clamp technique is possible to observe, in real-time, the changes in the activity of a single channel, including changes in conductance (the rate of ions going through the channel) and kinetic properties (the speed with which a channel opens and closes) in response to a pre-set stimulus. [70]

In this technique, a small heat-polished glass pipette is pressed against the cell membrane, forming an electrical seal. The resistance of the seal is important because it determines the level of the background noise of the current trace recorded during the measurement. Typically, a good resistance has a value ranging from 10 to 100 MΩ guaranteeing a low-level noise. [71]

There are five primary methods usable in patch-clamp experiments in Fig. 2.7 ;

1. Cell-attached recording
2. Whole-cell configuration
3. Outside-out configuration
4. Inside-out configuration
5. Perforated

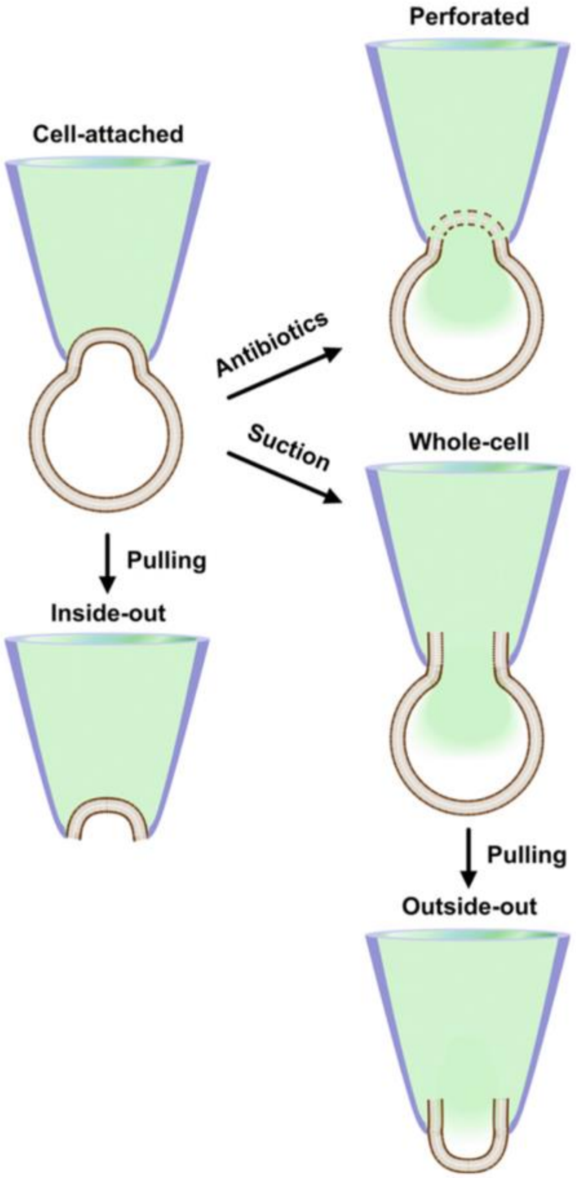

Fig. 2.7 Different methods of patch-clamp. [70]

All the procedures have, as a starting point, the cell-attached configuration that it is obtained as follows: using a microscope, after choosing an isolated cell, the patch pipette is moved towards that cell surface, while a low-voltage square pulse is applied to the pipette. When the pipette touches the membrane, there is an increase in resistance, and after a suction, a tight seal is formed [70]. This configuration allows recording a single-channel current from the sealed patch with the intact cell still attached. At this point, it is possible to pass to the others three measurement configurations. It is possible to break, after a suction, the membrane between the pipette solution and the cytoplasm, obtaining the whole-cell configuration. This allows measuring currents of all the cellular membrane. From this configuration, it is possible to obtain the outside-out patch, which is got excising the pipette slowly away. With this method, the outside of the cell membrane may be exposed to the bathing solution; therefore, it may be used to investigate the behavior of a single ion channel activated by the extracellular part of the receptor.

Another approach is to excise the seal from the cell by suddenly pulling the pipette away from the cell after reaching the cell-attached. This method is called the inside-out patch because the inside of the plasma membrane is exposed to the external salt solution. [72] The use of this approach is useful to investigate the cytoplasmic regulation of ion channels (see Fig 2.7). [69]

The last configuration is the perforated-patch configuration. It is similar to the whole-cell configuration and can be reached from the cell-attached configuration providing that the pipette contains a small amount of an antibiotic that allows the holing membrane. [70]

For the measurement of ion currents across the membrane, the patch-clamp technique uses a specific amplifier based on a current-to-voltage converter circuit, which transfers the pipette current into an equivalent output voltage. [73]

In practice, the amplifier measures the membrane voltage and compares it to a pre-set voltage (V) defined by the channel property. When a current is activated, there is a voltage change of a value V_i. To compensate for this change current of equivalent magnitude (but opposite direction) is injected through the pipette. [70]

$$I = \frac{(V - V_i)}{R}$$

This method is called Voltage Clamp.

Chapter 3: Materials and Method

3.1 Chemicals

Zinc-phthalocyanine (ZnPc) and Hypericin (HYP) stock solutions were prepared by dissolving molecules powder in dimethylsulfoxide (DMSO). Then, we determined, using the molar extinction coefficient and Lambert-Beer law, the concentration of molecules solved through a spectrophotometer.

3.2 Spinning disk

Spinning disk confocal microscopy utilizes multiple pinholes to project a series of parallel excitation light beams onto the specimen in a multiplexed pattern that is subsequently detected after fluorescence emission passing through the same pinholes. The main features of this technique are (i) the high-speed imaging of living cells, (ii) lower photobleaching, and (iii) low phototoxicity due to the use of multiple excitation beams that needs only low laser power. However, it is sufficient for exciting sample fluorescence. The microscope is composed by a confocal unit Nikon TiE inverted Microscope equipped with an Okolab incubation system, and four excitation lasers (405nm, 488nm, 561nm, 640nm). The system is equipped with a Yokogawa CSU-X1 spinning disk containing about 20,000 pinholes and a second spinning disk containing the same number of micro-lenses to focus the excitation laser light. The fluorescence light is collected by an Andor EMCCD camera Ixon 897. Therefore, we image the specimens sequentially exciting at 561 nm and 640 nm, and detecting in the spectral windows 575 - 625 nm and 670 - 740 nm, respectively.

3.3 STED nanoscopy

STimulated Emission Depletion nanoscopy is composed of a custom made setup equipped with a supercontinuum pulsed laser source (ALP-710-745-SC, Fianium LTD, Southampton, UK) [59]. The excitation wavelength was selected by means of an acousto-optic tunable filter (AOTF), while STED wavelength was predefined by the laser output. The laser has a repetition frequency of 20MHz and a pulse width of about 100 ps. In all the experiments, we used 566 nm of excitation and 715 nm of the STED beam. The donut shape of the STED beam was realized by a vortex phase plate (RPC Photonics inc., Rochester, NY, USA). The beams are scanned on the sample by galvanometric mirrors (Till-photonics, FEI Munich GmbH, Germany), focused by an HCX PL APO CS 100x 1.4NA oil (Leica Microsystems, Mannheim, Germany) objective and fluorescence is collected by an avalanche photodiode (SPCM-AQRH-13-FC, Excelitas Technologies, Vaudreuil-Dorion, Quebec, Canada) in the spectral window 670-640nm. The STED efficiency had been previously assessed by measuring the fluorescence depletion curve [74]

3.4 Uptake Analysis

To study PSs accumulation we have marked cells with "CellMask™ Deep Red Plasma Membrane Stain" (Thermofisher, USA), characterized by excitation and emission wavelengths (λ_{ex} = 649 nm, λ_{em} = 666 nm) that are longer than Hyp wavelengths (λ_{ex} = 550 nm, λ_{em} = 600 nm), allowing to separate the two signals. In this way, with CellMask™ is possible to identify the cell plasma membrane and compare the signal with that due to the Hyp accumulation (that is our PS object of study) on the same membrane Fig. 3.1. With the use of the software Fiji, we are able to extrapolate fluorescence profiles of 10-pixel thickness for each cell on each frame for both fluorescence channels (red for Hyp and deep red for CellMask™). Then, we analyzed these profiles Matlab custom-written code. Moreover CellMask™ fluorescence profile allows us to identify the external membrane position and to use it as the reference point. In this way, we are able to quantify the Hyp fluorescence emission intensity both on the plasma membrane and in the cytoplasm at each frame. From the average values of each profile, in turn averaged over all the cells analyzed, we were able to acquire the accumulation curves, over time, of the Hyp dye both on the membrane and in the cytoplasm. All measurements were taken at a temperature of 37 °C R.H. 95% and flow 0.6 l/min.

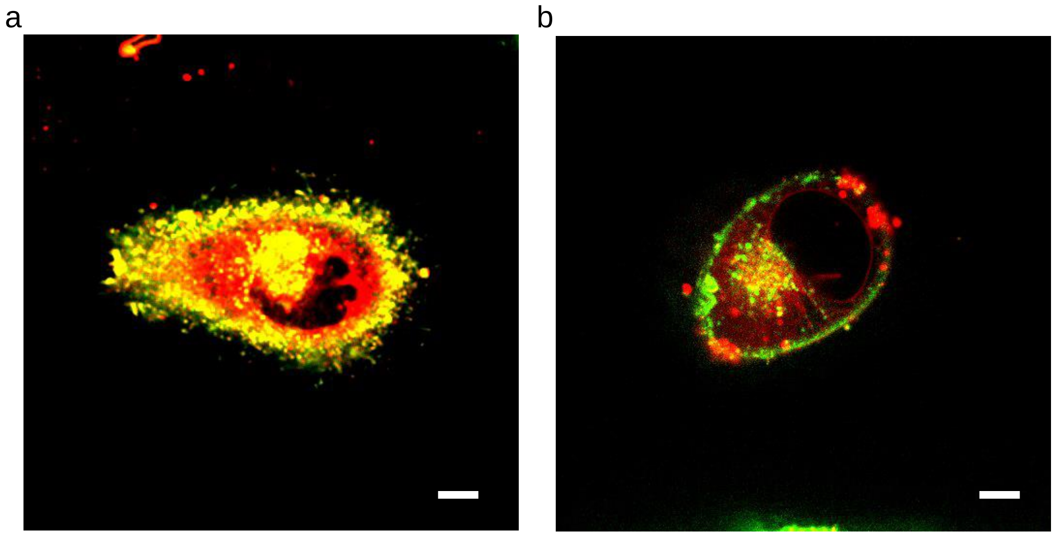

Fig. 3.1 two-color spinning-disk image of HeLa (a) and PC3 (b) cells. The cell mask is in green and hypericin in red. Scalebar (10 μm)

3.5 HeLa cells transfection and tumor spheroids preparation.

A stable cell-line expressing miRFP703 [75] fused to histone H2B obtained from the HeLa cell culture was selected with 0.7 mg/ml of antibiotic G418. The positive cells were sorted by BD FACSAria III (BD Biosciences San Jose, CA, USA) using a 633 nm laser line and 780/60 BP emission filter. This stable cell line was used to obtain multicellular tumor spheroids using suitable microplates equipped with non-adhesive surfaces to maintain cells in an un-attached state. The number of cells seeded was around $10^3 – 2x10^3$, and they were left in the incubator at 37 °C and 5% CO_2 for at least 48 h before imaging.

3.6 Live/Dead Assay

HeLa cells were grown in DMEM supplemented with 10% Fetal Bovine Serum and 1% pen/strep and glutamine. For the viability assay, HeLa cells were seeded on Nunc (ThermoFisher) at 60-80% confluence and were used after incubation at 37 °C and 5% CO_2 for 24 - 48 h.

LIVE/DEAD Viability/Cytotoxicity Kit (ThermoFisher) was performed to determine the viability of cells. Calcein-AM and ethidium bromide were diluted in the medium and added to cell cultures. By intracellular esterase activity, the calcein-AM is metabolically converted by live cells in a green fluorescent product, termed calcein. Instead, Ethidium bromide is readily absorbed by dead cells, labeling DNA with a deep red emission. Cells are incubated with these reagents for 10–15 min at 37 °C and imaged by confocal spinning disk at 37 °C and 5% CO_2.

3.7 Cerebellar granule cell culture

Cerebellar granule cells were obtained from 6 – 8 days old Sprague – Dawley rats as described by Robello et al [76]. In brief, they were planted with a density of 1.5 – 2.5 · 10^6 cells/well on coated glass treated with 20 µg/ml Poly – L – Lysine (Sigma-Aldrich, St. Louis, MO, USA).

The neurons were kept at 37 °C in a humidified 95% air/5% CO_2 atmosphere and grown in 90% basal medium Eagle, 10% fetal calf serum (Sigma-Aldrich, St. Louis, MO, USA), 25 mM KCl, 2 mM glutamine and 100 µg/ml gentamicin.

At 18–24 h from plating, 10 µM cytosine arabinoside (Sigma-Aldrich, St. Louis, MO, USA) was added to the culture medium to prevent glial cell growth; at 48 h the medium was refreshed and 10 µM cytosine arabinoside was renewed.

The cells were studied *in vitro* from the sixth to the tenth day.

3.8 Electrophysiology

The experiments were performed in the whole-cell patch-clamp configuration with an Axopatch 200 B (Axon Instruments, Burlingame, CA, USA).

The patch micropipettes (5–6 MΩ) were prepared using borosilicate glass capillaries (TW 150 – 3 World Precision Instruments Inc., Sarasota, FL, USA) and a P–30 puller (Sutter Instruments Co., Novato, CA, USA).

The currents were measured with a Labmaster D/A, A/D converter driven by pClamp 10 software (Axon Instruments, Burlingame, CA, USA) and analyzed with pClamp, SigmaPlot (SYSTAT Software, San Jose, CA, USA), MatLab (MathWorks, Natick, MA, USA) and Origin software (OriginLab, Northampton, Massachusetts, USA).

The standard external solution (pH 7.4) used for the maintenance of the cells in the recording bath contained (in mM): 135 NaCl, 5.4 KCl, 1.8 $CaCl_2$, 1 $MgCl_2$, 5 HEPES, 10 glucose; the micropipettes were filled with the internal solution contained (in mM): 142 KCl, 10 HEPES, 2 EGTA, 2 $MgCl_2$, 3 ATP and the pH was adjusted to 7.3 with Tris base.

The neurotransmitter GABA (Sigma-Aldrich, St. Louis, MO, USA) and the caged compound RuBi – GABA (Tocris Cookson Ltd, Bristol, UK) were diluted with an external solution at the needed concentration for experiments.

Where not specified, the final concentration of RuBi – GABA used was 10 µM.

3.9 One and two-photon imaging and uncaging

The uncaging procedure was performed using a three-channel of Leica TCS SP5 laser–scanning confocal microscope equipped with 458, 476, 488, 514, 543, and 633 nm excitation lines, through a plan-apochromatic oil immersion objective ×63/1.4. The images were acquired with the Leica "LAS AF" software package (Leica Microsystems, Germany).

Chameleon Coherent (Coherent Inc., Santa Clara, CA USA) femtosecond Ti:Sapphire laser was used to perform two-photon excitation.

The laser power was measured at the objective focal point by a power meter (PM100A, Thorlabs Inc., Newton, NJ, USA).

The images in transmitted light were acquired with a scan of 633 nm laser, and as a detector was used a photomultiplier.

For uncaging experiments, Frap Wizard Leica was used to set up the bleach points. An image before and after the uncaging was acquired to check that no cellular movements occured.

The currents measured after the photoexcitation of the caged compound directly return to the initial value because of the physiological separation of GABA from its site on the $GABA_A$ receptor, and it spreads out as a result of diffusion.

3.10 Carrier system: Photosensitizer protein binding

The hydrophobic effect mediates the interaction between PSs and proteins. In nature, proteins possess a hydrophobic pocket (i.e. an apolar environment) in which a cofactor is usually bound. Since PSs are hydrophobic molecules, typically when they are in the presence of a protein deprived of their cofactor they tend to occupy the protein pocket by binding to it forming a single complex. (Fig. 3.2)

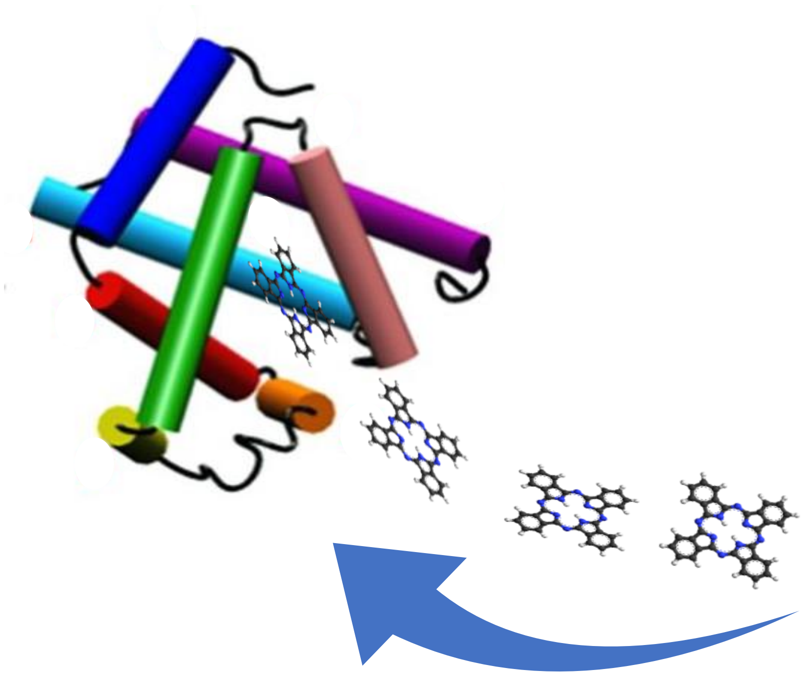

Fig. 3.2 Representation of binding dynamic.

The molecule that binds to the protein, thanks to the hydrophobic effect, recovers its monomeric state, while the rest of the molecules in aqueous solution tend to form aggregates such as dimers, trimers and oligomers of higher rank.

In the following paragraph we'll show how it is possible to bind a PS with a protein vector. Specifically, we will spectorscopilly study how the PS (Zinc-Phthalocyanine) ZnPC interacts and binds to the protein carrier ApoMyoglobin (ApoMb). [77]

3.10.1 ZnPc-ApoMb complex

ZnPc has a characteristic blue due to the intense absorption band peak in the red region at 670nm (Q-band). The more energetic transitions are lower intense, and they are found in the blue region of the spectrum around the 340 nm (Soret band). But when this PS is dissolved in aqueous solutions (i.e. PBS) it forms aggregates which result in a blue shift of the Q band. Furthermore the two peaks at 630nm and 670nm are due to the formation of the dimeric and monomeric species, respectively.[78]

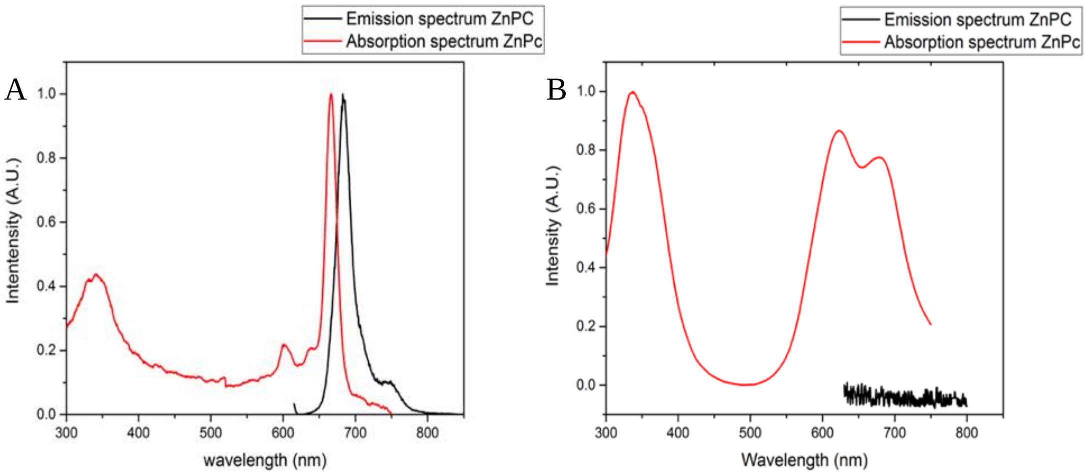

Fig. 3.3 Absorption spectrum (red) and emission spectrum (black) of ZnPc dissolved in DMSO (A) and in PBS (B)

The intense absorption peak at 670 nm and the high fluorescence signal in Fig. 3.3A indicates that ZnPc is soluble in an organic solvent (i.e. DMSO) where it has a monomeric conformation. Though, when the ZnPc is dissolved in PBS, the absorption spectrum changes, resulting in an increase of the absorption peak at 610 nm, in comparison to 670 nm peak (Fig. 3.3 B). This conversion is due to the formation of the aggregate state of ZnPc (dimer, trimer,[…]), which causes the loss of ROS production and fluorescence emission, fundamental characteristic useful in PDT.

To create nanostructures composed of PS-protein complexes, it is added a specific quantity of ZnPc dissolved in DMSO (10 μM) in a buffer solution in which is previously solved only ApoMb protein carrier.

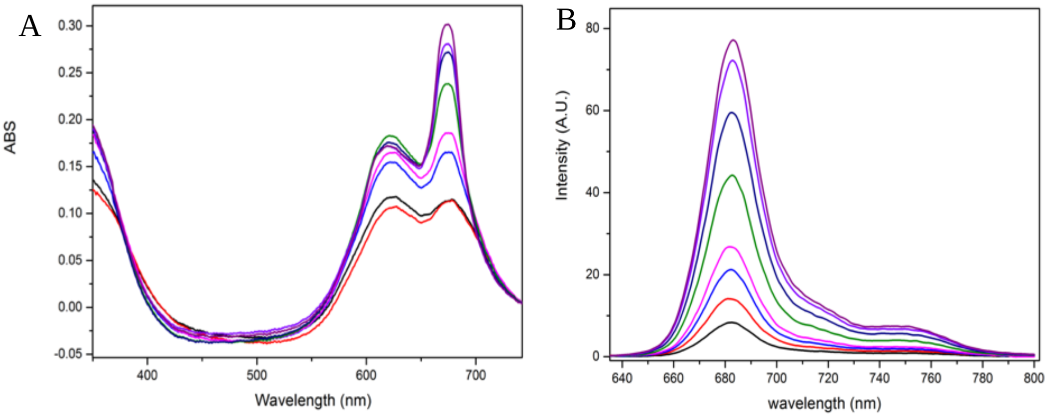

Fig. 3.4 Absorption spectrum with increasing protein concentration (From 0.6 to 14.9 μM)(A), emission spectrum with increasing protein concentration. (B)

Fig. 3.4 shows the measurements of the absorption and fluorescence emissions of various samples with different protein concentrations, in which a constant amount of ZnPc is added. Since the strong interaction among aggregates results in the impossibility of returning to the monomer state even if it is added the protein carrier in solution, it was not possible to perform measurements on a single sample, adding gradually greater quantities of protein to the initial solution composed of ZnPc dissolved in PBS. This means that the interaction between the ZnPc aggregates is greater than the hydrophobic interaction that would lead to the formation of the protein-PS complex. This does not happen for other photosensitizers such as hypericin and curcumin where, to form the complexes, it is possible to add the protein carrier after dissolving the photosensitizer in PBS.

From the absorption spectrum of ZnPc, by increasing the protein concentration, we observed an increase in the ratio between the two peaks at 610 nm and 670 nm (Fig. 3.4 A). This means that there is an increase in the population of ZnPc which is in the monomeric state since it tends to enter the protein pocket of the ApoMb.

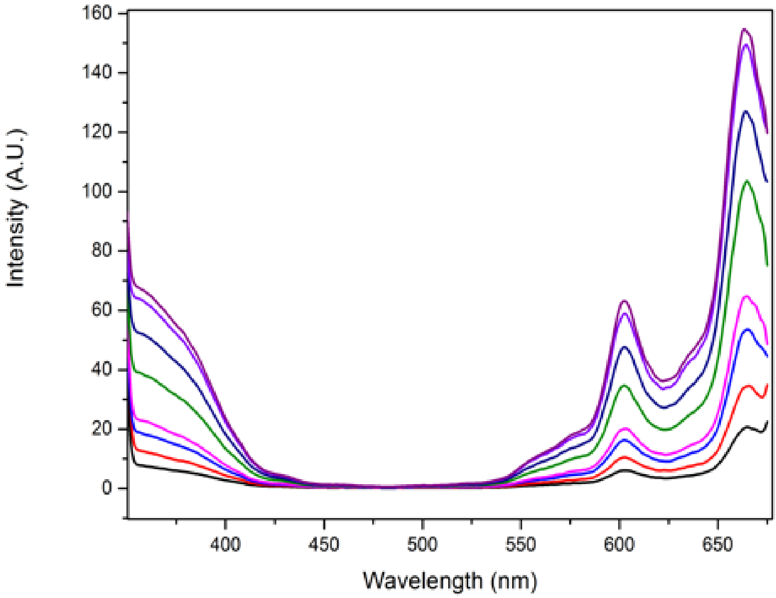

Fig. 3.5 Fluorescence excitation spectrum with increasing protein concentration (From 0.6 to 14.9 μM).

From the fluorescence excitation (Fig. 3.5) and emission (Fig 3.4 B) spectrum, it is possible to deduce the same things. In fact, it is recorded a growth of fluorescence emission at the increase of ApoMb concentration. Since aggregates are not fluorescent, the behavior suggests the there is an increased population of fluorescent ZnPc, which are in a monomeric state due to binding to the protein.

It is known, that for the common organic molecules the excitation spectrum coincides with the absorption spectrum. But in this case, we did not obtain the same trend because aggregates are not fluorescent, so they contribute to the absorption spectrum while not to the excitation spectrum.

The only contribute to the excitation spectrum is due to the absorption of the monomeric fluorescent ZnPc population that is bound to the protein.

Integrating all emission spectra at the variation of protein concertation and correcting for dilution factor and plotting the results in function of protein concentration, we obtain the binding curve (Fig. 3.6) from which we could infer the association constant of the complex ApoMb - ZnPc. $K_a = \frac{[R][x]}{[Rx]} = (9{,}0 \pm 0{,}6) \times 10^{4}$ M^{-1}.

Where [RX] is the complex concentration at equilibrium, while [R] and [X] represent respectively the concentrations of protein and free photosensitizers at equilibrium. Tipically mioglobin has a single binding site in which is present his cofactor called Heme.

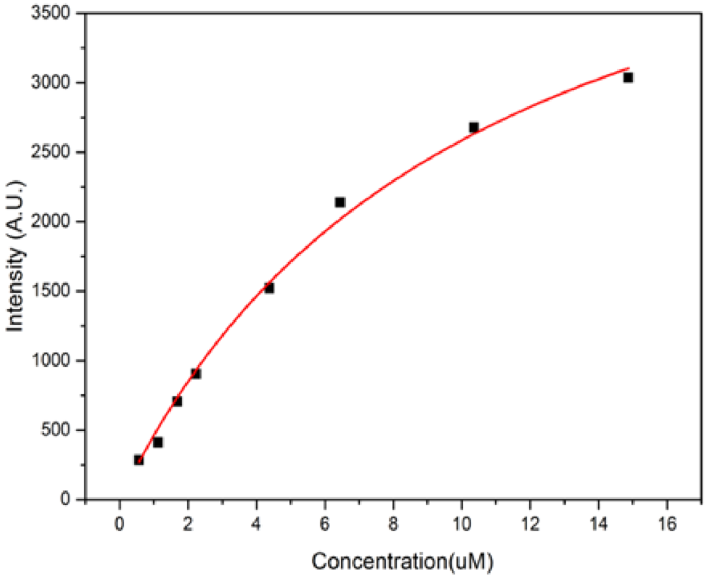

Fig. 3.6 Binding curve

Chapter 4: Results and discussion

4.1 RuBi-GABA Uncaging on cerebellar granule cells

Photoactivatable cage compounds remain the primary tools to study membrane proteins, such as GABA receptors, with a high spatiotemporal resolution.

In this work, the photoactivation of caged molecules, in a controlled volume, is used for releasing a small amount of GABA neurotransmitters, in a well confined way.

So, it is possible to choose a cellular region as an object of study, uncage GABA neurotransmitters in its proximity, and collect cellular response through electrophysiology measurements.

As can be imagined, some physical parameters such as the quantity, geometry, and the modality of GABA release can change, causing, in turn, a change in the neural response.

The main goal of this part of the thesis work concerns the investigation of all the photophysical parameters that change the GABA uncaging, performing a two-photon uncaging of RuBi-GABA. This allows to understand the mechanism of GABA release and to obtain the maximum spatio-temporal control. In detail, this study wants to provide the capability to remove the dependence from these photophysical parameters for being sure that variations in patch-clamp signals were given only from the change of biological parameters.

First of all, we have observed differences induced by the variation of laser power, exposure time, XYZ distance from the cell, and different holding potential. All this measurement has been achieved using both one and two-photon excitation. Moreover, we determined the advantages and disadvantages given by non-linear photoactivation.

By comparing the values of the current, acquired with the patch-clamp technique, changing from time to time the different parameters mentioned above, it is possible to obtain the best physical conditions to be set during the uncaging experiments. We observed that the current value increases in several cases, while in others, the signal shape changes.

Moreover, we performed these measurements both on the same cell and doing statistics on more cells, minimizing, in this way errors in order to remove the biological sample influence.

4.1.1 Antagonist test

The first test performed was the Antagonist test. It is fundamental to confirm the activation of $GABA_A$ receptors by the uncaged RuBi–GABA molecules.

As a competitive antagonist molecule we used Bicuculline that it is a $GABA_A$ receptor inhibitor.

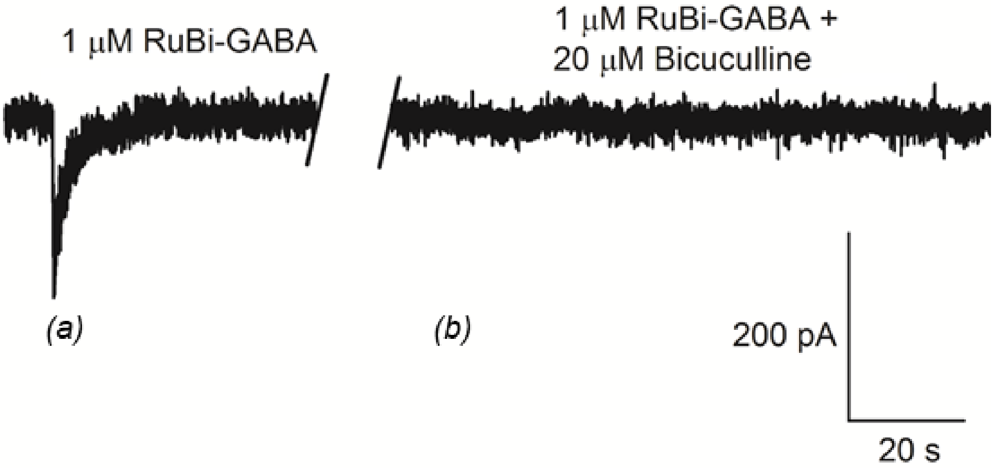

Fig. 4.1: Measurement of a current evoked by the photoactivation (458 nm, 100 ms, 6.7 µW) of 1 µM RuBi – GABA (a); on the same cell, in the presence of 20 µM competitive antagonist bicuculline, uncaged 1 µM RuBi – GABA does not activate $GABA_A$ receptors (b).

Fig. 4.1 (a) shows the characteristic ion current signal induced from the chloride ions passages, because of the activation of the $GABA_A$ receptor. The receptor activation is due to the 1PE uncaging of RuBi–GABA in the proximity of the cerebellar granules.

When granules are treated with 20 µM of bicuculline, it tends to bind to the GABA site of the channel localized between the α and β subunits of the $GABA_A$ receptor.

After the binding, GABA$_A$ is not able to open the channel and no current signal is present. (Fig 4.1b).

This measurement confirms that the RuBi–GABA photoactivation effectively generates a GABAA receptors response.

4.1.2 Effect of 1PE and 2PE power changes

The number of photo-released molecules after photoactivation depends on three parameters: the excitation volume size, the concentration of caged molecules in this volume, and the laser power.

As can be imagined, when the laser power is low, only a fraction of caged molecules will be uncaged. Increasing the laser power, the amount of uncaged RuBi–GABA increases until saturation occurs, i.e. when all the molecules in the excitation volume will be uncaged. At this point, the quantification of uncaged molecules depends only on their concentration.

As mentioned before, another significant value is the excitation volume. It is possible to control this value by choosing a linear or nonlinear photoactivation. Using 1PE (458 nm), RuBi–GABA is uncaged along the all optical path crossing the sample, proportionally to the amount of light absorbed in each plane. Using 2PE (750 nm), the uncaging occurs in the focal point where the photon density is the highest.

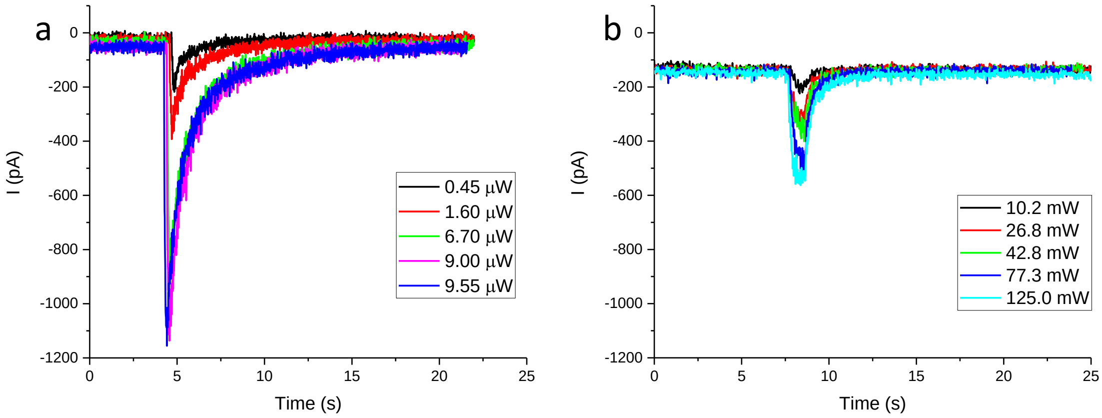

Fig. 4.2: Examples of chloride current peaks evoked by 10 μM uncaged RuBi – GABA at different laser powers during 1PE (458 nm, 100 ms) (a) and 2PE (750

nm, 100 ms) (b) on the same cell. The data are normalized at current value evoked by uncaging of 4.9 µW for 1PE and 77.3 mW for 2PE.

Fig. 4.2a and 4.2b show currents measured on the same cell after one and two-photon uncaging, respectively.

As already said, increasing the laser power, the uncaged GABA molecules increase causing an increase of activated receptors that, in turn, cause a higher current peak (fig 4.2 A and B).

From the comparison of Fig. 4.2 A and 4.2 B, we obtain another information regarding the excitation volume. The maximum current peak, after 2PE uncaging, results lower, in comparison with 1PE. This is due to the smaller volume of 2PE than 1PE case. In fact these two excitation volumes have different geometries: 1PE might be approximate as a large double cone centered in the focal point while 2PE geometry is an ellipsoid around the focal point. [79]

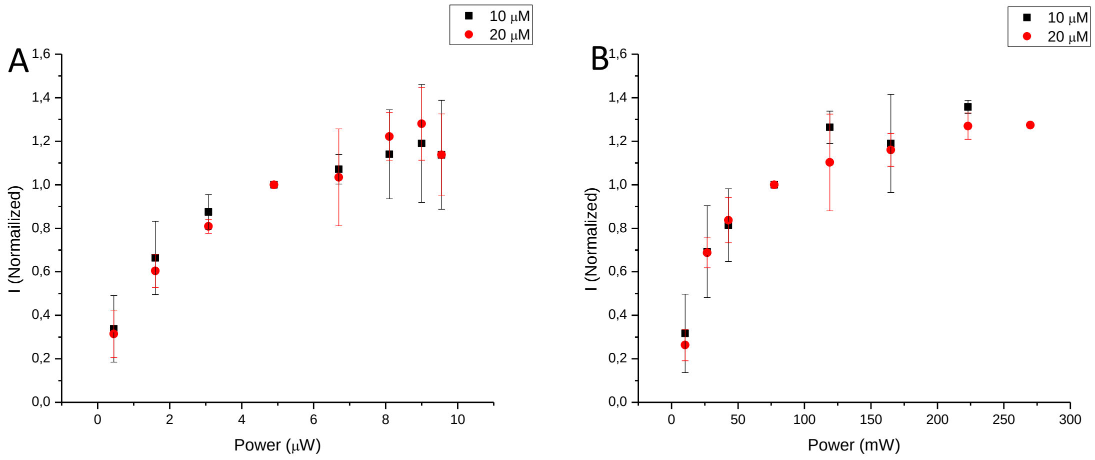

Fig. 4.3: Normalized values of current evoked by 10 µM (black squares) and 20 µM (red dots) uncaged RuBi – GABA at different laser powers during 1PE (458 nm, 100 ms) (A) and 2PE (750 nm, 100 ms) (B). The data are normalized at current value evoked by uncaging of 4.9 µW for 1PE and 77.3 mW for 2PE.

Fig. 4.3 A and 4.3 B describe the normalized mean values (at least 3 cells) of the peak current, in the function of the laser power, at two different concentrations of RuBi–GABA (10 and 20 µM). At lower powers, few molecules are released. Raising the laser power gradually, uncaged GABA increases until all the molecules are photolyzed in the excitation volume, reaching saturation.

The two different concentration is used for being sure that the saturation comes from the uncaging of all the molecules in the excitation volume and not to the saturation of the receptors on the plasmatic membrane of the neurons. Both curves have the same trend confirming that there is not a receptor’s saturation. The curve plateau is only due to the release of all molecules in the excitation volume.

4.1.3 Exposure time

Exposure time is a parameter that can influence the administration of GABA molecules leading to the change in the current signal shape. Moreover, for 1PE, the exposure time can also influence the excitation volume size.

Our first assumption is that caged molecules in the solution spread out. Being exposure time longer than the diffusion time, the molecules in the excitation volume will be uncaged while spreading out. At the same time, other caged molecules will enter in the excitation volume and will be photoactivated.

Becouse of this mechanism, with long exposure time, a cloud of mixed caged and uncaged molecules are formed within and outside the excitation volume.

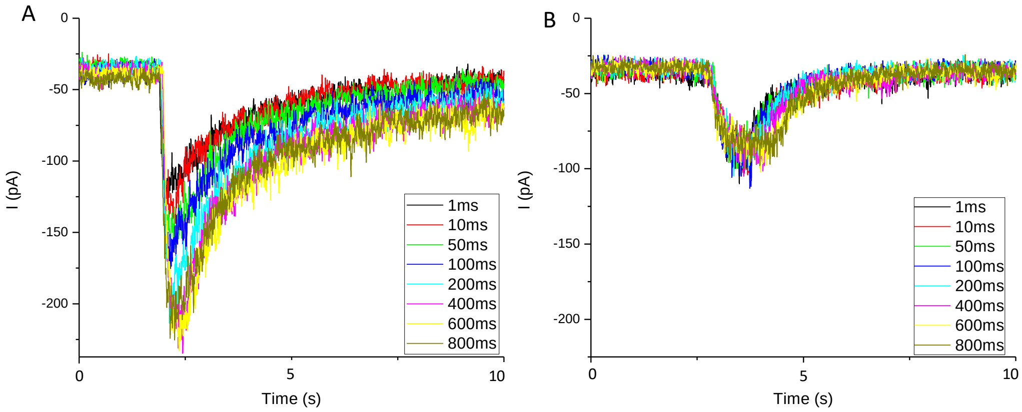

Fig. 4.4: Examples of chloride current peaks evoked by 10 µM uncaged RuBi – GABA at different exposure times during 1PE (458 nm, 9.36 µW) (A) and 2PE (750 nm, 125 mW) (B) on the same cell.

Experiments were performed (at least on 4 cells) changing the exposure times (1, 10, 50, 100, 200, 400, 600, 800 ms) for analyzing how may vary the electrophysiological measurements. (fig. 4.4A and 4.4B).

From these measurements is possible to extrapolate the average peak intensity and plot them in functions of the exposure time:

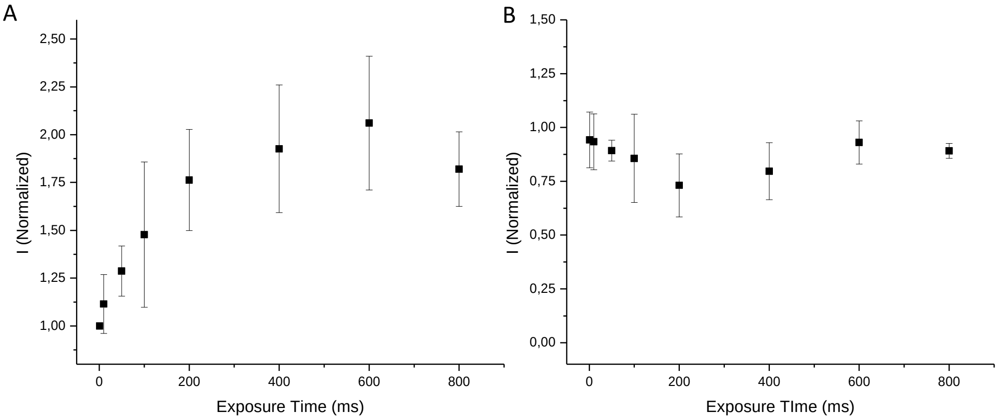

Fig. 4.5: normalized values of current evoked by 10 µM uncaged RuBi – GABA at different exposure times during 1PE (458 nm, 9.36 µW) (A) and 2PE (750 nm, 125 mW) (B), the data are normalized at the current value of the lowest exposure time (1 ms).

Another parameter is the decay value of the peak obtained, interpolating the only the decay function with a single exponential (considering only the fastest decay of the curve fig 4.4 bis):

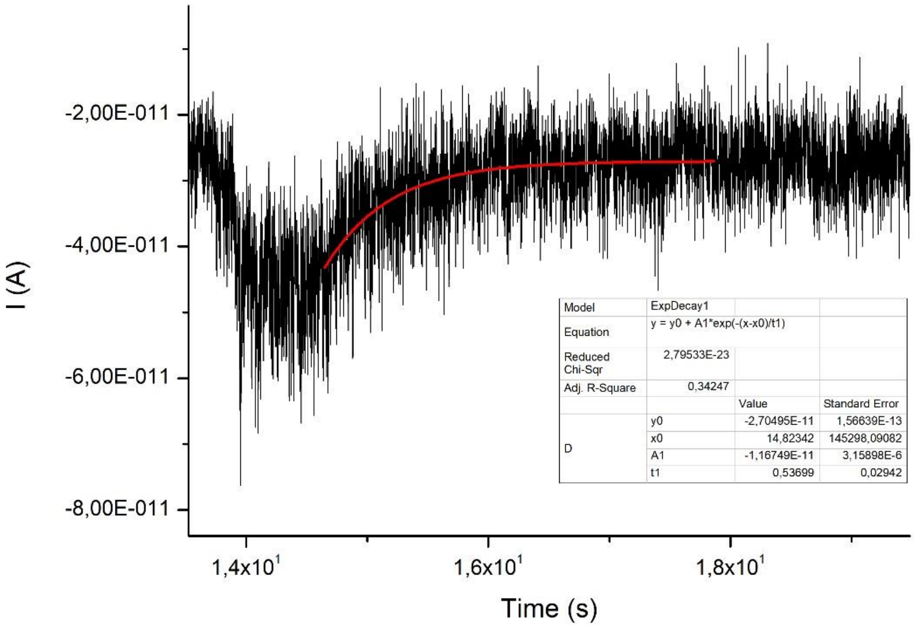

Model	ExpDecay1		
Equation	y = y0 + A1*exp(-(x-x0)/t1)		
Reduced Chi-Sqr	2,79533E-23		
Adj. R-Square	0,34247		
		Value	Standard Error
D	y0	-2,70495E-11	1,56639E-13
	x0	14,82342	145298,09082
	A1	-1,16749E-11	3,15898E-6
	t1	0,53699	0,02942

Fig. 4.4 bis. Example of exponential decay fitting of chloride current peaks evoked by 10 µM uncaged RuBi – GABA with 2Ph Excitation

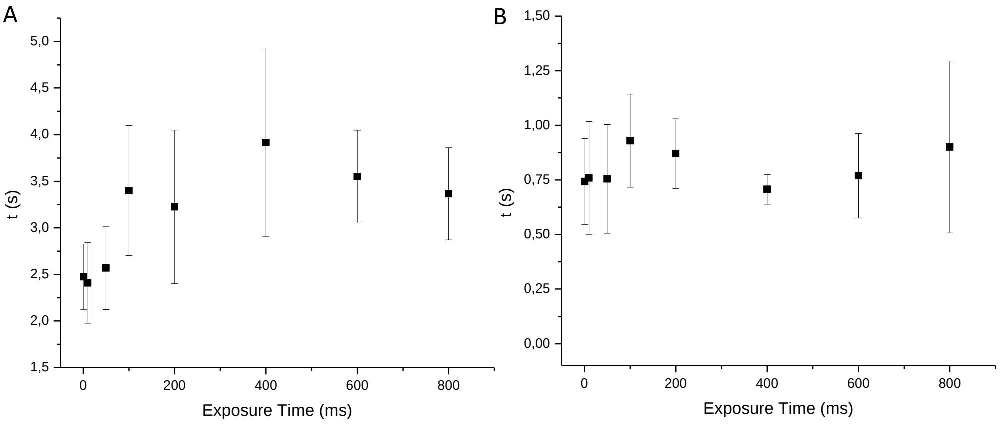

Fig. 4.6: time of decay in function of the exposure time (τ) during 1PE (458 nm, 9.36 µW) (A) and 2PE (750 nm, 125 mW) (B);

Finally, we can plot the full width at half maximum (FWHM) that is characteristic of the GABA administering:

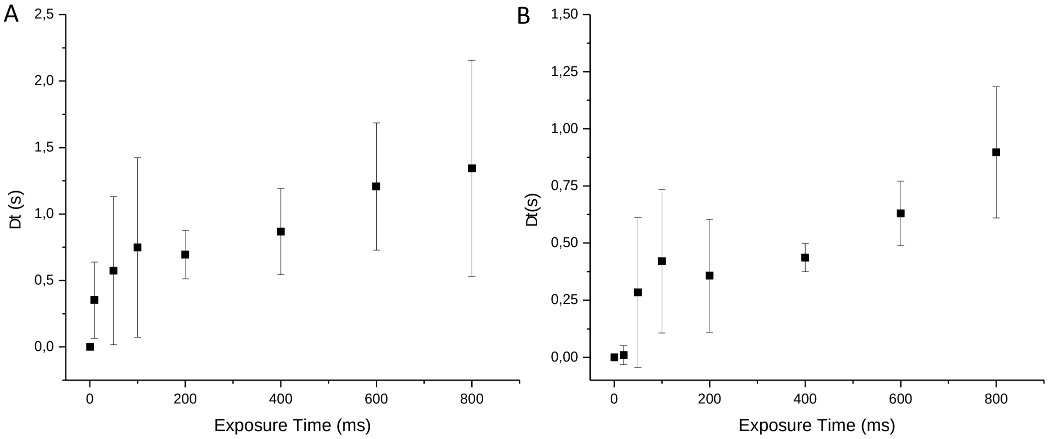

Fig. 4.7: the difference between FWHM and FWHM at 1 ms in the function of the exposure time during 1PE (458 nm, 9.36 µW) (A) and 2PE (750 nm, 125 mW) (B).

Using 1PE and protracting the exposure time, the intensity of the current peak (fig. 4.4A and 4.5A) and the time of decay (fig. 4.6A) increase until a plateau value. Considering the full width at half maximum (FWHM) of the signal it results in a linear trend when the exposure time increases (fig. 4.7A).

With 2PE, the behavior changes: the peak of current and the time decay does not vary (fig. 4.4B, 4.5B, and 4.6B), but the FWHM (Fig.7 B) linearly rises with the exposure time.

This analysis explains how the behavior of neuronal response changes using 1PE or 2PE. The increase of the exposure time during 1PE raises the dimension of the uncaging volume causing an increase of the current intensity (fig. 4.5A).

This is correlated to the probability of photoactivation in the far planes from the focal point. In these planes the photon density is smal, thus the probability of uncaging molecules is low.

On the other hand, rising the exposure time, the probability increases, and it produces a raise of the excitation volume.

This volume increment increases the number of uncaged molecules leading to a raise in the number of the receptors involved in the signal and consequently extends the decay time of the signal. (fig. 4.6A).

This behavior does not happen for 2PE (Fig. 4.5 B), where the excitation probability peculiarly depends on laser power.

For both 1PE and 2PE when the power increases the full width at half maximum broadens too. However, in the first case is due to the mix of two effects: decay time (Fig. 4.6 A) and neurotransmitter administration become longer because we increase the exposure time. (fig. 4.7A).

When 2PE is used, the behavior changes: in fact, as shown in fig. 4.5B and 4.6B, the current intensity and decay time remain constant because the excitation volume of the two-photon does not significantly vary by varying the exposure time. Therefore, the population of receptors involved in the signal is constant.

Only the full width at half maximum (fig. 4.7B) linearly increases with the exposure time because the neurotransmitter is administered for a longer time. This is confirmed by the fact that for a variation of the exposure time there is the same variation of the full width at half maximum.

4.1.4 X, Y, Z distance from the target

Changing the distance between the uncaging point and the cell, the amount of uncaged GABA that will binds $GABA_A$ receptors on the plasma membrane will vary. This is due to the isotropic diffusion of photolyzed molecules from the uncaging point that is defined as the source point.

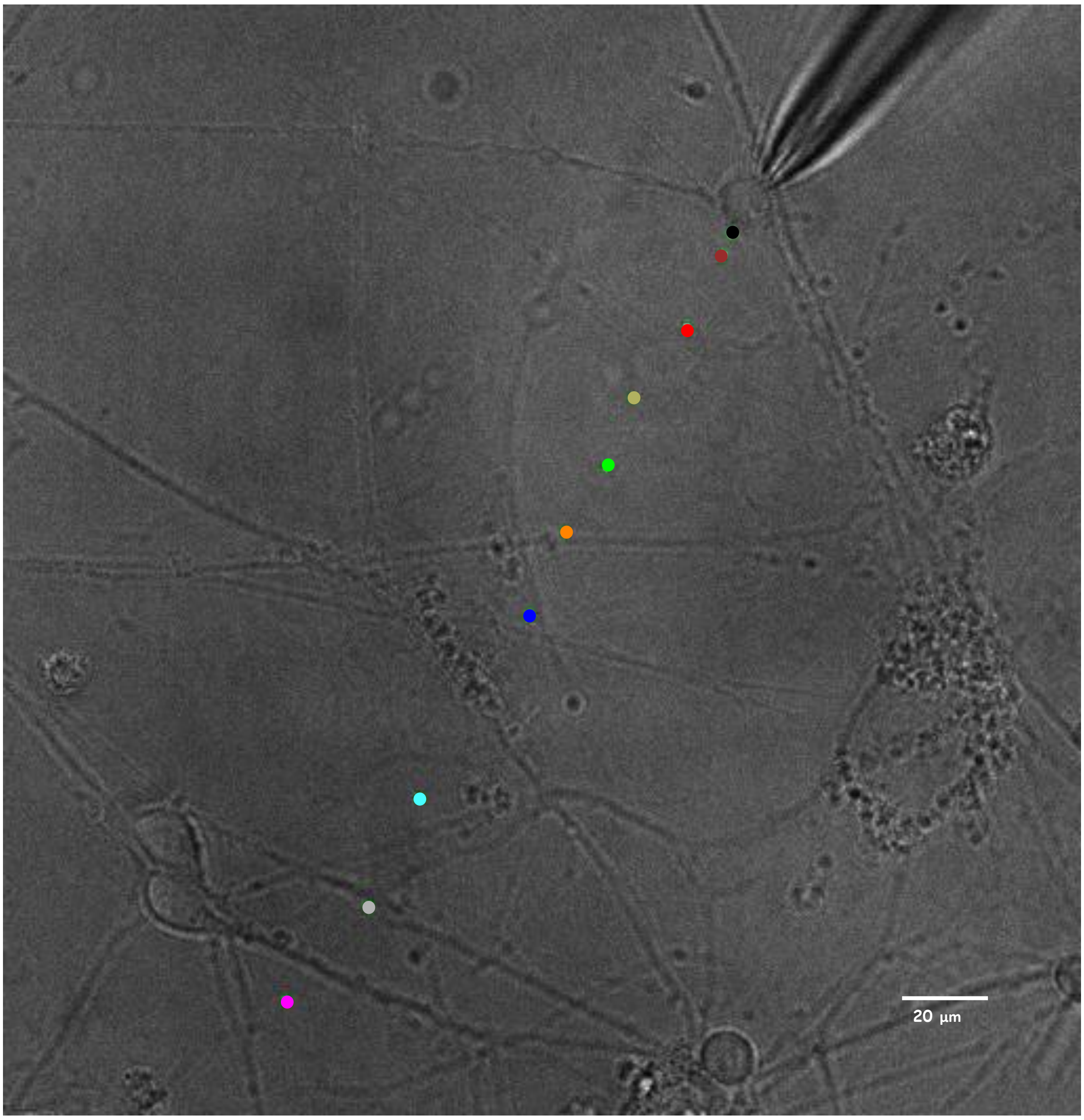

Fig. 4.8: Example of uncaging point variations on X–Y axis

Changing the uncaging distance on the X–Y axes (fig. 4.8), the measured currents, using both 1PE and 2PE, decrease as shown in fig 4.9 A and 4.9 B.

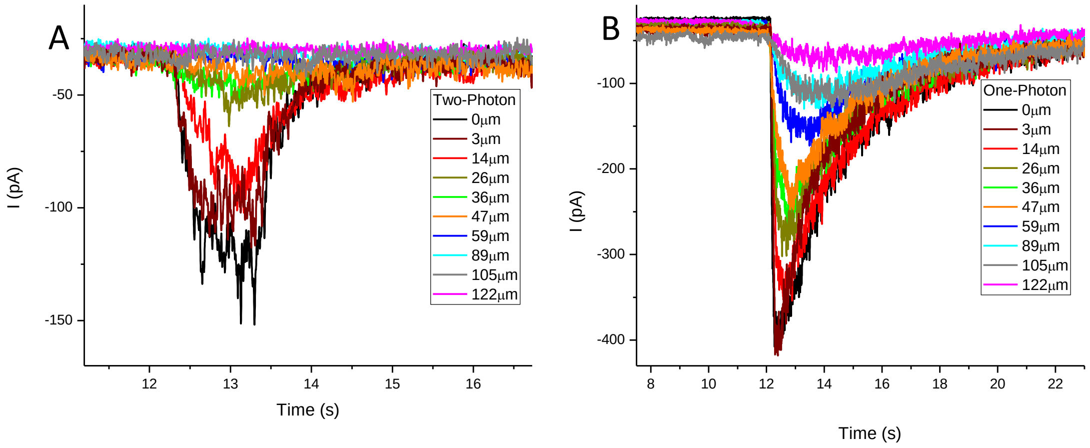

Fig. 4.9: Currents related to the example of fig. 4.8 during 2PE (750 nm, 100 ms, 77.3 mW) (A) and 1PE (458 nm, 100 ms, 9.36 µW) (B).

Moreover, from the graphs in Fig. 4.9 A-B is possible to observe not only a change of current intensity but also a change of the rising current in the function of distance that is due to diffusion.

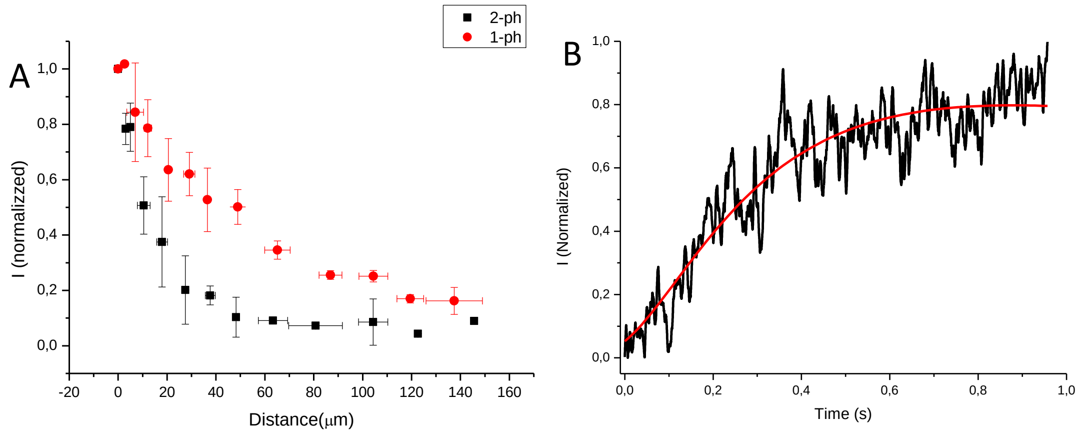

Fig. 4.10: Peak value for 1PE (458 nm, 100 ms, 9.36 µW) and 2PE (750 nm, 100 ms, 77.3 mW)to vary of XY distance; normalized data (at least 4 cells) at the current value nearest of the cell (A). The rising peak in function time during 1PE (458 nm, 9.36 µW) at 50 µm uncaging distance interpolated with Eq. 4.1 .(B)

As shows in the following equation, the diffusion of the molecules can be approximated as diffusion of an instantaneous point source:

$$C(x,t) = \frac{A}{\sqrt{4\pi D \cdot t}} e^{\left(-\frac{x^2}{4Dt}\right)} \quad (4.1)$$

with C as molecule concentration, D as diffusion coefficient, x as the distance from the point source, t as the time and A as an arbitrary constant [80]

Increasing the uncaging distance increases the rise time. Since we uncage away from the cell, not all uncaged molecules will reach the receptors at the same time(fig. 4.9 A, B and 4.10 B).

The theoretical value of the GABA diffusion coefficient evaluated for GABA molecules with the Stokes-Einstein equation, using water as medium and a concentration of 10 μM, is $7 \cdot 10^{-10}$ $m^2 \cdot s^{-1}$.

The value obtained from the measurements performed in the experiments, as shown in fig. 4.10 B, is $(6 \pm 3) \cdot 10^{-10}$ $m^2 \cdot s^{-1}$ which results in good agreement with the theoretical value. Therefore, the variations of the current peak are due to diffusion phenomena. The diffusion coefficient was calculated at different distances between 20 to 90μm.

In Fig. 4.10 are shown the current peak values, as a function of the distance from the cellular membrane both for experiments performed with 1PE (red dots) and 2PE (black squares). Varying the uncaging point in X and Y (fig. 4.8) and moving from the target, the number of molecules that reach the receptor is gradually lesser due to the isotropic diffusion of the compound in solution. When uncaging is produced using 2PE, the current peaks show a faster decrease, compared to 1PE, as the distance on the X-Y plane increases. This confirms that two-photon microscopy results more sensitive than one–photon.

Whereas, when we uncage in different positions on Z-axis (Fig. 4.11), current peaks measured for 2PE and 1PE have different trends.

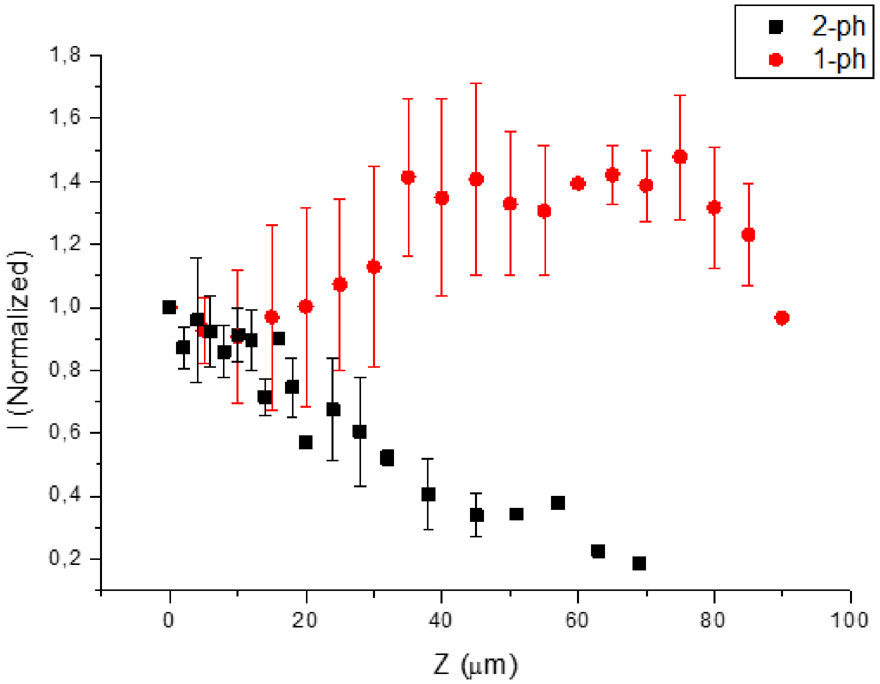

Fig. 4.11: Normalized data (at least 3 cells) current value at different Z-Distance: red dots for 1PE (458 nm, 100 ms, 9.36 µW) (red dots) and black squares for 2PE (750 nm, 100 ms, 77.3 mW).

In the first 10 µm from the coverslip surface, the current peak for 2PE remains constant. This is due to the Z-dimension of the cerebellar granule that is of the order of 10 µm. Going to further distance, the current value decreases. (Black dots of fig. 4.11) because the photolyzed molecules, that can arrive at the receptors, are lesser because of the diffusion. The same result was also obtained when we changed the distance in X and Y.

This does not happen for 1PE where the current increase in the first points until achieves a plateau (red dots of fig. 4.11).

The increase of the current is due to the moving, in the solution, of the lower excitation cone that, in the beginning, was under the glass slice. After that, the current trace reaches a plateau because the gain of the uncaged molecules of the inferior excitation cone is balanced from the symmetric part of the superior cone.

4.1.5 Curve current–voltage

The experiment conducted, consists of an I - V currents in different conditions. Changing different holding potentials and collecting the current signals is possible to investigate if and how endogenous GABA and uncaged RuBi–GABA have different effects on current traces. The measurements made with 10 µM GABA show an ohmic trend (4.12) [81].

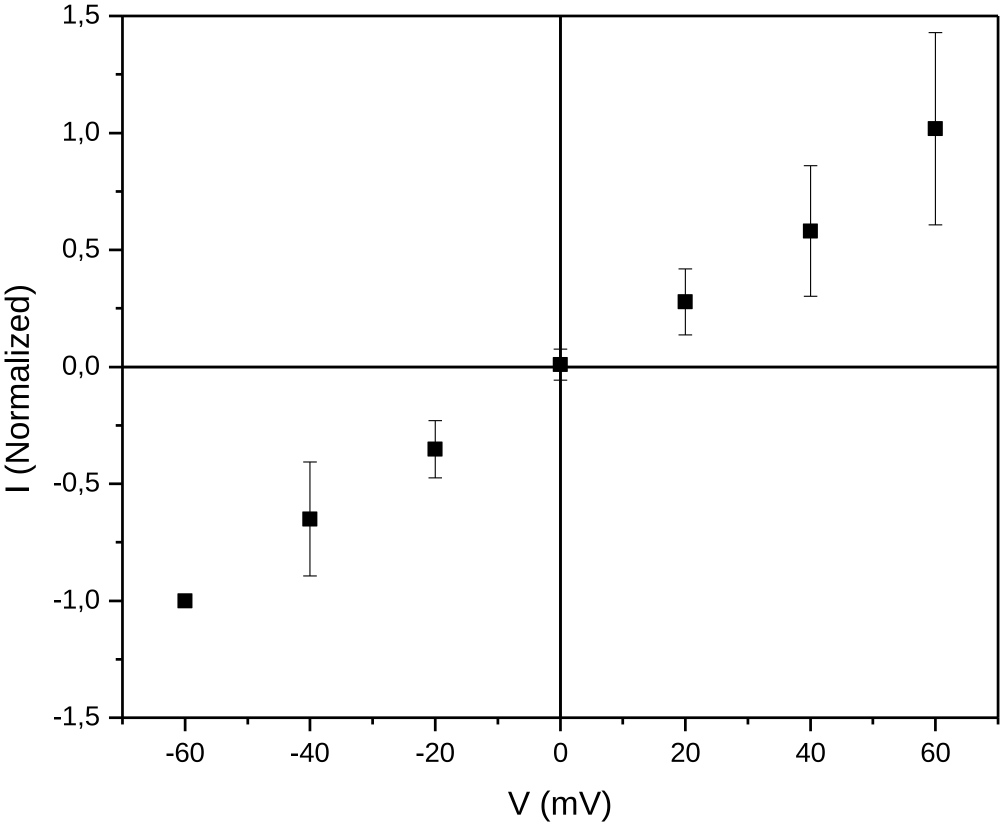

*Fig. 4.12**:** Current – potentials curve obtained after the administration of 10 µM GABA. The data (at least 4 cells) are normalized at the current values of –60 mV. The potential range goes from –60 mV to +60 mV with a step of 20 mV.*

Other experiments (on 4 cells) were carried out with photolyzed 10 µM RuBi–GABA (1PE, 458 nm, 9 µW, 100 ms) (Fig.4.13). The photoactivation point was set near the cell target, and the currents were recorded applying a voltage bias spanning from –60 mV to +60 mV with steps of 20 mV.

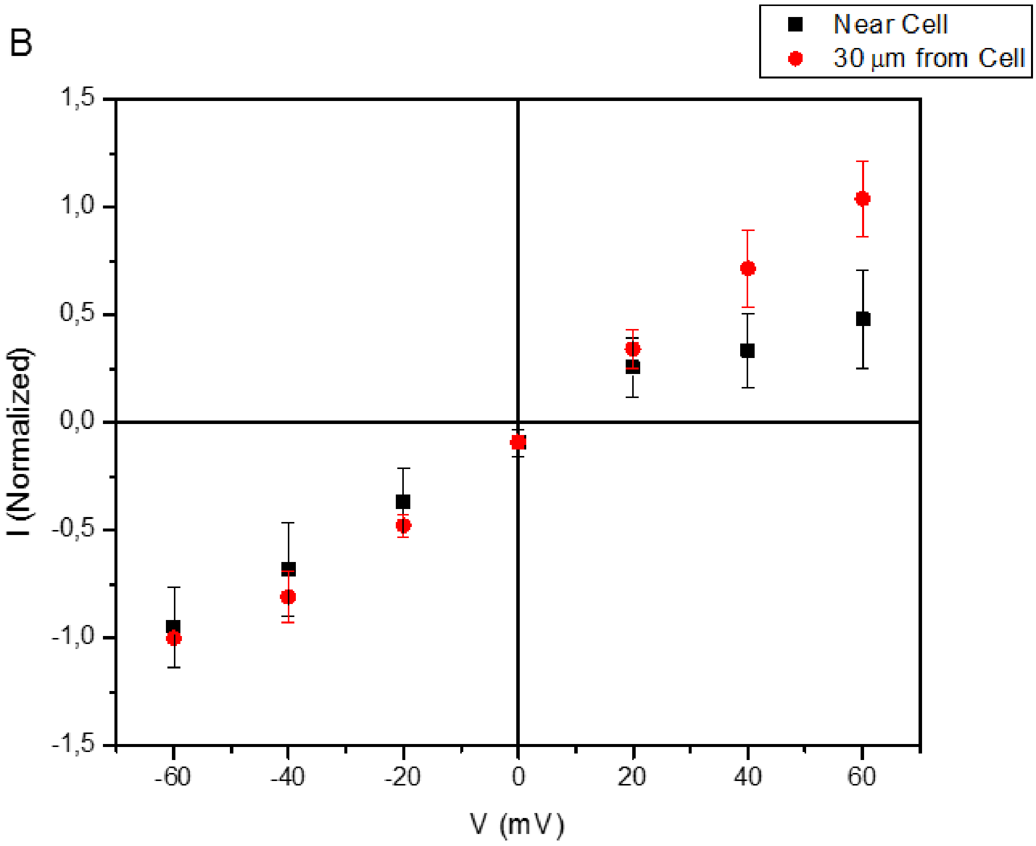

*Fig. 4.13**:** Current – potentials curve obtained after uncaging of 10 µM RuBi – GABA with 1PE (458 nm, 9 µW) and 100 ms of exposure time. The data are normalized at the current values of –60 mV. The potential range goes from –60 mV to +60 mV with a step of 20 mV. The experiments (at least 4 cells) were performed near (black squares) and at 30 µm from the cell (red dots).*

The data (black squares) are reported in Fig. 4.13: at positive bias, the current peak values deviate from the ohmic behavior; the current module is lower than the negative one.

Then, RuBi–GABA was uncaged 30 µm far away from the plasma membrane, and this resulted in currents with the same ohmic behavior both for negative and positive bias, similar to experiments performed with endogenous GABA (red dots fig. 4.13). The current response in function of the potentials in cerebellar granule cells usually shows an ohmic trend (fig. 4.12), this also occurs at a great distance, but not when the uncaging is near the cell (fig. 4.13).

It is possible to suppose that this behavior derives from a local change of the potential due to the uncaging: the caged group, in fact, shows a positive charge in aqueous solution, which might lead to electrostatic interaction with chloride ions [82].

This hypothetic binding would entail a depletion of the chloride concentration in the external solution near the cell.

Therefore, it would bring to a decrease of currents at positive potentials, that is when the chloride moves from the external solution into the cell.

4.2 Photosensitizer action on tumor cells

Intracellular distribution of PSs may play a key role in the different degrees of phototoxicity of Hyp and Hyp-apoMb. Fluorescence microscopy is one of the main methods to investigate the localization and diffusion of molecules or proteins in a living system [83], and it is useful to understand PSs uptake by cultured cells.

In this section, we studied different PSs that have several properties of interest for photodynamic therapy (PDT). Moreover, we will see how these PSs combined with a suitable protein carrier increase their efficacy.

In particular, the use of protein carrier systems can increase the rate of accumulation of hypericin PS or can increase the ZnPc compatibility and bioavailability.

Furthermore, we will also see that by using curcumin it will be possible to change the areas of intracellular accumulation and photostability, and finally, it will be shown how the use of Zinc Myoglobin VIP as a protein carrier allows you to give selectivity to PDT which is one of the fundamental requirements to damage only cancer cells.

All PSs studies were performed, taking advantage of fluorescence emission of these dyes.

4.2.1 Hypericin

Hypericin is well-known for its different photodynamic effects. These effects were discovered when grazing animals ingested St. John's wort (i.e Hypericum Plant) and showed effects such as severe skin irritation, high temperatures bodily, and in extreme cases, even death. This phenomenon took the name of hypericism because it causes severe and robust events of photosensitivity due to ingestion hypericin contained in the Hypericum. Since hypericism is an oxygen-dependent condition, its photodynamic action was soon recognized.

Like many other photosensitizers, Hyp is insoluble in water and forms aggregates, which dramatically influence the photo-physics of the compound, resulting in the quenching of the excited states that lead to triplet state formation, consequently impairing the photosensitizing properties.

Binding of Hyp to proteins increases its solubility in physiological media [84,85], and thanks to their high biocompatibility, proteins appear to be a promising delivery vehicle ensuring good bioavailability of the drug and preservation of its photodynamic action against target cells [86,87]. In particular, Hyp binds with moderate affinity (K_d = 4.2±0.8 μM) to apomyoglobin (apoMb) forming a self-assembled, non-covalent complex, endowed with good fluorescence quantum yield (Φ_F = 0.14±0.02) and efficient singlet oxygen photosensitization (Φ_Δ = 0.14±0.03) [74].

For comparison, the fluorescence and singlet oxygen quantum yields of Hyp in organic solvents, such as DMSO, are Φ_F = 0.35±0.02 and Φ_Δ = 0.28±0.05, respectively [74].

Hyp-apoMb presents a higher efficacy of Hyp and results in more phototoxic cell viability tests [88]. For understanding which mechanism produces these differences, we performed some microscopic tests.

Cellular distribution of Hyp-apoMb by STED imaging

Super-resolution microscopy methods [89] [60] can allow the study of PS distribution in cellular environments at high spatial resolution.

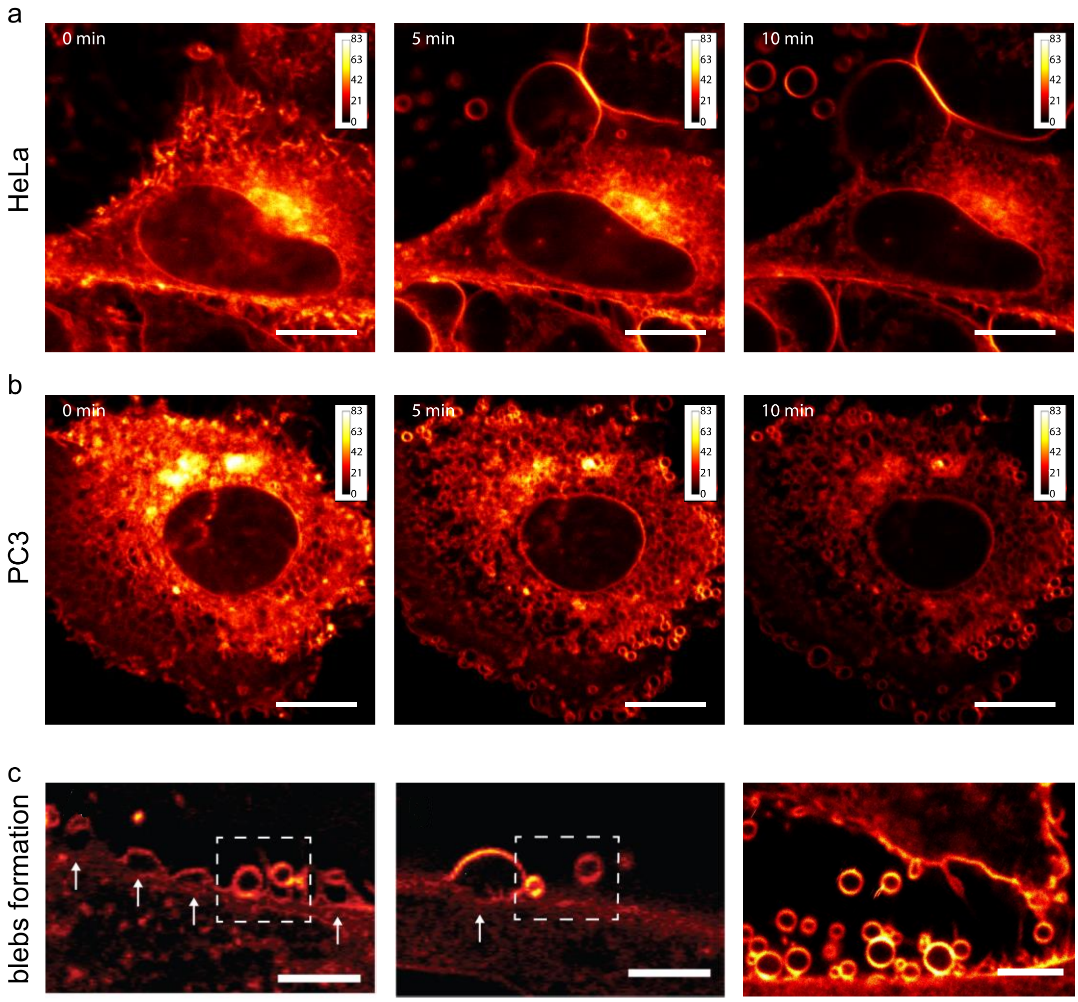

*Fig. 4.14 Photoinduced damage to HeLa and PC3 cells incubated with Hyp-apoMb. Effect of illumination by STED imaging on HeLa (**Panels a**) and PC3 cells (**Panels b**) incubated for 30 minutes with Hyp-apoMb (0.5 µM Hyp, 1.5 µM apoMb) after 0, 5 and 10 minutes of irradiation. STED images collected under excitation at 566 nm and detection at 605\70 nm. The STED beam was at 715 nm, power 8 mW, and dwelled time 0.05 ms. **Panels c** show close-up images on swelling and vesicle formation as a consequence of the photoinduced damage on the plasma membrane on HeLa cells. Scale bars, 10 µm.*

In fact, the inherent bright fluorescence emission by Hyp could be exploited to collect STED images of bacterial cells loaded with Hyp-apoMb [74][90][59].

In this case, STED nanoscopy, was applied to follow the uptake of the PS and to distinguish the possible different mechanisms that occur in cells when it is present either Hyp or Hyp-ApoMb.

STED images of HeLa and PC3 cells incubated with Hyp-ApoMb (0.5 µM Hyp, 1.5 µM apoMb) for 30 minutes is reported in Fig. 4.14 Panels a and b (at time 0 min). These images highlight the accumulation of the PS on the plasma membrane as well as within the cytoplasm, whereas the cell nucleus results in devoid of fluorescence emission. The behavior is the same for both types of cells. The intense fluorescence emission indicates that the molecules are in the monomeric state, which represents a significant advantage over other nanostructured PSs systems for which a clear tendency to aggregate was sometimes evidenced. [91]. Fluorescent molecules are photoactive, and the photo-oxidative damages depend on molecular distribution.

When using STED microscopy, cell exposure to strong laser light produces a quickly extensive cell damage. The plasma membrane is damaged a few minutes after illumination, as shown in the central panels of Fig. 4.14 (a and b) when compared to non-irradiated HeLa and PC3 cells (Fig. 4.14 a and b, left panels). Damages consist of the formation of swelling areas in the plasma membrane in localized regions. The cell size increases and vesicles are formed, and they eventually detach from the cell. In particular, Fig. 4.14, panels c**,** offers close-up views on extensive swelling regions where the photo-oxidative damage concentrates. The left and center images of panel c show regions where vesicles are forming (at points indicated by the arrows) and detach (within the dashed line box). An area with an intense vesicle formation is reported in panel c. There is a large variability of vesicle diameters. In the same panel, it is also evident the loss of integrity of several regions of the plasma membrane.

Spinning disk imaging: photosensitizer uptake of Hyp and Hyp-apoMb.

As shown, super-resolution images obtained by exploiting STED nanoscopy demonstrate that under intense illumination the photo-induced oxidative stress strongly damages the plasma and internal membranes. This imaging method is unsuitable to follow PSs cellular uptake in time. The intense STED laser beam (fluence rate ~10MW/cm^2 in the focal plane) produce a severe photo-oxidation damage that far exceeds the standard experiments encountered for PDT applications on cultured cells where the light intensity is on the order of 10-30 mW/cm^2. Such damage generates a progressive and concomitant change in the transport properties of the system and results in a greatly accelerated PS uptake.

Therefore, we decided to sacrifice spatial resolution in favor of a less invasive imaging technique. Spinning confocal disk microscopy seems a good compromise, in fact, allow to keep sectioning capability and an excellent resolution. This methodology leads to a substantial reduction in the frame acquisition time (one frame in 0.2 s), the number of averages (only 2 to optimize the signal-to-noise ratio), and laser power (132 μW). Additionally, to decrease photodamages, it was used low PSs concentrations (50nM), which is high enough to observe a detectable action against cells. Overall, this decreased the photo-oxidative damage during image acquisition and allowed us to follow the uptake of the PS by cells over a ~50-minute time window (every minute for the first 11 minutes and one frame in 0.2 s every 5 minutes for 40 minutes), without any interfering photo-oxidative damage. Fig. 4.15 panels a and b, shows examples of Hyp and Hyp-apoMb uptake time sequences by HeLa cells. A simple visual inspection of the images allows appreciating a remarkable difference in the PS loading mechanism. In the case of Hyp administered from a concentrated DMSO solution, the fluorescence grows homogeneously in the whole cell structure. On the other hand, when Hyp-ApoMb is delivered to the cell culture, fluorescence appears to be initially concentrated mostly at the plasma membrane, where the PS concentration appears higher than in the cytoplasm at all times. Similar results were obtained on PC3 cells.

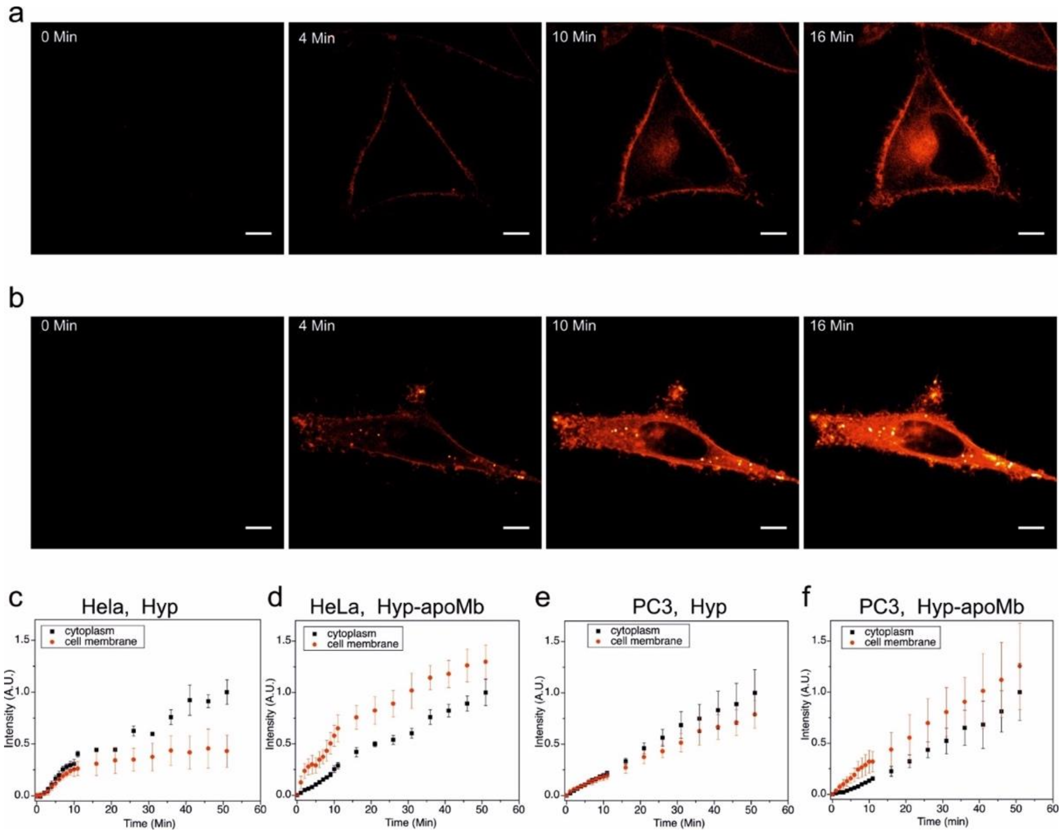

Fig. 4.15. Uptake dynamics of Hyp and Hyp-apoMb.
*Comparison between the accumulation of Hyp (50 nM) in HeLa cells at selected delays when the PS is delivered bound to apoMb (**Panels a**) and when delivered without a carrier (**Panels b**). Experiments on PC3 cells gave similar results. Images were collected with a spinning disk microscope with excitation at 561 nm (power 132 μW). It Was acquired one image (0.2 s frame acquisition time) every minute for the first 10 minutes and one image (0.2 s frame acquisition time) every 5 minutes for the last 40 minutes. Scale bar 10μm (Panels a and b).*
***Panels c-f.** Hypericin fluorescence intensity for the plasma membrane and for the cytoplasm calculated from images collected at increasing delay after Hyp or Hyp-apoMb was added to the solution.Cellmask deep red was used to mark the mebrane to obtain a reference (see Materials and methods section 3.4) . Plots refer to HeLa cells (c, d) and PC3 cells (e, f) treated with Hyp (c, e) and with Hyp-apoMb (d, f). Intensity values are calculated for several cells, and the error bars represent cell-to-cell variability. The intensity curves are normalized to the maximum fluorescence value observed for the internal part of the cell.*

In order to quantitatively study the variations in time of the fluorescence intensity on the plasma membrane after injection of Hyp or Hyp-apoMb to the buffer where cells are held, cells were labeled by “CellMask™ Deep Red Plasma Membrane Stains.” This stain allows maintaining a reference for the position of the membranes preventing excessive excitation of Hyp. Using this reference signal, it was possible to determine the fluorescence emission intensity at selected positions (See materials and method 3.4). Then the fluorescence intensity at the plasma membrane and in the cell interior (cytoplasm and inner membranes) was plotted in function of time (Fig 4.15 panels c-f).

The trends of the Hyp uptake when delivered in complex with ApoMb or alone show significant differences. In particular, it is evident that the rise fluorescence at the plasma membrane (red symbols in Fig. 4.15 panels d and f) is much faster when cells are treated with Hyp-apoMb. The time scale of the concentration increase at the plasma membrane is about 5-10 minutes from the administration. Moreover, the presence of the protein carrier leads to higher concentrations of the PS on the plasma membrane than on the inner membranes. This represents an advantage when it is essential to induce photodynamic action in short times after the drug administration.

Since ApoMb is a water-soluble protein without any known specific affinity for plasma membrane components, it remains to be understood whether the higher PS uptake involves unreported interaction with the cell structure. In order to further comprehend the action of the complex Hyp-apoMb, we covalently labeled Fluorescein-5-Isothiocyanate (FITC) to ApoMb. Such labeling allowed us to study the fate of the ApoMb and the pay load Hyp independently during the uptake process in HeLa and PC3 cells.

In Fig. 4.16 for PC3 cells**,** green fluorescence from FITC-labelled ApoMb is appreciable only from the buffer medium and is not detectable either on the cell membrane or inside the cell. In contrast, the red fluorescence emission from Hyp is observed from the plasma membrane as well as from the internal membranes and reflects the distribution (after incubation and uptake) reported in Fig 4.14 and 4.15. Similar results were obtained for HeLa cells. These findings suggest that apoMb mostly acts as a passive carrier that facilitates the delivery of Hyp to the membranes by preventing aggregation in the aqueous phase. The higher affinity of the PS for the lipid phase leads to the fast partitioning of Hyp, leaving the unloaded protein in solution.

The water-soluble protein carrier is very useful in preventing Hyp aggregation, and when the Hyp-apoMb solution is injected into the buffer medium, covering cells in the wells, the Hyp, in the monomeric state, bound to ApoMb is rapidly and efficiently transferred to the plasma membrane. It speeds up cell loading and allows us to increase the bioavailability of the PS compound. This mechanism is not present when Hyp is added to the solution without the protein carrier. In these conditions, right after injection to the cell-bathing buffer, PSs result extensively aggregated, and the rescue of aggregated PSs molecules is a slower and less efficient process. Thus, we can conclude that Hyp-ApoMb remarkably increases PSs bioavailability.

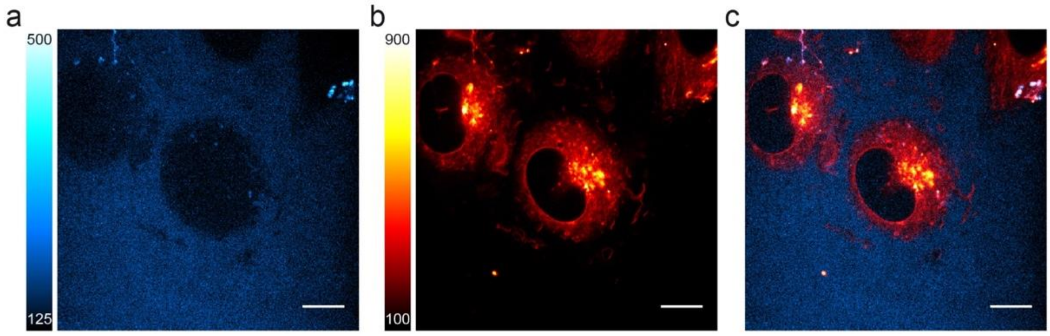

Fig. 4.16. Hyp-apoMb-FITC imaging. Spinning Disk Fluorescence Imaging of PC3 cells treated with Hyp-apoMb (a) in the FITC channel (500-550 nm) shows the distribution of apoMb, in comparison with (b) the red channel (575-605 nm) that shows Hyp distribution. (c) Overlay of the two images [ApoMb] = 10 μM, [Hyp] = 3 μM. The incubation time was 1 hour. Scale bars are 10μm. FITC channel is excited at 488nm, Exposure time 400ms, power 324μW; Hypericin is excited with the laser at 561nm, exposure time 100ms, power 567μW, for both channels the pixel size is 0.14μm.

Tumor spheroid treated with PS.

We have shown that uptake of the PS is faster and more efficient for Hyp-ApoMb than for Hyp in bi-dimensional cell cultures, but it is not obvious that this advantage is preserved in tumor tissues. Thus, we used tumor spheroids as a three-dimensional model system to study the uptake of the PS. Spheroids are considered a good model for small solid tumors before neovascularization [92][93]. HeLa cells were transfected with the far red-emitting fluorescent protein miRFP703 [75] fused to histone H2B to visualize the cell nucleus and to monitor the size of the spheroid. Since such a fluorescent protein has excitation and emission spectra in the far red, it is particularly suitable for imaging thick samples and scattering objects as tumor spheroids. In Fig 4.17, was showed the effects of Hyp and Hyp-apoMb on HeLa spheroids.

In the control spheroids, which are not exposed to the microscope light (Fig. 4.17 a), we did not observe any evidence of morphological damages induced by phototoxicity; in fact, they grow normally. Although the size of Hyp-apoMb is significantly larger than that of Hyp, steric effects do not impair penetration of the drug. Thus, uptake through the spheroid occurs both for Hyp (Fig. 4.17 b) and for Hyp-apoMb (Fig. 4.17 d). However, as noted, for cultured single-layer cells, the concentration of the fluorescent species is higher when Hyp-apoMb is used (Fig. 4.17 d). The difference between the two cases is at least one order of magnitude. After irradiation, the cells in the outer layer die, and in the short term (1 week), the growth of the spheroids is completely blocked (right images in panels c, and e). A few documented difficulties hamper a more quantitative estimation of the efficiency of the phototoxicity on the spheroid. These include low oxygen content in the inner parts of the spheroid [94] and uneven distribution of the PS, which is found at lower concentrations in the center [95][96]. Initial accumulation at the spheroid rim was also reported for treatments of spheroids with hypocrellin-loaded liposomes, followed by a more even distribution of the PS at longer times [97]. This delayed kinetics most likely derives from the high affinity of Hyp for liposomes that may transiently hold the photosensitizers and prevent binding to the plasma membrane of tumor cells.

Definitely, Hyp-ApoMb potentially offers advantages in terms of delivery rate, since fluorescence is also detected in the center of the spheroid (although at a lower concentration than at the periphery) after just one-hour incubation time (Fig. 4.17 d). The moderate affinity of Hyp for apoMb and the high affinity for lipid membranes mean that, when Hyp-apoMb is in the presence of tumor cells, Hyp will be quickly released by the protein in favor of the lipid phase.

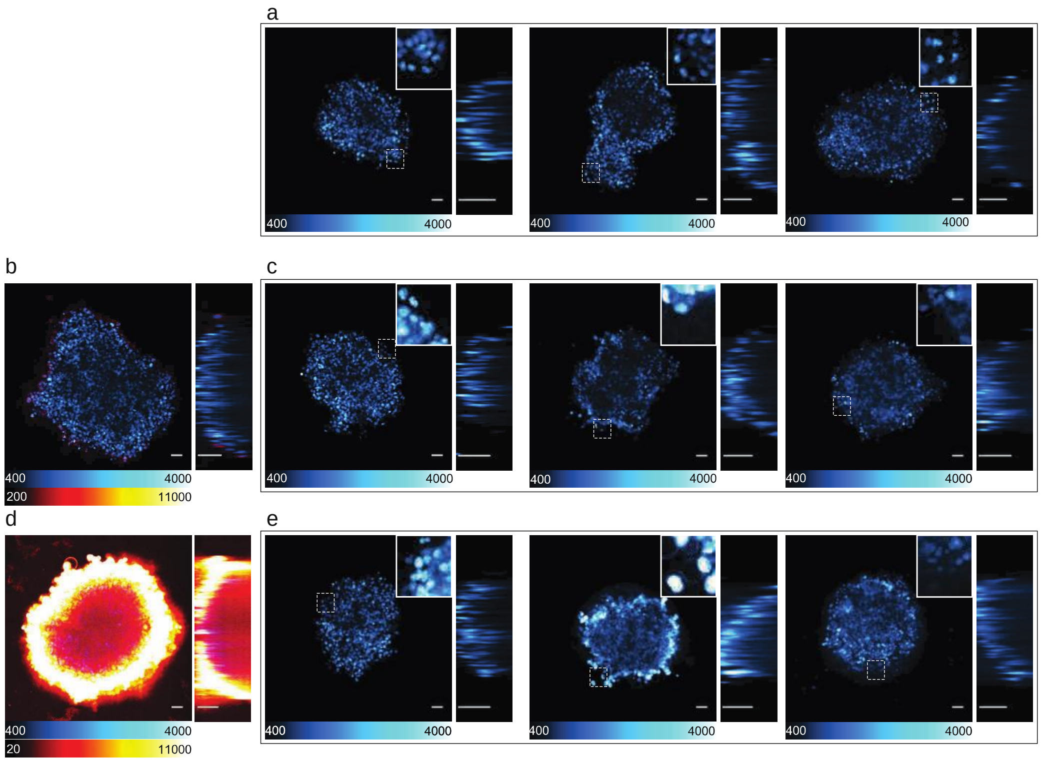

Fig. 4.17 Effects of Hyp and Hyp-apoMb on HeLa tumor spheroids upon light irradiation. Spinning disk imaging of HeLa cells permanently transfected with miRFP703-H2B (shown in cyan-hot) (a-e) and treated with Hyp (1 μM) (b and c), and with Hyp-apoMb (1 μM) (d and e). The samples in a, b, and c were incubated 1h with Hyp. The samples in d and e were incubated 1h with Hyp-apoMb. Panels a, c and e, are time sequences at days 0, 1, and 6. Samples were illuminated at day 0 for 5 minutes at 561 nm with power 3.37 mW. Each image is composed of inset with a 3x magnification of the squared area defined with a dashed line, and by an orthogonal projection of the middle plane, yz. Scale bar is 50 μm, voxel size is 1.6 x 1.6 x 1.4 μm.

4.2.2 Zinc phthalocyanine

A particular class of PSs, called Phthalocyanines (PCs), were objects of study for PDT applications. The high absorbance maximum in the near-infrared spectrum, necessary for an optimal tissue light penetration, the molar extinction coefficient at 674 nm of 2,8 × 10^5(cm^{-1} M^{-1}), the triplet lifetime of the order of microsecond and the high singlet oxygen quantum yield are characteristics that make PCs ideal candidates for PDT.

PCs form various chelates state with several metallic ions, giving a longer triplet lifetime and allowing high singlet oxygen quantum yield (ΦΔ) that for example for Zinc phthalocyanine (ZnPc) reaches the value of 0.67 [98].

The main drawback of these molecules is the formation of aggregates that cause a substantial decrease in molecule bioavailability involving a drop in their efficacy. Typically is possible to bind Phthalocyanine to Apomyglobin, obtaining a stable complex with an association constant of $(9.0 \pm 0.6) \times 10^4\ M^{-1}$ [77]. When we compared cells treated with PS bound to ApoMb (Fig.4.18) was observed an increase of phototoxicity respect to only PS administration. Illumination without PS is not toxic. Measurements were done at the same PSs concentration [100 nM] and illumination. The incubation time was 1 hour.

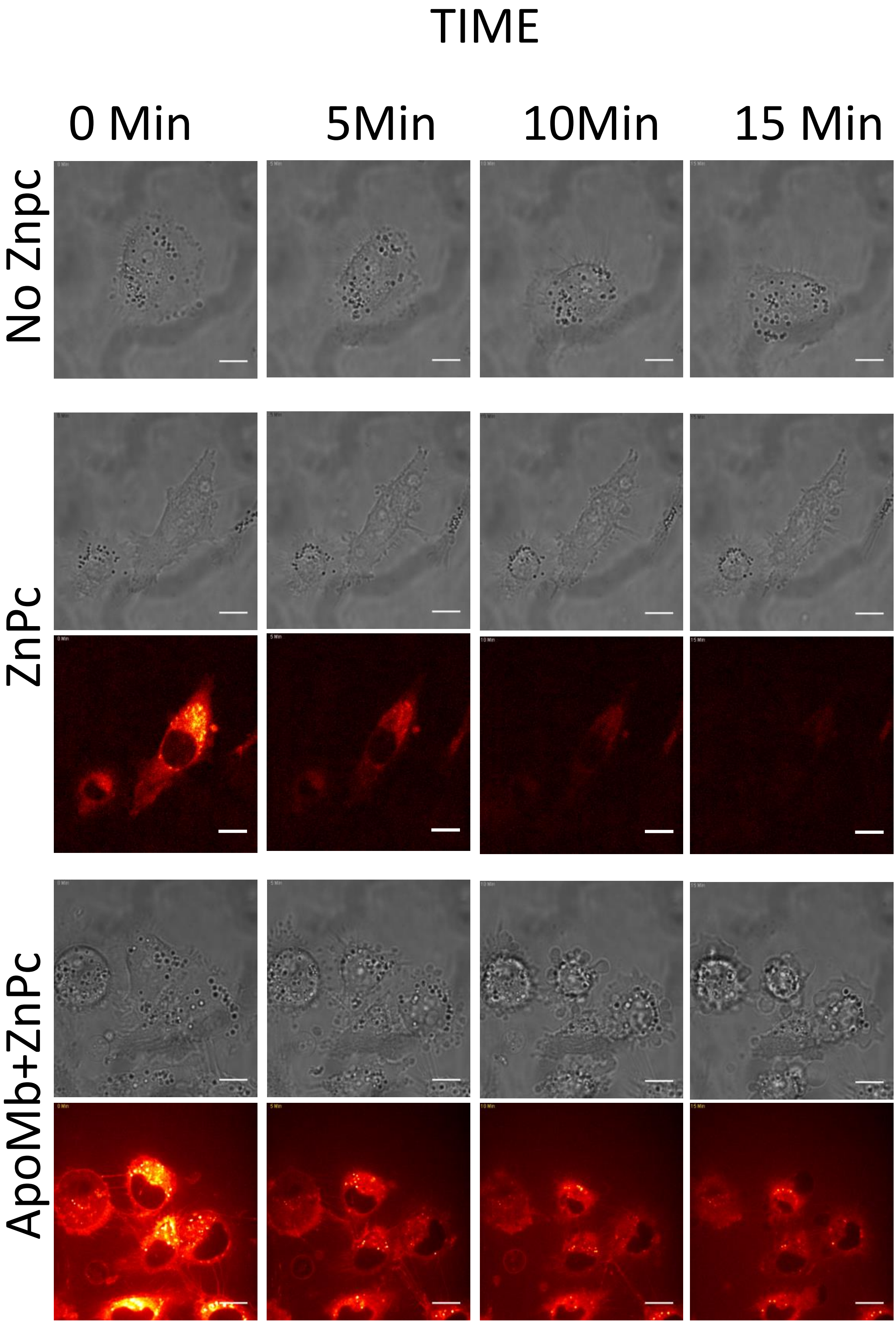

Fig. 4.18 Pc3 illuminated without PS, cellular damages [100nM] ZnPc, and ZnPc+ApoMb [100nM] transmission and fluorescence channels at zero, five,

ten, and fifteen minutes (Scale bar 10μm). Image acquisition was made with a frame rate of one per minute for 19 minutes, laser power of (389μW), and exposure (500 mS) with 100x objective 1.4NA. The images are 512x512 with a pixel size of 0.249μm/px. 8 averages were performed to minimize the noise. All measurements were done with an incubation system.

ZnPc and ZnPc+ApoMb uptake

At this point we also investigated cellular uptake and the accumulation differences between the membrane and the cytoplasm both for ZnPc and ZnPc+ApoMb complex. The study of PSs accumulation in time was performed using spinning disk confocal microscopy (Fig 4.19).

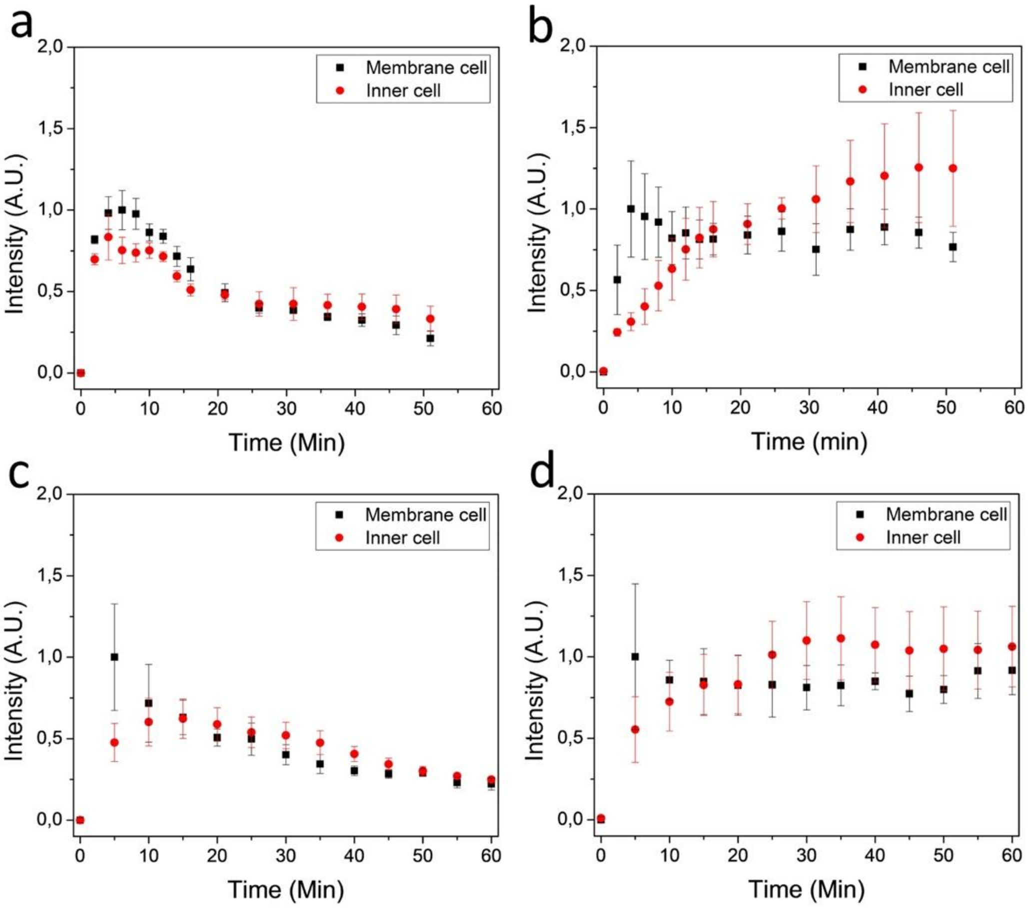

Fig. 4.19 Uptake of ZnPc [100nM] in HeLa cells (a) and PC3 cells (c); ZnPc+ApoMb [10nM] in HeLa cells (b) and Pc3 cells (d)

We acquired one frame every 2 minutes for the first 16 minutes, and finally, one frame every 5 minutes in order to minimize the cellular damages. Moreover, a concentration of 100 nM for ZnPc and 10 nM for ZnPc-ApoMb were respectively used. It was crucial to set these conditions because a higher concentration of the complex ApoMb-ZnPc causes serious cellular damage, while for much low PS concentration we have too low fluorescent signals. This is an additional aspect that shows the difference in the bioavailability of these two species. The ZnPc accumulation curves (Fig.4.19 a-c) are characterized by a fast decrease of the fluorescent signal and loss of the PS molecules. In addition, PS aggregation in solution occurred. Aggregation is an irreversible process and the the replacement with new monomeric molecules did not occur.

Instead, using the complex ZnPc-ApoMb (Fig. 4.19 b-c), it is possible to notice an increase of bioavailability. Indeed, the accumulation curves show an equilibrium between the complexes ZnPc-ApoMb and ZnPc-cells, the concentration of our PSs remains constant involving a phototoxicity increase.

Toxicity test

Finally, three-colors large images were acquired using live HeLa cells. The first two channels show live (green) and dead (red) cells, while the last one shows ZnPc (Cyan). Dark toxicity test was performed (Fig. 4.20 A-B-C-D) for analyzing the biocompatibility and bioavailability of our PS molecules (Fig. 4-20 A-D) and the complexes (Fig. 4.20 B).

Besides, the phototoxicity test in the absence of the complex (Fig. 4.20 F), used as a negative control (Fig. 4.20 E), was performed in order to compare the potential photo-toxicity induced by PS photoactivation.

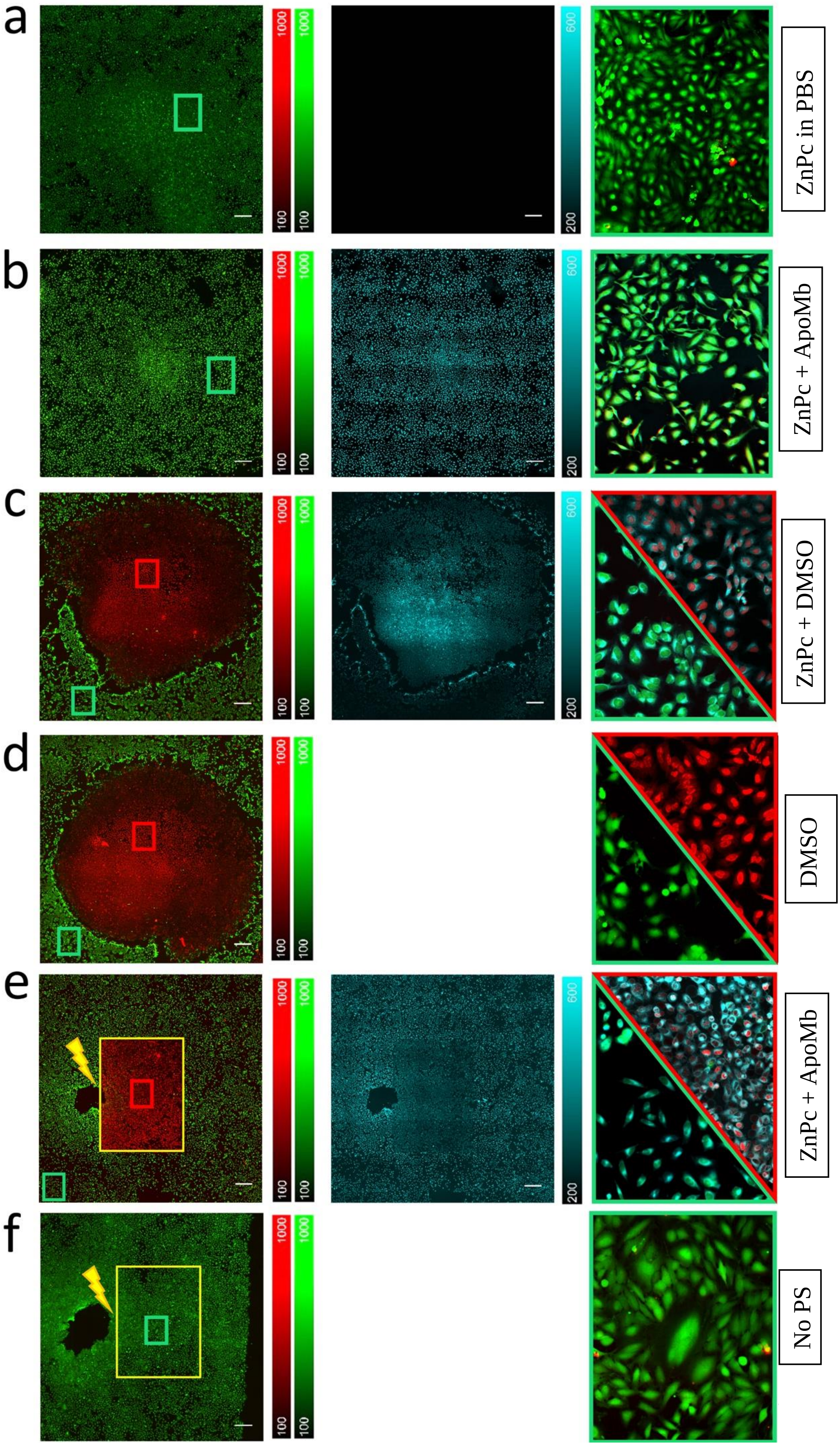
a
1000
100
1000
100
600
200
ZnPc in PBS
b
ZnPc + ApoMb
c
ZnPc + DMSO
d
DMSO
e
ZnPc + ApoMb
f
No PS

Fig. 4.20. Dead cells red, live cells green, ZnPc cyan, scale bars are 500 μm. Hela cell with ZnPc 500nM solved in PBS (A), ZnPc+ApoMb 100nM (B), ZnPc 500nM solved in DMSO (C), 5.2μl DMSO (D), illumination in the center region for 5min at 647nm with power of 2.5mW in presence of ZnPc-ApoMb complexes (E) and without PS (F) Image acquisition was performed using 4x objective 0.45NA for the large image and a 20X for the inset. Images are 512x512 pixels.

These measurements show that ZnPc is only soluble in DMSO though in this condition (Fig. 4.20 C) our PS is not compatible with the biological sample. Indeed, in the injection region we noticed cellular death due to DMSO as well as not uniform distribution of ZnPc. Moreover, at a longer distance from the injection point, we observed an increase of the PSs aggregation (i.e. less fluorescence). Moreover, it is not possible to use ZnPc in aqueous solution, because of aggregates formation, which drastically decreases the bioavailability of our PS (Fig. 4.20 A). Instead, using the complex ZnPc-ApoMb allows dissolving ZnPc in aqueous solutions efficiently. In this way, we obtain uniform distribution in the biological sample, an increase in biocompatibility and bioavailability (Fig. 4.20 B). Also, these data demonstrate the high toxicity of our complex when excited with light, while outside the illuminated area, our complexes result atoxic for specimens (Fig. 4.20 E). In fact, the control test shows that illuminating without the administration of PS is not toxic (Fig. 4.20 F).

4.2.3 Zinc Myoglobin

In the myoglobin the heme group cannot produce singlet oxygen [31], but the heme iron chelation can occur. During periods of iron insufficiency or impaired iron utilization by the organism, zinc becomes an alternative metal substrate for ferrochelatase, leading to increased ZnPP (Zinc ProtoPorphirin) formation [99].

These molecules have a quantum yield of a single oxygen generation of $\Phi_\Delta = 0.91$ [100]. Such a relevant value is of significant importance and makes this molecule a good PS with promising potential in photodynamic therapy.

The high quantum yield for singlet oxygen generation corresponds to a lower fluorescent quantum yield (Φ_F =0.03) [31].

Cellular uptake study

Since this PS is directly based on myoglobin is hydrophilic, and does not accumulate spontaneously in the cell membranes.

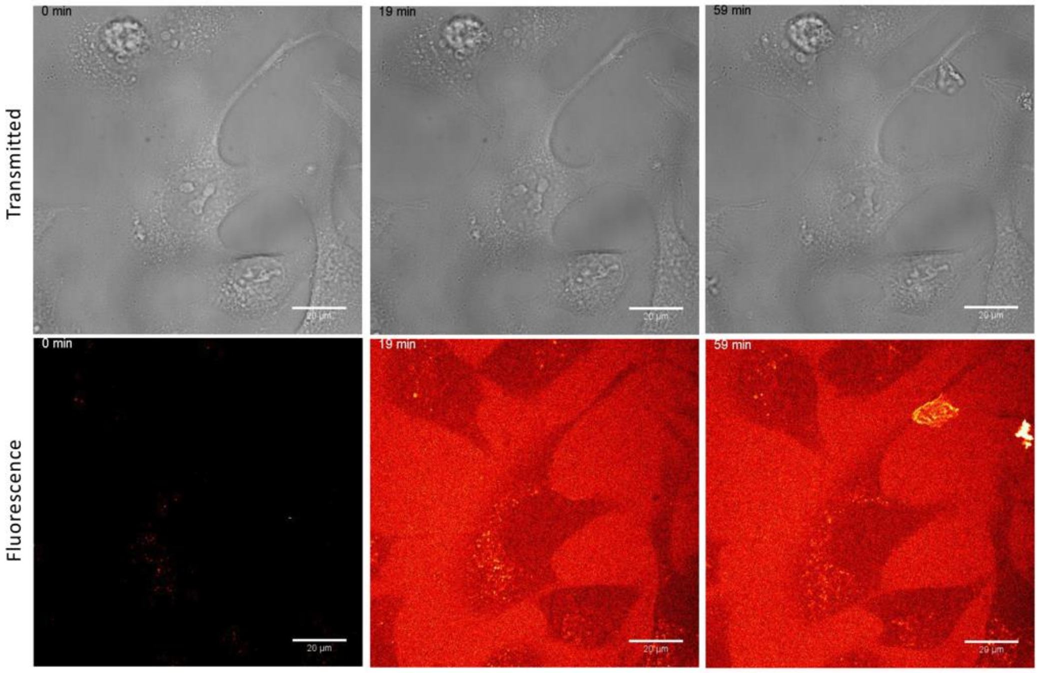

Fig. 4.23 Fast confocal spinning disk fluorescence imaging of HeLa cells treated with Zinc-Myoglobin at 0, 19 and 59 min of accumulation time. Time-lapse one frame each 2 min for the first 14min and 1 frame each 5 min to 69 min. Excitation 561 nm, emission 592/22 nm, exposure time 100 ms. For all the images, the pixel's area is 512x512, and the pixel size is 0.23 µm. 0 time without PS.

So myoglobin re-formed with Zn-protoporphyrin IX (ZnMb) is characterized by high efficiency of production of singlet oxygen, but, as is shown in Fig. 4.23, it has no specificity for cells. In fact, ZnPP IX molecules result diffused in all the samples, and no accumulation in the cells is observed. This compromises the efficiency of the PS for PDT.

However, it is possible to engineer the protein part of this PS with a specific peptide able to bind one of the receptors overexpressed in tumor tissues.

The peptide, called Vasoactive Intestinal Peptide (VIP), is a neurotransmitter and a peptide hormone belonging to the glucagon-secretin family, located mainly in intestinal and nervous tissues. Among its functionalities, there are vasodilation, prolactin release, and intestinal and pancreatic secretion [101]. Furthermore, the VIP can carry out a transport action towards neoplastic tissues since the presence of its receptors in different tumor cells has been identified [102].

This peptide bonded to ZnMb protein allows the accumulation of these proteins in tumor cells, causing cell death, as shown in Fig. 4.24

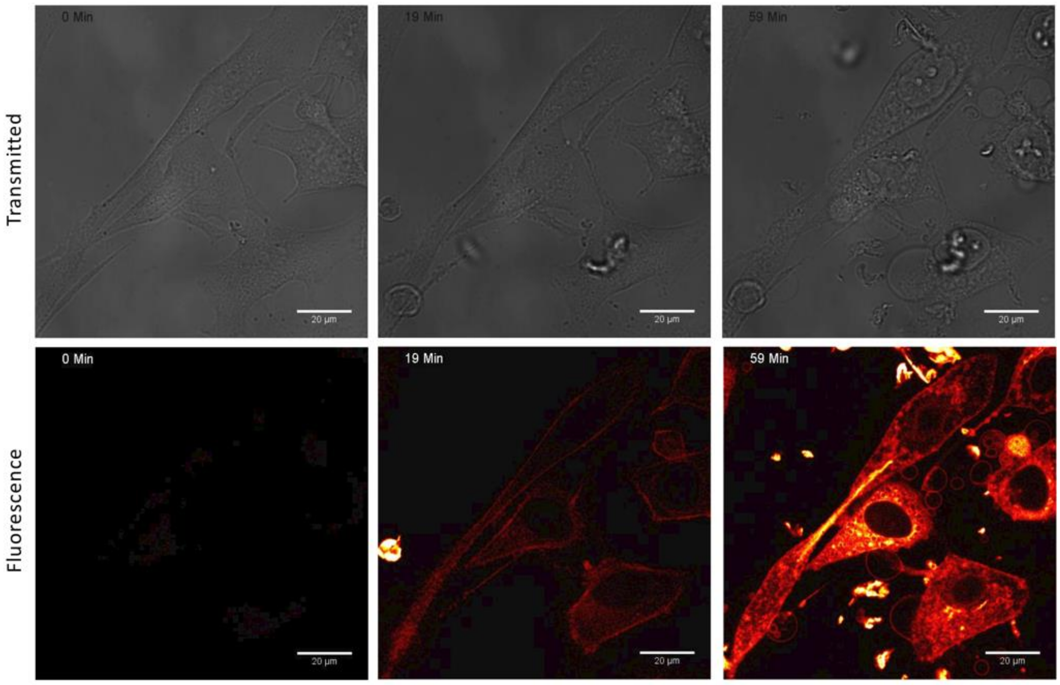

Fig. 4.24 Fast confocal spinning disk fluorescence imaging of HeLa cells treated with Zinc-Myoglobin VIP at 0, 19 and 59 min of accumulation time. Time-lapse one frame each 2 min for the first 14min and 1 frame each 5 min to 69 min. Excitation 561 nm, emission 592/22 nm, exposure time 100 ms. For all the images, the pixel's area is 512x512, and the pixel size is 0.23 µm. 0 time without PS.

4.2.4 Curcumin

Turmeric (*Curcuma longa* rhinzomes), commonly used as a spice, is well documented for its medicinal properties in Indian and Chinese systems of medicine. It has been widely used for the treatment of several diseases. Epidemiological observations, though inconclusive, are suggestive that turmeric consumption may reduce the risk of some form of cancers and may have other protective biological effects in humans. These biological effects of turmeric have been attributed to its constituent called curcumin. Curcumin was widely studied for its anti-inflammatory, anti-angiogenic, antioxidant, wound healing, and anti-cancer effects. [103]

Curcumin exhibits a variety of biological and photochemical activity, including phototoxicity. [104]

This PS is unstable in water, and its spectral properties undergo major changes within minutes from the preparation of the solutions. On the contrary, in ethanol solutions, curcumin spectral properties are stable over days.

The spectral instability observed in PBS solutions poses limitations in the use of this PS for applications in PDT and for antibacterial treatments.

Oxidation of the compound may be prevented or at least made less efficient if a delivery agent is used to solubilize curcumin in water [105].

Using BSA, Curcumin results stable over at least 5 hours and comparing the use of the only curcumin with curcumin-BSA, the concentration at which we have a 50% reduction of cell viability results 3-times lower when curcumin is bound to the carrier. [105]. This difference can be led back to a different accumulation of the PS using BSA as a carrier.

Mytotraker Colocalization study

When curcumin is delivered to cultured cells using a concentrated ethanol solution, fluorescence is observed from inside the cellular structures after just a few minutes of incubation.

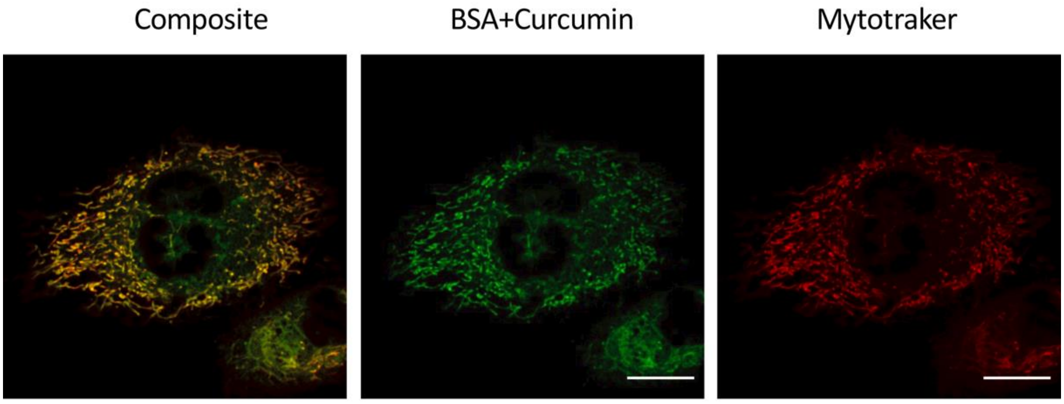

Fig. 4.21. Fast confocal spinning disk fluorescence imaging of HeLa cells incubated 15 min with mitoTracker Deep red [0.3 μM], and 10 min with curcumin [15 μM]. Curcumin channel: excitation 405 nm, emission 460/60, exposure time 50 ms. Mitotraker channel: excitation 633 nm, emission 700/75 nm, exposure time 200 ms. For all the images, the pixel's area is 512x512, and the pixel size is 0.16 μm. Scale bar 10 μm.

Fig. 4.21 shows that fluorescence emission from curcumin co-localizes with the fluorescence emission from MitoTracker red. Thus, the accumulation of curcumin when delivered without a carrier occurs at the mitochondria level. Curcumin shows preferred association in model lipid bilayers with cardiolipin, which is a lipid molecule exclusively localized in the inner mitochondrial membrane. In keeping with our findings, fluorescence from curcumin was demonstrated to co-localize with mitochondria within cells. [106] The interaction of curcumin through cardiolipin-mediated interactions with mitochondrial membranes was suggested to be an underlying responsible factor for the high efficacy of this compound against metabolic diseases. Moreover, when curcumin accumulates inside mitochondrial membranes can also have adverse effects on cells. Curcumin and curcumin derivatives targeting mitochondria exhibited significant cytotoxicity towards several cancer cell lines, inducing significant ROS generation, cell-cycle arrest, and apoptosis. [107]

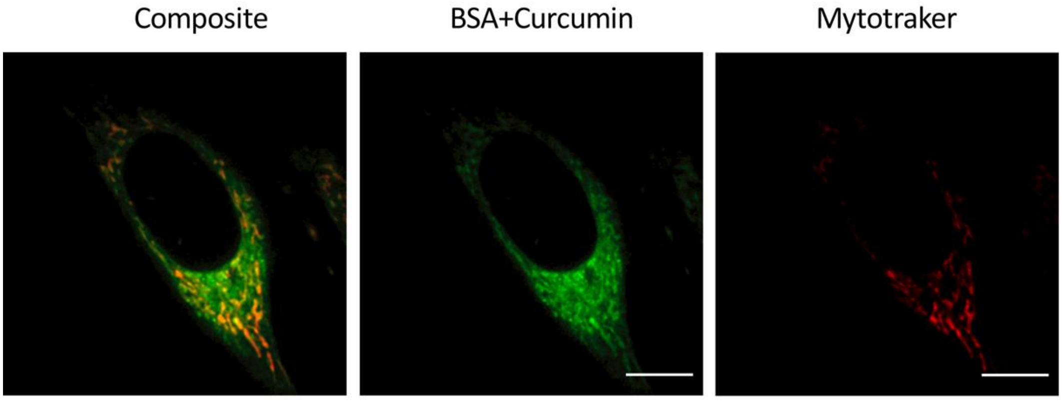

Fig. 4.22. Fast confocal spinning disk fluorescence imaging of HeLa cells incubated 15 min with mitoTracker Deep red [0.3 μM], and 10 min with curcumin-BSA [15 μM]. Curcumin channel: excitation 405 nm, emission 460/60, exposure time 50 ms. Mitotraker channel: excitation 633 nm, emission 700/75 nm, exposure time 200 ms. For all the images, the pixel's area is 512x512, and the pixel size is 0.16 μm. Scale bar 10 μm.

Fig. 4.22 shows that when HeLa cells are incubated with curcumin-BSA the distribution of the compounds appears different from that observed for curcumin alone. While it co-localizes with mitochondria there is a diffuse fluorescence in a large area in the cytoplasm, from curcumin in addition to. The homogeneous loading of the cell appears to be a direct consequence of the higher bioavailability of the photoactive compound when delivered bound to BSA.

The lack of aggregation and the increased stability of curcumin mean that the compound is accessible at higher concentrations and for longer times so that the uptake from cells is more diffuse. In the presence of HeLa cells, it is expected that fully photoactive curcumin is efficiently transferred to the cell structures by the carrier protein, due to the higher affinity of the compound for lipids and possibly for other macromolecules endowed with hydrophobic binding sites.

The broader distribution of curcumin-BSA may be responsible for the more extensive damages induced by the illumination of HeLa cells.

Chapter 5: Conclusions

5.1 Rubi-GABA uncaging

In conclusion, the study of the uncaging process and its critical parameters allows understanding its influence in the electrophysiological measurements.

Never the less it demonstrates that it can be used to map the distribution of functional $GABA_A$ receptors in different regions of neurons, using uncaging points in specific areas such as the cell body, axons or dendrites (fig. 4.7).

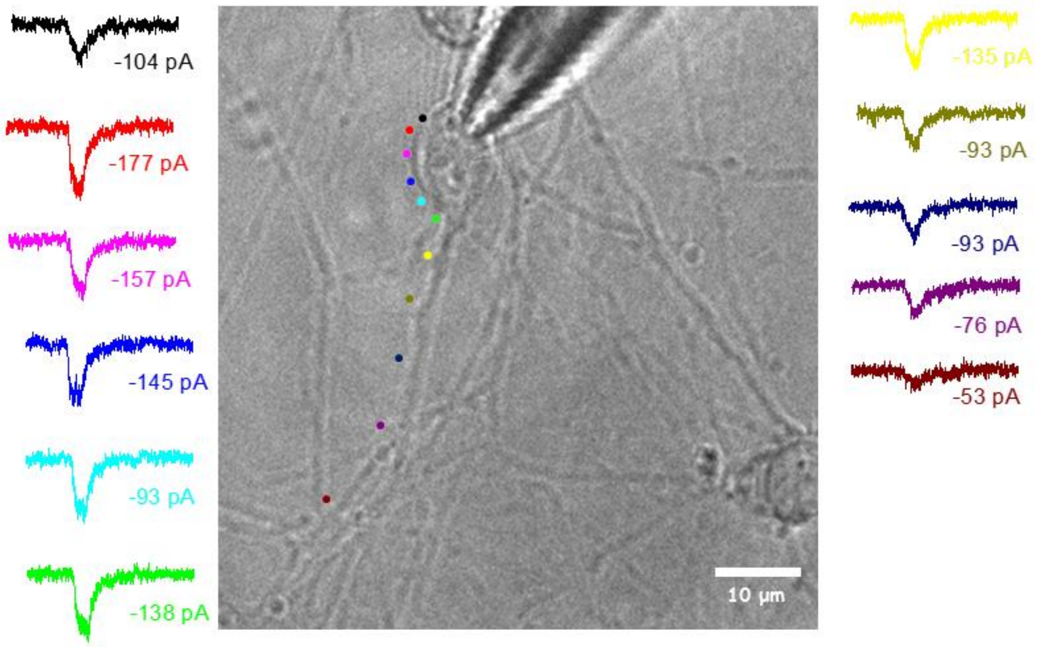

Fig. 4.7: *Currents related to several uncaging points in different parts of a neuron during 2PE (750 nm, 100 ms, 77.3 mW) of 10 µM RuBi – GABA; among the measurements, it waited that the current returned to the initial status.*

In the figure several current measurements after a sequential uncaging of 10 µM RuBi – GABA are pointed out in different parts of a neuron: moving the photoactivation point from the cell body, the current decreases, suggesting that the receptor density in the neuronal extensions is lower than in the soma.

The future aims of this approach are: (i) map the receptor subtypes with fluorescence staining for the different subunits and with antagonist molecules that block the receptor binding sites and (ii) study how the receptor density may change in a precise area after treatment with drugs such as benzodiazepines.

5.2 Photosensitizers

The study of photosensitizers coupled with protein carriers shows that PSs form stable complexes with protein carriers such as ApoMb and BSA. Using these molecules, we were able to induce cellular death by light in a specific region of biological specimens. Complex formation preserves the monomeric photoactivable state of the PS and increases its biocompatibility, bioavailability, and phototoxicity, even at low concentrations upon illumination.

Delivery of PS with protein has an impact on the intracellular distribution of the compound. For example, we have seen that when curcumin is delivered without the protein carrier, it is mainly localized in the mitochondria. While, when curcumin is bound to BSA, the cellular distribution appears more homogeneous, likely associated with a variety of target structures.

In addition, it is possible to modify the PS accumulation dynamics. We showed that the Hyp-ApoMb complex allows a preferential accumulation in the external membrane, compared to the only Hyp. It results efficient when applied to 3D tissues such as tumor spheroids. The use of protein carriers produces an increase in bioavailability of the PS.

Finally, it was possible to engineer proteins with a particular linker that would allow them to be selectively targeted to tumor cells (i.e. being able to distinguish healthy cells from tumor cells), thus, increasing the sensitivity and selectivity of the PDT. All these characteristics allow increasing the efficacy and the phototoxicity of these PSs that are essential to reduce the concentration of PSs necessary for cell death, avoiding side effects. In summary, the use of protein carrier systems makes PSs powerful candidates in the PDT application.

Chapter 6: List of Publications

APOMYOGLOBIN IS AN EFFICIENT CARRIER FOR ZINC PHTHALOCYANINE IN PHOTODYNAMIC THERAPY OF TUMORS
Cozzolino M., Pesce L., Pezzuoli D., Montali C., Brancaleon L., Cavanna L., Abbruzzetti S., Diaspro A., Bianchini P., Viappiani C.
Biophysical Chemistry, 2019,

ENHANCED PHOTOSENSITIZING PROPERTIES OF PROTEIN BOUND CURCUMIN
Cozzolino M., Delcanale P., Montali C, Tognolini M, Giorgio C., Cavanna L., Bianchini P., Diaspro A., Abbruzzetti S., Viappiani C.
Life Sciences, 2019

S. SERUM ALBUMINS ARE EFFICIENT DELIVERY SYSTEMS FOR THE PHOTOSENSITIZER HYPERICIN IN PHOTOSENSITIZATION BASED TREATMENTS AGAINST STAPHYLOCOCCUS AUREUS.
Pezzuoli, D.; **Cozzolino, M.**; Montali, C.; Brancaleon, L.; Bianchini, P.; Zantedeschi, M.; Bonardi, S.; Viappiani, C.; Abbruzzetti,
Food Control 2018,

MEASURING EXPANSION FROM MACRO- TO NANOSCALE USING NPC AS INTRINSIC REPORTER.
Pesce, L.; **Cozzolino, M**.; Lanzanò, L.; Diaspro, A.; Bianchini, P.
J. Biophotonics 2019.

HYPERICIN–APOMYOGLOBIN: AN ENHANCED PHOTOSENSITIZER COMPLEX FOR THE TREATMENT OF TUMOR CELLS.
Bianchini, P.; **Cozzolino, M.**; Oneto, M.; Pesce, L.; Pennacchietti, F.; Tognolini, M.; Giorgio, C.; Nonell, S.; Cavanna, L.; Delcanale, P.; Abbruzzetti, S.; Diaspro, A.; Viappiani, C..
Biomacromolecules, 2019.

PRECISE CONTROL OF ELECTRICAL AND OPTICAL PARAMETERS IN 3D MODULATION OF GABAA RECEPTORS IN VITRO.
Cozzolino, M.; Bazzurro,V.; Gatta, E.; Bianchini, P.; Angeli, E.; Robello, M.; Diaspro, A..
Submitted.

References

[1] Raymo F M 2012 Photoactivatable Synthetic Dyes for Fluorescence Imaging at the Nanoscale *J. Phys. Chem. Lett.* **3** 2379–85

[2] Rial Verde E M 2008 Photorelease of GABA with visible light using an inorganic caging group *Front. Neural Circuits* **2**

[3] Diaspro A, Chirico G and Collini M 2005 Two-photon fluorescence excitation and related techniques in biological microscopy *Q. Rev. Biophys.* **38** 97–166

[4] Dougherty T J 1993 PHOTODYNAMIC THERAPY *Photochem. Photobiol.* **58** 895–900

[5] Agostinis P, Berg K, Cengel K A, Foster T H, Girotti A W, Gollnick S O, Hahn S M, Hamblin M R, Juzeniene A, Kessel D, Korbelik M, Moan J, Mroz P, Nowis D, Piette J, Wilson B C and Golab J 2011 Photodynamic therapy of cancer: An update *CA. Cancer J. Clin.* **61** 250–81

[6] Dolmans D E J G J, Fukumura D and Jain R K 2003 Photodynamic therapy for cancer *Nat. Rev. Cancer* **3** 380–7

[7] Majumdar P, Nomula R and Zhao J 2014 Activatable triplet photosensitizers: magic bullets for targeted photodynamic therapy *J Mater Chem C* **2** 5982–97

[8] Marchal S, François A, Dumas D, Guillemin F and Bezdetnaya L 2007 Relationship between subcellular localisation of Foscan® and caspase activation in photosensitised MCF-7 cells *Br. J. Cancer* **96** 944–51

[9] Castano A P, Mroz P and Hamblin M R 2006 Photodynamic therapy and anti-tumour immunity *Nat. Rev. Cancer* **6** 535–45

[10] Bechet D, Couleaud P, Frochot C, Viriot M-L, Guillemin F and Barberi-Heyob M 2008 Nanoparticles as vehicles for delivery of photodynamic therapy agents *Trends Biotechnol.* **26** 612–21

[11] Konan Y N, Gurny R and Allémann E 2002 State of the art in the

delivery of photosensitizers for photodynamic therapy *J. Photochem. Photobiol. B* **66** 89–106

[12] Sharman W 2004 Targeted photodynamic therapy via receptor mediated delivery systems *Adv. Drug Deliv. Rev.* **56** 53–76

[13] Bransden B H and Joachain C J 2003 *Physics of atoms and molecules* (Harlow, England ; New York: Prentice Hall)

[14] Atkins P W and Friedman R 2011 *Molecular quantum mechanics* (Oxford ; New York: Oxford University Press)

[15] Valeur B 2002 *Molecular fluorescence: principles and applications* (Weinheim ; New York: Wiley-VCH)

[16] Sathyanarayana D N 2001 *Electronic absorption spectroscopy and related techniques* (Hyderabad, India: Universities Press)

[17] Lakowicz J R 2010 *Principles of fluorescence spectroscopy* (New York, NY: Springer)

[18] Goodman L S and Gilman A 1975 *The Pharmacological basis of therapeutics* (New York: Macmillan)

[19] Barnard E A, Skolnick P, Olsen R W, Mohler H, Sieghart W, Biggio G, Braestrup C, Bateson A N and Langer S Z 1998 International Union of Pharmacology. XV. Subtypes of gamma-aminobutyric acidA receptors: classification on the basis of subunit structure and receptor function *Pharmacol. Rev.* **50** 291–313

[20] Sernagor E 2010 GABAergic control of neurite outgrowth and remodeling during development and adult neurogenesis: general rules and differences in diverse systems *Front. Cell. Neurosci.* **4**

[21] Petroski R E, Pomeroy J E, Das R, Bowman H, Yang W, Chen A P and Foster A C 2006 Indiplon Is a High-Affinity Positive Allosteric Modulator with Selectivity for α1 Subunit-Containing GABA $_A$ Receptors *J. Pharmacol. Exp. Ther.* **317** 369–77

[22] Clementi F, Fumagalli G and Chiamulera C 2016 *Farmacologia generale e molecolare: il meccanismo d’azione dei farmaci* (Milano: Edra)

[23] Olsen R W and Sieghart W 2008 International Union of Pharmacology. LXX. Subtypes of γ-Aminobutyric Acid $_A$ Receptors: Classification

on the Basis of Subunit Composition, Pharmacology, and Function. Update *Pharmacol. Rev.* **60** 243–60

[24] Ramerstorfer J, Furtmuller R, Sarto-Jackson I, Varagic Z, Sieghart W and Ernst M 2011 The GABAA Receptor + - Interface: A Novel Target for Subtype Selective Drugs *J. Neurosci.* **31** 870–7

[25] Zayat L, Noval M G, Campi J, Calero C I, Calvo D J and Etchenique R 2007 A New Inorganic Photolabile Protecting Group for Highly Efficient Visible Light GABA Uncaging *ChemBioChem* **8** 2035–8

[26] Ellis-Davies G C R 2009 Basics of Photoactivation *Cold Spring Harb. Protoc.* **2009** pdb.top55-pdb.top55

[27] Popovic M A, Carnevale N, Rozsa B and Zecevic D 2015 Electrical behaviour of dendritic spines as revealed by voltage imaging *Nat. Commun.* **6** 8436

[28] Arvin M C, Wokosin D L, Banala S, Lavis L D and Drenan R M 2019 Probing Nicotinic Acetylcholine Receptor Function in Mouse Brain Slices via Laser Flash Photolysis of Photoactivatable Nicotine *J. Vis. Exp.* 58873

[29] Brown S B, Brown E A and Walker I 2004 The present and future role of photodynamic therapy in cancer treatment *Lancet Oncol.* **5** 497–508

[30] Ormond A and Freeman H 2013 Dye Sensitizers for Photodynamic Therapy *Materials* **6** 817–40

[31] Lepeshkevich S V, Parkhats M V, Stasheuski A S, Britikov V V, Jarnikova E S, Usanov S A and Dzhagarov B M 2014 Photosensitized Singlet Oxygen Luminescence from the Protein Matrix of Zn-Substituted Myoglobin *J. Phys. Chem. A* **118** 1864–78

[32] Frauenfelder H, McMahon B H, Austin R H, Chu K and Groves J T 2001 The role of structure, energy landscape, dynamics, and allostery in the enzymatic function of myoglobin *Proc. Natl. Acad. Sci.* **98** 2370–4

[33] Ascoli F, Rossi Fanelli M R and Antonini E 1981 [5] Preparation and properties of apohemoglobin and reconstituted hemoglobins *Methods in Enzymology* vol 76 (Elsevier) pp 72–87

[34] Curry S, Brick P and Franks N P 1999 Fatty acid binding to human serum albumin: new insights from crystallographic studies *Biochim. Biophys. Acta* **1441** 131–40

[35] Bujacz A, Zielinski K and Sekula B 2014 Structural studies of bovine, equine, and leporine serum albumin complexes with naproxen: Structures of BSA, ESA, and LSA with Naproxen *Proteins Struct. Funct. Bioinforma.* **82** 2199–208

[36] Peer D, Karp J M, Hong S, Farokhzad O C, Margalit R and Langer R 2007 Nanocarriers as an emerging platform for cancer therapy *Nat. Nanotechnol.* **2** 751–60

[37] Solban N, Rizvi I and Hasan T 2006 Targeted photodynamic therapy *Lasers Surg. Med.* **38** 522–31

[38] van Dongen G a. M S, Visser G W M and Vrouenraets M B 2004 Photosensitizer-antibody conjugates for detection and therapy of cancer *Adv. Drug Deliv. Rev.* **56** 31–52

[39] Verma S, Watt G M, Mai Z and Hasan T 2007 Strategies for Enhanced Photodynamic Therapy Effects *Photochem. Photobiol.* **83** 996–1005

[40] Goodhew P J, Humphreys F J and Beanland R 2001 *Electron microscopy and analysis* (London ; New York: Taylor & Francis)

[41] Alonso J L and Goldmann W H 2003 Feeling the forces: atomic force microscopy in cell biology *Life Sci.* **72** 2553–60

[42] Allison D P, Mortensen N P, Sullivan C J and Doktycz M J 2010 Atomic force microscopy of biological samples *Wiley Interdiscip. Rev. Nanomed. Nanobiotechnol.* **2** 618–34

[43] Inkson B J 2016 Scanning electron microscopy (SEM) and transmission electron microscopy (TEM) for materials characterization *Materials Characterization Using Nondestructive Evaluation (NDE) Methods* (Elsevier) pp 17–43

[44] Sanderson M J, Smith I, Parker I and Bootman M D 2014 Fluorescence Microscopy *Cold Spring Harb. Protoc.* **2014** pdb.top071795-pdb.top071795

[45] Novotny L and Hecht B 2006 *Principles of Nano-Optics* (Cambridge: Cambridge University Press)

[46] Pawley J B 2006 *Handbook Of Biological Confocal Microscopy* (Boston, MA: Springer US)

[47] Mondal P P and Diaspro A 2014 *Fundamentals of Fluorescence Microscopy* (Dordrecht: Springer Netherlands)

[48] Agard D A 1984 Optical sectioning microscopy: cellular architecture in three dimensions *Annu. Rev. Biophys. Bioeng.* **13** 191–219

[49] Parton R and Davis I 2006 Lifting the FogImage Restoration by Deconvolution *Cell Biology* vol 3 (Elsevier) pp 187–200

[50] Nwaneshiudu A, Kuschal C, Sakamoto F H, Rox Anderson R, Schwarzenberger K and Young R C 2012 Introduction to Confocal Microscopy *J. Invest. Dermatol.* **132** 1–5

[51] Koester C J 1980 Scanning mirror microscope with optical sectioning characteristics: applications in ophthalmology *Appl. Opt.* **19** 1749

[52] Chen J-T, Chen R-M, Lin Y-L, Chang H-C, Lin Y-H, Chen T-L and Chen T-G 2004 Confocal laser scanning microscopy: I. An overview of principle and practice in biomedical research *Acta Anaesthesiol. Taiwanica Off. J. Taiwan Soc. Anesthesiol.* **42** 33–40

[53] Schermelleh L, Heintzmann R and Leonhardt H 2010 A guide to super-resolution fluorescence microscopy *J. Cell Biol.* **190** 165–75

[54] Betzig E 2015 Single Molecules, Cells, and Super-Resolution Optics (Nobel Lecture) *Angew. Chem. Int. Ed.* **54** 8034–53

[55] Hell S W 2015 Nanoscopy with Focused Light (Nobel Lecture) *Angew. Chem. Int. Ed.* **54** 8054–66

[56] Moerner W E W E 2015 Single-Molecule Spectroscopy, Imaging, and Photocontrol: Foundations for Super-Resolution Microscopy (Nobel Lecture) *Angew. Chem. Int. Ed.* **54** 8067–93

[57] Thorley J A, Pike J and Rappoport J Z 2014 Super-resolution Microscopy *Fluorescence Microscopy* (Elsevier) pp 199–212

[58] Diaspro A 2010 *Nanoscopy and Multidimensional Optical Fluorescence Microscopy* (Chapman and Hall/CRC)

[59] Bianchini P, Peres C, Oneto M, Galiani S, Vicidomini G and Diaspro A 2015 STED nanoscopy: a glimpse into the future *Cell Tissue Res.* **360** 143–50

[60] Vicidomini G, Bianchini P and Diaspro A 2018 STED super-

resolved microscopy *Nat. Methods* **15** 173–82

[61] Galiani S, Harke B, Vicidomini G, Lignani G, Benfenati F, Diaspro A and Bianchini P 2012 Strategies to maximize the performance of a STED microscope *Opt. Express* **20** 7362

[62] Huang B, Bates M and Zhuang X 2009 Super-Resolution Fluorescence Microscopy *Annu. Rev. Biochem.* **78** 993–1016

[63] Gustafsson M G L 2000 Surpassing the lateral resolution limit by a factor of two using structured illumination microscopy. SHORT COMMUNICATION *J. Microsc.* **198** 82–7

[64] Leutenegger M, Eggeling C and Hell S W 2010 Analytical description of STED microscopy performance *Opt. Express* **18** 26417

[65] Denk W, Strickler J and Webb W 1990 Two-photon laser scanning fluorescence microscopy *Science* **248** 73–6

[66] Albota M A, Xu C and Webb W W 1998 Two-photon fluorescence excitation cross sections of biomolecular probes from 690 to 960 nm *Appl. Opt.* **37** 7352

[67] Helmchen F and Denk W 2005 Deep tissue two-photon microscopy *Nat. Methods* **2** 932–40

[68] Bianchini P, Harke B, Galiani S, Vicidomini G and Diaspro A 2012 Single-wavelength two-photon excitation-stimulated emission depletion (SW2PE-STED) superresolution imaging *Proc. Natl. Acad. Sci.* **109** 6390–3

[69] Malmivuo J and Plonsey R 1995 *Bioelectromagnetism: principles and applications of bioelectric and biomagnetic fields* (New York: Oxford University Press)

[70] Conforti L 2012 Patch-Clamp Techniques *Cell Physiology Source Book* (Elsevier) pp 369–81

[71] Hamill O P, Marty A, Neher E, Sakmann B and Sigworth F J 1981 Improved patch-clamp techniques for high-resolution current recording from cells and cell-free membrane patches *Pflüg. Arch. - Eur. J. Physiol.* **391** 85–100

[72] Ogden David S P 1994 Patch clamp techniques for single channel and whole-cell recording

[73] Polder H R, Weskamp M, Linz K and Meyer R 2005 Voltage-

Clamp and Patch-Clamp Techniques *Practical Methods in Cardiovascular Research* ed S Dhein, F W Mohr and M Delmar (Berlin/Heidelberg: Springer-Verlag) pp 272–323

[74] Delcanale P, Pennacchietti F, Maestrini G, Rodríguez-Amigo B, Bianchini P, Diaspro A, Iagatti A, Patrizi B, Foggi P, Agut M, Nonell S, Abbruzzetti S and Viappiani C 2015 Subdiffraction localization of a nanostructured photosensitizer in bacterial cells *Sci. Rep.* **5** 15564

[75] Shcherbakova D M, Baloban M, Emelyanov A V, Brenowitz M, Guo P and Verkhusha V V 2016 Bright monomeric near-infrared fluorescent proteins as tags and biosensors for multiscale imaging *Nat. Commun.* **7** 12405

[76] Robello M, Amico C and Cupello A 1993 Regulation of gabaa receptor in cerebellar granule cells in culture: Differential involvement of kinase activities *Neuroscience* **53** 131–8

[77] Cozzolino M, Pesce L, Pezzuoli D, Montali C, Brancaleon L, Cavanna L, Abbruzzetti S, Diaspro A, Bianchini P and Viappiani C 2019 Apomyoglobin is an efficient carrier for zinc phthalocyanine in photodynamic therapy of tumors *Biophys. Chem.* **253** 106228

[78] Buschow K H J 2001 *Encyclopedia of materials: science and technology* (Amsterdam ; New York: Elsevier)

[79] Soeller C and Cannell M B 1999 Two-photon microscopy: imaging in scattering samples and three-dimensionally resolved flash photolysis *Microsc. Res. Tech.* **47** 182–95

[80] Tosteson D C 1978 *Concepts and Models* (Berlin, Heidelberg: Springer Berlin Heidelberg)

[81] Robello M, Baldelli P and Cupello A 1994 Modulation by extracellular pH of the activity of GABAA receptors on rat cerebellum granule cells *Neuroscience* **61** 833–7

[82] Filevich O, Zayat L, Baraldo L M and Etchenique R 2014 Long Wavelength Phototriggering: Ruthenium-Based Caged Compounds *Luminescent and Photoactive Transition Metal Complexes as Biomolecular Probes and Cellular Reagents* vol 165, ed K K-W Lo (Berlin, Heidelberg: Springer Berlin Heidelberg) pp 47–68

[83] Zanacchi F C, Bianchini P and Vicidomini G 2014 Fluorescence microscopy in the spotlight: Fluorescence Microscopy in the Spotlight *Microsc. Res. Tech.* **77** 479–82

[84] Miskovsky P, Hritz J, Sanchez-Cortes S, Fabriciova G, Ulicny J and Chinsky L 2001 Interaction of hypericin with serum albumins: surface-enhanced Raman spectroscopy, resonance Raman spectroscopy and molecular modeling study *Photochem. Photobiol.* **74** 172–83

[85] Roelants M, Van Cleynenbreugel B, Lerut E, Van Poppel H and de Witte P A M 2011 Human serum albumin as key mediator of the differential accumulation of hypericin in normal urothelial cell spheroids versus urothelial cell carcinoma spheroids *Photochem. Photobiol. Sci. Off. J. Eur. Photochem. Assoc. Eur. Soc. Photobiol.* **10** 151–9

[86] Comas-Barceló J, Rodríguez-Amigo B, Abbruzzetti S, Rey-Puech P del, Agut M, Nonell S and Viappiani C 2013 A self-assembled nanostructured material with photosensitising properties *RSC Adv.* **3** 17874

[87] Rodríguez-Amigo B, Delcanale P, Rotger G, Juárez-Jiménez J, Abbruzzetti S, Summer A, Agut M, Luque F J, Nonell S and Viappiani C 2015 The complex of hypericin with β-lactoglobulin has antimicrobial activity with potential applications in dairy industry *J. Dairy Sci.* **98** 89–94

[88] Bianchini P, Cozzolino M, Oneto M, Pesce L, Pennacchietti F, Tognolini M, Giorgio C, Nonell S, Cavanna L, Delcanale P, Abbruzzetti S, Diaspro A and Viappiani C 2019 Hypericin–Apomyoglobin: An Enhanced Photosensitizer Complex for the Treatment of Tumor Cells *Biomacromolecules* **20** 2024–33

[89] Betzig E, Patterson G H, Sougrat R, Lindwasser O W, Olenych S, Bonifacino J S, Davidson M W, Lippincott-Schwartz J and Hess H F 2006 Imaging Intracellular Fluorescent Proteins at Nanometer Resolution *Science* **313** 1642–5

[90] Pezzuoli D, Cozzolino M, Montali C, Brancaleon L, Bianchini P, Zantedeschi M, Bonardi S, Viappiani C and Abbruzzetti S 2018 Serum albumins are efficient delivery systems for the photosensitizer hypericin in photosensitization-based treatments against Staphylococcus aureus *Food Control* **94** 254–62

[91] Doix B, Bastien E, Rambaud A, Pinto A, Louis C, Grégoire V, Riant

O and Feron O 2018 Preclinical Evaluation of White Led-Activated Non-porphyrinic Photosensitizer OR141 in 3D Tumor Spheroids and Mouse Skin Lesions *Front. Oncol.* **8** 393

[92] Evans C L 2015 Three-dimensional in vitro cancer spheroid models for photodynamic therapy: strengths and opportunities *Front. Phys.* **3**

[93] Mohammad-Hadi L, MacRobert A J, Loizidou M and Yaghini E 2018 Photodynamic therapy in 3D cancer models and the utilisation of nanodelivery systems *Nanoscale* **10** 1570–81

[94] Kamuhabwa A, Huygens A and De Witte P 2003 Photodynamic therapy of transitional cell carcinoma multicellular tumor spheroids with hypericin *Int. J. Oncol.*

[95] Huygens A, Huyghe D, Bormans G, Verbruggen A, Kamuhabwa A R, Roskams T and de Witte P A M 2003 Accumulation and photocytotoxicity of hypericin and analogs in two- and three-dimensional cultures of transitional cell carcinoma cells *Photochem. Photobiol.* **78** 607–14

[96] Alemany-Ribes M, García-Díaz M, Busom M, Nonell S and Semino C E 2013 Toward a 3D Cellular Model for Studying *In Vitro* the Outcome of Photodynamic Treatments: Accounting for the Effects of Tissue Complexity *Tissue Eng. Part A* **19** 1665–74

[97] Xiao Z, Hansen C B, Allen T M, Miller G G and Moore R B 2005 Distribution of photosensitizers in bladder cancer spheroids: implications for intravesical instillation of photosensitizers for photodynamic therapy of bladder cancer *J. Pharm. Pharm. Sci. Publ. Can. Soc. Pharm. Sci. Soc. Can. Sci. Pharm.* **8** 536–43

[98] A. Staicu, , A. Pascu, , A. Nuta, , A. Sorescu, , V. Raditoiu and , M.L. Pascu 2013 Studies about phtalocyanine photosensitizer to be used in photodinamic therapy *Romanian Rep. Phys.* **65** 1032–1051

[99] Labbé R F, Vreman H J and Stevenson D K 1999 Zinc protoporphyrin: A metabolite with a mission *Clin. Chem.* **45** 2060–72

[100] Fernandez J M, Bilgin M D and Grossweiner L I 1997 Singlet oxygen generation by photodynamic agents *J. Photochem. Photobiol. B* **37** 131–40

[101] Linder S, Barkhem T, Norberg A, Persson H, Schalling M, Hökfelt

T and Magnusson G 1987 Structure and expression of the gene encoding the vasoactive intestinal peptide precursor *Proc. Natl. Acad. Sci. U. S. A.* **84** 605–9

[102] Zia H, Hida T, Jakowlew S, Birrer M, Gozes Y, Reubi J C, Fridkin M, Gozes I and Moody T W 1996 Breast cancer growth is inhibited by vasoactive intestinal peptide (VIP) hybrid, a synthetic VIP receptor antagonist *Cancer Res.* **56** 3486–9

[103] Maheshwari R K, Singh A K, Gaddipati J and Srimal R C 2006 Multiple biological activities of curcumin: A short review *Life Sci.* **78** 2081–7

[104] Chignell C F, Bilskj P, Reszka K J, Motten A G, Sik R H and Dahl T A 1994 SPECTRAL AND PHOTOCHEMICAL PROPERTIES OF CURCUMIN *Photochem. Photobiol.* **59** 295–302

[105] Cozzolino M, Delcanale P, Montali C, Tognolini M, Giorgio C, Corrado M, Cavanna L, Bianchini P, Diaspro A, Abbruzzetti S and Viappiani C 2019 Enhanced photosensitizing properties of protein bound curcumin *Life Sci.* **233** 116710

[106] Ben-Zichri S, Kolusheva S, Danilenko M, Ossikbayeva S, Stabbert W J, Poggio J L, Stein D E, Orynbayeva Z and Jelinek R 2019 Cardiolipin mediates curcumin interactions with mitochondrial membranes *Biochim. Biophys. Acta BBA - Biomembr.* **1861** 75–82

[107] Reddy C A, Somepalli V, Golakoti T, Kanugula A K, Karnewar S, Rajendiran K, Vasagiri N, Prabhakar S, Kuppusamy P, Kotamraju S and Kutala V K 2014 Mitochondrial-Targeted Curcuminoids: A Strategy to Enhance Bioavailability and Anticancer Efficacy of Curcumin ed R J Anto *PLoS ONE* **9** e89351